**Gallium nitride based heterojunction field effect transistor: fabrication and application**

by

Resham Raj Thapa

A dissertation submitted to the Graduate Faculty of
Auburn University
in partial fulfillment of the
requirements for the Degree of
Doctor of Philosophy

Auburn, Alabama
August 4, 2012

Keywords: GaN, Heterojunction, DNA sensor, PZT



Approved by

Minseo Park, Chair, Associate Professor of Physics
Michael J. Bozack, Professor of Physics
Ahjeong Son, Assistant Professor of Civil Engineering
Dong-Joo Kim, Associate Professor of Materials Research and Education Center

Abstract

Gallium nitride (GaN) is a wide bandgap semiconducting material, which is piezoelectric, biocompatible, and also resistive to ionizing radiation. Material properties such as direct bandgap, chemical/thermal stability, higher mobility, higher saturation velocity, and higher sensitivity makes it an auspicious material for the use in electronics, optoelectronics as well as bioelectronics based applications. In the first part of this dissertation, fabrication of aluminum gallium nitride/gallium nitride heterojunction field effect transistor (AlGaN/GaN HFET) for the detection of the DNA hybridization has been discussed. Photopatternable spin-on silicone has used to encapsulate the device except the gate electrode for the use in aqueous environment. Biofunctionalization and immobilization chemistry using the assembly of an alkanethiol self assembled monolayer (SAM) onto the metal gate, and the subsequent coupling of amine-terminated ssDNA to the SAM has been discussed. Current-voltage ($I_D$-$V_{DS}$) and current-time ($I_D$-t) measurements of DNA binding experiments using the field effect transistors are presented, in which the hybridization of a fully complementary target DNA sequence is compared to that of a partly mismatched target DNA sequence. Second part of this dissertation describes the incorporation of amorphous lead zirconium titanate (PZT) thin film as a gate dielectric in AlGaN/GaN heterojunction field effect transistor. Comparative study regarding transistor output, transfer and gate current leakage between the Ni/Au Schottky gate conventional HFET and amorphous PZT incorporated PZT/Ni/Au gate HFET were carried out. Significant reduction in gate leakage current had observed with the incorporation of the PZT thin film as a gate dielectric.

Acknowledgments

I owe my deepest gratitude to my advisor Dr. Minseo Park for providing such a great research environment. His encouragement, guidance and support from the initial to the final level not only enabled me to develop an understanding of the subject, but also helped me to overcome challenges in many aspects of life. I am also very thankful to all the committee members, Dr. Michael J. Bozack, Dr. John R. Williams, Dr. Ahjeong Son, Dr. Dong-Joo Kim, Dr. Michael Hamilton for their time and participation in evaluating this work.

I cannot thank enough Dr. Ahjeong Son for her guidance and letting me use her lab. I am very indebted to her for giving every support whenever it was needed. I am also grateful to Dr. Claude Ahyi and Ms. Tamara Isaacs-Smith for their help with the semiconductor processing and characterization. They have been valuable resources for me and I have greatly benefited from their knowledge and expertise. I would also like to thank Mr. Max Cichon for his training and excellent job on keeping the facilities running. I would also like to thank Dr. Dong-Joo Kim and Dr. David Stanbury for letting me use the facilities in their lab. In addition, I would like to thank Dr. Sarit Dhar, Dr. Siddharth Alur, Dr. Yaqi Wang, Mr. Yogesh Sharma, Ms. Fei Tong, Mr. Jing Dai, Mr. Seon-Bae Kim, and Mr. Nootan Bhattarai for helping me throughout this research.

My deep love and appreciation goes to my family whose love and support still sustain me today. Finally I would like to dedicate this thesis to my late father Khaman Sing Thapa, whose words of inspiration and encouragement in pursuit of excellence, still lingers in me.

Table of Contents

List of Tables

List of Figures

List of Abbreviations

| | |
|---|---|
| 2DEG | 2 dimensional electron gas |
| 2DHG | 2 dimensional hole gas |
| CE | Capillary electrophoresis |
| CFOM | Combined figure of merit |
| CGS | Gouy-Chapman-Stern |
| DC | Direct current |
| DI | Deionized |
| DNA | Deoxyribonucleic acid |
| EFO | Electric flame off |
| FAB | Free air ball |
| FET | Field effect transistor |
| FOM | Figure of merit |
| HCP | Hexagonal close pack |
| HEMT | High electron mobility transistor |
| HFET | Heterojunction field effect transistor |
| IC | Integrated circuit |
| IHP | Inner Helmholtz plane |
| I-V | Current-voltage |

| | |
|---|---|
| JFOM | Johnson figure-of-merit |
| LED | Light emitting diode |
| LD | Laser diode |
| MEMS | Micro-electro mechanical system |
| MFS | Minimum feature size |
| MOSFET | Metal oxide semiconductor field-effect transistor |
| NVRAM | Non-volatile random access memory |
| NA | Numerical aperture |
| OHP | Outer Helmholtz plane |
| PDMS | Polydimethlysiloxane |
| PPS | Photopatternable spin-on silicone |
| PZT | Lead zirconium titanate |
| RF | Radio frequency |
| RIE | Reactive ion etching |
| RPM | Revolutions per minute |
| RTA | Rapid thermal annealing |
| SAM | Self-assembled monolayer |
| SAW | Surface acoustic wave |
| STR | Short tandem repeats |
| TCE | Trichloroethylene |
| UV | Ultra-violet |
| WBG | Wide bandgap |
| XPS | X-ray photoelectron spectroscopy |

# Chapter 1

## Background

### 1.1 Scope of the semiconductor field effect transistor based biosensor

Standard deoxyribonucleic acid (DNA) sequencing technologies at present involve multiple steps and require large and expensive scanner/analyzer equipment. Since the DNA molecules do not have an intrinsic optical property, they are subjected to labeling for the optical detection. At present, hybridization based microarray, capillary electrophoresis, etc. are the dominant techniques for the DNA sequencing.[1] Radioactive tagging, silver staining etc. have been used traditionally; whereas fluorescent dyes, mediator molecules, etc. in combination with the short tandem repeats (STRs) as a marker are used in the current optical and electrochemical detection settings for DNA sequencing.[2]

In microarray biochips based DNA detection scheme, the surface of the chip is covered with the DNA probes and is subjected to hybridization with the target DNA molecules.[3] Nonetheless, this method also involves pre-labeling of the target molecules and thus all the intricacies of optical detection. Other typical biomolecule sensing techniques include: electrochemical, surface plasmon resonance, impedance spectrometry, quartz crystal microbalance, etc. In general, these techniques also do not support the realization of consumer end handheld electronic devices.

The trend for the sensor is toward the simpler, faster and miniature devices that do not require costly reagents, bulky instrumentation set-ups, operating skills etc. At present, nucleic acid and protein detection are essentially associated with the semi automated laboratory settings and only available to the centralized location. As compared to the commercial demands, the current capabilities for the DNA sequencing are limited. None of the methods are portable enough to use outside the laboratory settings and also involves the final analysis of the data by the skilled personnel. They also require pre-labeling of the molecule analytes and are time consuming.[4] Associated costs and technology requirements often makes the current commercial detection schemes unsuitable for large screening programs.

Biotechnology is quickly taking advantage of well-developed micro and nano fabrication technology. It's been shown that semiconductor field effect transistor (FET) based biosensor can be used for the detection of the biomolecules.[5,6,7] They offer the label-free detection route and convert the biochemical processes into electronic signal for the direct electrical readout. Field effect transistors with the hybridization based electronic detection techniques is very convenient for diagnostic and comparative sequencing. Key features such as real time, fast, miniature in size, and low-tech operation are combined with the monolithic integration capabilities into the electronic devices makes it very attractive for the commercial application. With the suitable choice of the semiconductor material and biofunctionalization chemistry, it is possible to produce the highly selective and sensitive handheld devices. By further incorporating microfluidics delivery system, nanorods, quantum dots etc. to the sensing electrode, the sensitivity of the detection can be increased.

As of now, there hasn't been any successful semiconductor FET based nucleic acid sensor available for commercial purpose. Considering the increasing demand, advancement in the semiconductor material growth, sophisticated device fabrication technology; fully electronic biosensors are the potential successors to a wide range of analytical sensors. In this regard, III-Nitride semiconductor materials present an attractive platform for the fabrication of the FET based biosensor. They possess superior material characteristics such as non-toxicity to the living cells, higher chemical and thermal stability, higher sensitivity, higher energy bandgap etc. as compared to the conventional semiconducting materials. Polarization and surface states are believed to create the highly mobile 2 dimensional electron gas (2DEG) channel at the heterointerface, which lies proximity to the surface, thus making it highly sensitive to the surface phenomena. Biomolecules can be directly immobilized to the semiconductor gate surface or on the Schottky gate contact of the device for the electronic detection. Fabricating the array of suitably spaced transistors will permit the multi-parameter detection without using markers and labels as used in conventional detection techniques.

In general, it is expected that semiconductor FET-based biosensor has the potential to become better alternative to the current electrochemical and optical detection based capillary electrophoresis (CE) & microarray technology. It will offer the conveniences that a handheld digital electronic device provides and testing will become more routine and simpler.

## 1.2 Integration of PZT thin film oxide with AlGaN/GaN HFET

Conventional AlGaN/GaN (aluminum gallium nitride/ gallium nitride) heterojunction field effect transistors (HFET) suffer from large gate leakage current resulting in additional noise source, current collapse problem that affects the overall reliability and poor power efficiency.[8,9,10,11] The leakage current also lowers the breakdown voltage caused by the impact ionization of hot electrons.[12] By integrating a thin dielectric layer under the gate, aforementioned gate leakage problems can be minimized.

Generally, a material that is less conducting and more polar exhibits high dielectric constant ($\kappa$). Appropriate $\kappa$ value allows incorporation of reasonably thicker dielectric material while maintaining the same value of the capacitance required for controlling the gate channel current. High $\kappa$ polycrystalline lead zirconium titanate (PZT) with large grain boundary is less suited as a gate dielectric. On the other hand, single crystalline PZT with nominal grain boundary requires higher processing temperature, which degrades the PZT-semiconductor interface. By using amorphous PZT with appropriate thickness, gate leakage problem of the AlGaN/GaN HFET can be reduced. In addition to the high dielectric constant; excellent ferroelectric, piezoelectric and pyroelectric properties of the crystalline PZT makes it suitable for sensors and actuators devices such as infrared sensors, torque sensors, humidity sensors, high frequency ferroelectric sonar transducers, micro-electro mechanical system devices (MEMS).[13]

### 1.3 Solid-liquid interface: an electrical double layer

The interface between the solid and liquid surface is very interesting and important for the device operating in the liquid medium.[14,15,16,17] Electrical property at the interface between the solid electrode and electrolyte solution is considerably different than that of the bulk solution. When these two mediums come in contact, the solid surface becomes charged due to the differences in the electrons or ions affinities between them. In addition, the ions in the electrolyte also redistributes accordingly. This rearrangement of the charged particles gives rise to a distinct charged layers in the interface called as an electrical double layer.

The electrical double layer model was first put forward by Helmholtz in 1853. According to the model, metallic electrode and electrolyte interface behaves like an electrical capacitor, where the electrode possesses a charge density of $q^m$, arising from the excess ($-q^m$) or deficiencies ($+q^m$) of the electrons. This charge on the electrode surface attracts the equal amount of oppositely charged ions ($\pm q^n$) in the electrolyte; a rigidly held charged layers in a plane perpendicular and very close to the electrode surface. The capacitance of this simple approximation can be given by[18,19]

$$C_H = \frac{\epsilon \epsilon_0}{d_H} \qquad [1.1]$$

where $\epsilon$ is the dielectric constant, $\epsilon_0$ is the permittivity of the free space and $d_H$ is the distance between the electrode surface and center of the counterions layer, which is roughly the radius of the counterions. As depicted in the Fig. 1(a), the electric potential decreases linearly across the counterion layer. The Helmholtz model hypothesizes the counterions as a rigid layer, which might be a close approximation only for polarizable

electrodes with a sufficiently high electrolyte concentration. However, the actual scenario is different and has been modified by Gouy-Chapman and later by Stern.[20]

Gouy & Chapman suggested that the electrode-electrolyte interface comprises of adsorbed ions at the electrode surface and an equal number of counterions in the solution. The electrostatic force between the ions will be disturbed by the random thermal motion, which disperses the ions. The Gouy-Chapman model assumes that the ions as a point charge extended within the single diffuse layer as depicted in Fig. 1(b).

The electrostatic potential $\Phi(\vec{x})$ due to the local charge density $\rho(\vec{x})$ can be solved by Poisson's equation as

$$\nabla^2\Phi(\vec{x}) = -\frac{\rho(\vec{x})}{\epsilon\epsilon_o} \qquad [1.2]$$

The fluctuation in surface potential caused by the mobile ions presents the substantial difficulty to solve the above equation. However, by considering the ions to be Boltzmann-distributed in the potential $\Phi(\vec{x})$, we can write the local cation and anion concentration as

$$c^+(\vec{x}) = c_o e^{-e\phi(\vec{x})/k_BT} \qquad [1.3]$$

and

$$c^-(\vec{x}) = c_o e^{e\phi(\vec{x})/k_BT} \qquad [1.4]$$

where $c_o$ is the ion concentration of the electrolyte, $e$ is the electronic charge, $k_B$ is the Boltzmann's constant, and $T$ is the absolute temperature. For monovalent ions such as NaCl, we can write the total local charge density as

$$\rho(\vec{x}) = e[c^{+}(\vec{x}) + c^{-}(\vec{x})] + \rho_{fixed}(\vec{x}) \qquad [1.5]$$

where $\rho_{fixed}(\vec{x})$ is the charge density due to the fixed charges such as due to the electrodes or macromolecules. Substituting into Poisson's equation above,

$$\nabla^2\Phi(\vec{x}) = \frac{c_o e}{\epsilon\epsilon_o}\left(e^{e\phi(\vec{x})/k_BT} - e^{-e\phi(\vec{x})/k_BT}\right) - \frac{\rho_{fixed}(\vec{x})}{\epsilon\epsilon_o} \qquad [1.6]$$

For an infinite charged plane of potential $\phi_0$, Gouy and Chapman independently solved the above equation in 1910. Rather than the linear drop, they found a roughly exponential drop in potential for lower $\phi_0$, and more rapid drop for higher $\phi_0$.[21] They suggested that the counterions distributes to the diffuse layer near the electrode surface with the concentration dropping off away from the electrode surface due to the smaller electrostatic force as compared to the thermal effects. With this model, the general expression for the capacitance of the electrical double layer becomes

$$C_{GC} = \sqrt{\frac{2e^2\epsilon\epsilon_o c_o}{kT}}\,\cosh\left(\frac{e\phi_o}{2kT}\right). \qquad [1.7]$$

For room temperature,

$$C_{GC}\left[F/cm^2\right] = 2.3\sqrt{c_o(M)}\,\cosh(19.5\phi_o)[V] \qquad [1.8]$$

With the increase in $\phi_o$, the value of the capacitance given by equation [1.8] increases exponentially. This unphysical result is due to the fact that the model ignores the finite size of the ions.[22]

To solve the problem, Stern in 1924 suggested that both the ion size and thermal energy are important parameters in calculating the capacitance, thus cannot be neglected. This model considers both the Helmholtz and Gouy-Chapman model and also called as a

Gouy-Chapman-Stern (CGS) model. The total capacitance is series combination of both the Helmholtz and Gouy-Chapman capacitance as given by

$$\frac{1}{C_{CGS}} = \frac{1}{C_H} + \frac{1}{C_{GC}} . \qquad [1.9]$$

As the series capacitance is dominated by smaller of the two capacitance, Stern model correctly predicts the double layer capacitance for lower surface potential. However, with the increase of the surface potential, the capacitance assumes a constant value instead of exponential increase.[23]

Grahame in 1947 modified the Stern's model by distinguishing specifically surface adsorbed ions (ions that lose their hydration shell and are chemically bonded with the surface; thus very close to the surface) as the inner Helmholtz plane (IHP) and non-specifically adsorbed ions with the hydration shell as the outer Helmholtz plane (OHP) as shown in the Fig. 1(d). As depicted in the Fig., the layer beyond the outer Helmholtz plane constitutes the diffuse layer. The diffused double layer model assumes that the excess ions in a solution distribute beyond the OHP and the thickness of the double layer varies accordingly.

In 1963, Bockris, Devanathan & Muller suggested a modified model of the double layer, where a layer of specifically oriented solvent molecules physically separates the hydrated counterions from the metal electrode.[24] Close to the electrode surface, the water molecules cannot rotate freely and this will reduce the dielectric constant at the first layer ($\epsilon \sim 6$), whereas the second layer has $\epsilon \sim 30$ as compared to the $\epsilon \sim 78.5$ for normal water as shown in the Fig. 1(e). With this modification, Gouy-Chapman-Stern model gives better assessment of the dependence of surface potential on the capacitance and is the standard model of the electrical double layer for the charged surface.

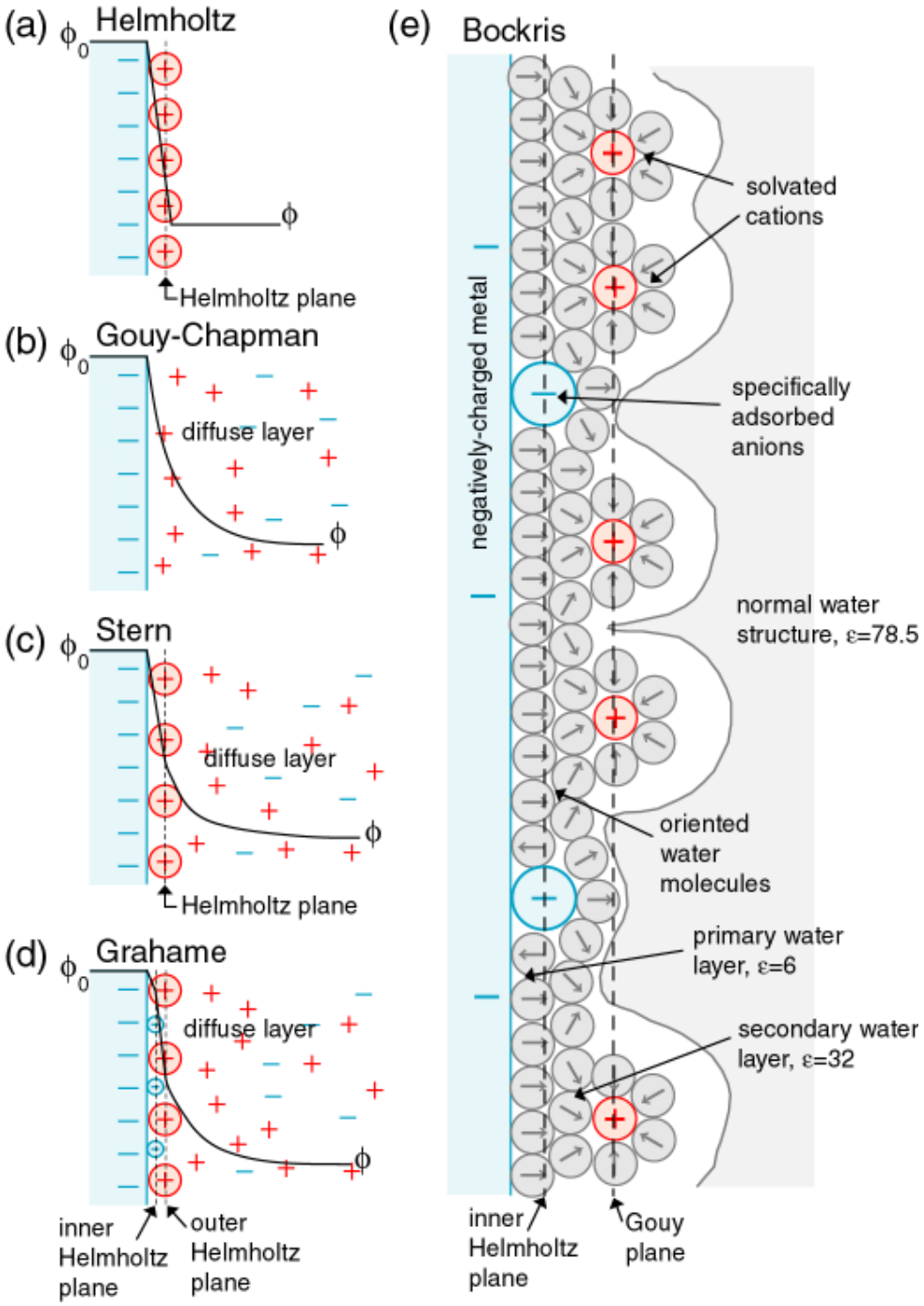


Fig. 1.1 Electrical double layer model for the negatively charged electrode surface with $\phi_0$ as a surface potential and $\phi$ as decay potential. (a) Helmholtz model of the rigid counterions layers (b) Gouy-Chapman model for the diffuse electrical double layer (c) Stern model for the distribution of ions at the electrode-electrolyte interface (d) Grahame model with the specifically adsorbed ions at the inner Helmholtz plane and hydrated ions at the outer Helmholtz plane (e) The model of Bockris, Devanathan and Muller. (Reproduced from[25])

## 1.4 Synopsis of the dissertation

This dissertation focuses on fabrication of the AlGaN/GaN heterojunction field effect transistors (HFET) for DNA sensor as well as development of the dielectric incorporated HFET for the reduction of gate leakage current. Chapter 2 provides basic background and literature survey of the gallium nitride based heterostructure. The chapter starts with the short description of the current semiconductor technology and proceeds with introducing the crystal, physical and electrical properties of the III-Nitride semiconducting material. In addition, polarization, source of 2DEG electrons and factors influencing the 2DEG density in AlGaN/GaN heterostructure are also discussed. In chapter 3, details involving the semiconductor processing techniques are discussed. Methods and tools involved in sample cleaning, contact deposition, and packaging of the devices are presented. Chapter 4 presents DNA detection experiment using AlGaN/GaN heterojunction field effect transistor with the amine based biofunctionalization chemistry. Lastly, chapter 5 presents the basic processing steps of amorphous PZT thin film gate dielectric AlGaN/GaN HFET. Fabricated device structures and their electrical characterization are also discussed.

**References**

[1] W. J. Ansorge, "Next-generation DNA sequencing techniques", New Biotechnology **25**, 195 (2009).

[2] L. M. Bellan, D. Wu, R. S. Langer, "Current trends in nanobiosensor technology", Wiley Interdiscip. Rev. Nanomed. Nanobiotechnol. **3**, 229 (2011).

[3] P. Bao, A. G. Frutos, C. Greef, J. Lahiri, U. Muller, T. C. Peterson, L. Warden, and X. Xie, "High-Sensitivity Detection of DNA Hybridization on Microarrays Using Resonance Light Scattering", Anal. Chem. **74**, 1792 (2002).

[4] Federal Bureau of Investigation, "Quality Assurance Standards for Forensic DNA Testing Laboratories" and "Quality Assurance Standards for Convicted Offender DNA Databasing Laboratories," Forensic Sci. Commun. **2**, 1 (2000).

[5] D.-S. Kim, Y. T. Jeong, H. K. Lyu, H.-J. Park, J.-K. Shin, P. Choi, J. H. Lee, G. Lim, "An FET-type charge sensor for highly sensitive detection of DNA sequence", Biosens. Bioelectron. **20**, 69 (2004).

[6] B. S. Kang, S. J. Pearton, J. J. Chen, F. Ren, J. W. Johnson, R. J. Therrien, P. Rajagopal, J. C. Roberts, E. L. Piner, and K. J. Linthicum, "Electrical detection of deoxyribonucleic acid hybridization with AlGaN/GaN high electron mobility transistors", Appl. Phys. Lett. **89**, 122102 (2006).

[7] S. Alur, R. Thapa, T. Ganaprakasa, Y. Wang, Y. Sharma, E. Javalosa, E. Smith, C. Ahyi, A. Simonian, M. Bozack, J. Williams, M. Park, "DNA hybridization sensor based on AlGaN/GaN HEMT", Phys. Status Solidi C **8**, 2483 (2011).

[8] A. V. Vertiatchikh and L. F. Eastman, "Effect of the surface and barrier defects on the AlGaN/GaN HEMT low-frequency noise performance," IEEE Electron Device Lett. **24**, 535 (2003).

[9] H. Hasegawa, T. Inagaki, S. Ootomo, and T. Hashizume, "Mechanisms of current collapse and gate leakage currents in AlGaN/GaN heterostructure field effect transistors," J. Vac. Sci. Technol. B, Microelectron. Process. Phenom. **21**, 1844 (2003).

[10] G. Meneghesso, G. Verzellesi, F. Danesin, F. Rampazzo, F. Zanon, A. Tazzoli, M. Meneghini, and E. Zanoni, "Reliability of GaN high- electron-mobility transistors: State of the art and perspectives," IEEE Trans. Device Mater. Rel. **8**, 332 (2008).

[11] W. Saito, M. Kuraguchi, Y. Takada, K. Tsuda, I. Omura, and T. Ogura, "High breakdown voltage undoped AlGaN–GaN power HEMT on sapphire substrate and its demonstration for DC–DC converter application," IEEE Trans. Electron Devices **51**, 1913 (2004).

[12] W. Saito, M. Kuraguchi, Y. Takada, K. Tsuda, I. Omura, and T. Ogura, "Influence of surface defect charge at AlGaN–GaN-HEMT upon Schottky gate leakage current and breakdown voltage," IEEE Trans. Electron Devices **52**, 159 (2005).

[13] X. Donglin, L. Meidong, Z. Yike, L. Churong, C. Shi, L. Shaobo, H. Yangiu, "fabrication and electrical properties of lead zirconate titanate thick films using a new sol-gel processing technique," J. Mat. Sci. **12**, 587 (2001).

[14] C. A. Barlow Jr. and J. R. Macdonald, "Theory of discreetness of charge effects in the electrolyte compact double layer", Adv. Electrochem. Electrochem. Eng. **6**, 1 (1967).

[15] G. Gouy, J. Phys. Radium **9**, 457 (1910).

[16] D. L. Chapman, "A contribution to the theory of electrocapillarity**"** Philos. Mag., **25**, 475 (1913).

[17] O. Stem, "Zur Theorie der elektrolytischen Doppelschicht" Z. Elektrochem., **30**, 508 (1924).

[18] V. Lockett, R. Sedev, J. Ralston, M. Horne and T, Rodopoulos, "Differential Capacitance of the Electrical Double Layer in Imidazolium-Based Ionic Liquids: Influence of Potential, Cation Size, and Temperature" J. Phys. Chem. C 112, 7486 (2008).

[19] R. J. Hunter, "Foundations of Colloid Science", Clarendon Press: Oxford, U.K., vol 1 (1987).

[20] K. B. Oldham, "A Gouy–Chapman–Stern model of the double layer at a (metal)/(ionic liquid) interface", J. Electroanal. Chem. 613, 131 (2008).

[21] A. J. Bard and L. R. Faulkner, "Electrochemical Methods, Fundamentals and Ap-

plications", John Wiley & Sons, New York, NY, second edition, (2001).

[22] A. Kitahara and A. Watanabe, "Electrical Phenomena at Interfaces", Marcel Dekker, Inc., New York, NY (1984).

[23] A. J. Bard and L. R. Faulkner, "Electrochemical Methods, Fundamentals and Applications", John Wiley & Sons, New York, NY, second edition, (2001).

[24] J. O. Bockris, M. A. V. Devanathan, and K. Muller, "On the structure of charged interfaces", J. Am. Chem. Soc. **274**, 55 (1963).

[25] L. Ouellette, "Chemical and biological sensing with carbon nanotube in solution", PhD Thesis, Cornell University, Ithaca, NY (2008).

## Chapter 2

## Nitride semiconductor: background and literature review

### 2.1 Introduction

Due to its lower material cost, higher level of integration capabilities and matured technology, silicon (Si) is still the workhorse material in the current semiconductor market. Si based technology has enjoyed the steady improvements over the decades and is poised to remain at the front in the mainstream market. The 22 nm node technology is in the phase of commercial production and the 11 nm node is expected to reach the market by 2015.[1] With the progress in the scaling and innovative device optimization techniques, Si is able to satisfy applications requiring low power and lower end of the microwave frequency. In addition, by alloying with other suitable semiconductor such as Germanium (Ge), the performance of Si technology has been increased significantly to accommodate specific applications.[2] On the other hand, compound semiconductor material such as GaAs has been introduced to overcome the limited intrinsic material capabilities of Si.[3] As compared to silicon, GaAs offers better device functionality in terms of faster low-field electron mobility (~ 8500 $cm^2/V.s$), high saturation velocity (~ $2\times10^7$ cm/s), and is also a direct band gap material. GaAs heterostructure based devices have achieved considerable success in the field of optoelectronic and high frequency devices. Arsenic and Phosphorous based light emitting diodes (LEDs) and laser diodes (LDs) have been successfully used to obtain infrared to yellow (As based) and green (P

based) part of the spectrum. Even with these advantages, GaAs cannot out-compete Si in terms of integration capabilities and availabilities. Also, small energy band gap of the conventional semiconductor materials results in a low electric breakdown field (Si ~ 0.3MV/cm, GaAs ~ 0.4MV/cm). This severely limits the capabilities of the device for the use in high power and high temperature application. Although SiC has emerged to address the performance and capability plateau of the Si based devices, the cost structure severely limits its widespread applications.[4] As the device scaling continues further, quantum mechanical effect needs to be accounted on the device behavior. With the fewer and fewer atoms in the device, position of impurities and other irregularities begin to affect the device performance variation and reliability.[5] In addition, cost effective lithography will be an issue at the highly-scaled nodes. So, instead of shrinking the device, new device structure based on a superior material system could better suit the problem.

With the progress in the semiconductor technology, the demand for high linearity, high frequency and high efficiency devices are increasing. As the Si based technology reaches its theoretical limits, gallium nitride based technology appears to be ready to continue to provide the significant improvement in performance enjoyed by the semiconductor industry for the past 40 years. Due to its inherent material characteristics, GaN heterostructure based devices are superior to the currently available Silicon and other III-V technology. The combination of key parameters such as high power, high frequency, high speed, high temperature, low noise, etc. either exceeds or matches the available semiconductor solution. Higher power/power density devices enable the use of fewer and smaller devices, thus leaving behind a smaller system footprint with overall

system reliability. As the electrons have much higher mobility in III-Nitride heterostructure semiconductor based devices, they possess high frequency capability than the Si based devices. Higher frequency gives a greater conversion efficiency (AC to DC and vice versa), and smaller passive components (capacitors, inductors, etc.) for smaller, lighter overall system. These devices can operate at higher temperature which translates to the less auxiliary cooling. Lower internal loss increases the power transmission efficiency and less heat will be generated. These features make GaN suitable for the application in analog, RF (radio frequency), power converter/regulator, and sensor paradigms. Key advantageous features of the GaN over the conventional semiconductor materials such as GaAs and Si are depicted in the Fig. 1.

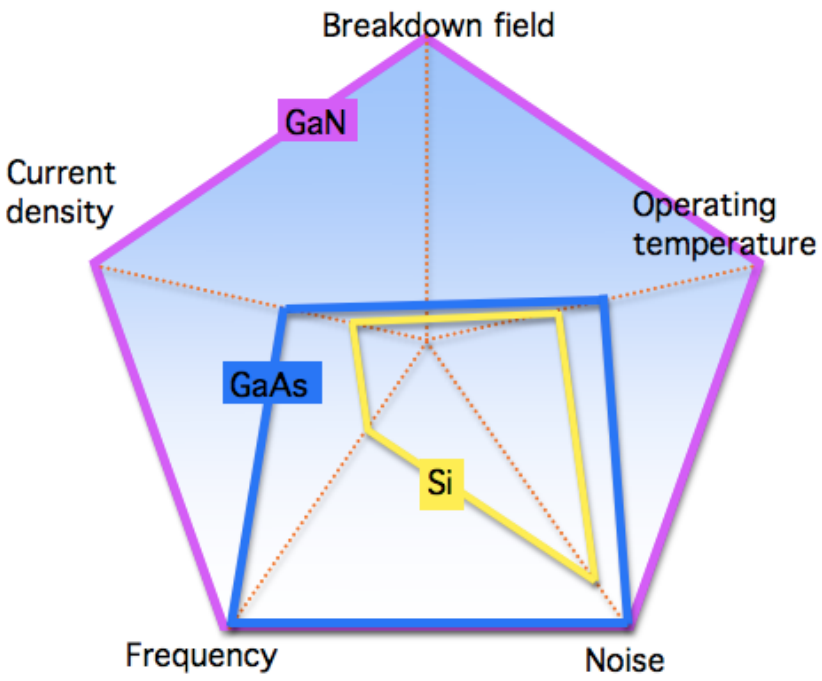


Fig. 2.1 Performance comparison of key semiconducting materials.

The characterization of a semiconductor material as a wide band gap pertains to the energy that an electron requires to jump from the top of the valance band to the bottom of the conduction band within the semiconductor. Typically, semiconductors with electronic energy bandgap larger than two electron volt (eV) are referred as a wide bandgap semiconductor. The wide bandgap results in a higher breakdown field, critical for a high power application. In this perspective, compound semiconductors such as SiC, GaN both provide high breakdown electric field. Higher thermal conductivity of SiC gives it an edge on high power and high voltage switching applications, whereas higher electron mobility of GaN makes it a better-suited material system for the high frequency application.

The performance of the devices are essentially based on the electrical, optical, thermal, and mechanical properties of the semiconductor material on which the devices are fabricated and often expressed in terms of the figure of merits (FOM). The FOM allows the simple comparison between the similar systems in terms of physical parameters. Table 2.1 shows the normalized FOM with respect to Si for the most common semiconducting materials with the larger number indicating the better performance.[6,7,8] In table 2.1, $E_C$ is the critical electrical field for breakdown in semiconducting material, $v_S$ is the electron saturation velocity, $\kappa$ is the thermal conductivity, $c$ is the speed of light, $\epsilon$ is the dielectric constant of the semiconductor, $\mu$ is the mobility of the charge carrier, and $E_G$ is the bandgap energy (in eV). Among the common semiconducting materials, GaN has the highest combined figure of merit (CFOM), making it suitable for the high power, high temperature and high frequency applications.

| *FIGURE OF MERITS* | *EXPRESSION* | Si | GaAs | SiC-4H | GaN | *FEATURES* |
|---|---|---|---|---|---|---|
| **COMBINED** | $\kappa \epsilon \mu v_s E_C^2$ | 1 | 3.6 | 358 | 520 | Overall performance |
| **KEYS** | $\kappa\sqrt{c.v_s/4\pi\epsilon}$ | 1 | 0.41 | 4.61 | 1.6 | Power density& speed |
| **BALIGA** | $\epsilon \mu E_G^3$ | 1 | 13.3 | 548 | 1507 | Resistive losses |
| **BALIGA HIGH FREQUENCY** | $\mu E_C^2$ | 1 | 9.5 | 22.9 | 77.8 | Switching losses |

Table 2.1 Figure of merits comparison of the common semiconducting materials.

Lately, compound semiconductor, in particular GaN based devices have been the subjects of intense research. They bring remarkable performance and size advantage over the Si technology. However, commercialization has been greatly impeded by the cost involved in the material growth. In order to be successful, GaN technology must be cost competitive with the conventional technology. For this, GaN wafer must be grown into a large diameter low cost substrate. So far GaN technology lacks the bulk substrate in the commercial size at reasonable cost. For this reason, mostly it has to be grown on the foreign substrate such as SiC, sapphire, Si, etc. This presents a series of problems due to the mismatch in the physical properties between the substrate and the GaN itself. GaN grown on sapphire substrate suffers from a large lattice mismatch, and low thermal

conductivity limiting the device performance. However, lower cost, robustness, higher melting point, transparency in the ultraviolet to infrared regions makes it an acceptable substrate. Moreover, SiC offers better thermal conductivity and lower defect density, but is less cost effective. On the other hand, Si substrate in general provides better option in terms of lower cost and larger substrate size. Nevertheless, larger lattice mismatch introduces higher defect densities in the crystal and negatively affects the device performance. Important physical parameters of the substrates used in the GaN heteroepitaxy are shown in the table 2.2.

| Material | Structure | Lattice constants (Å) | | | Thermal expansion coefficient ($10^{-6}$ $K^{-1}$) |
|---|---|---|---|---|---|
| | | a | b | c | |
| **w-GaN** | Wurtzite | 3.185 | | 5.185 | 5.45 |
| **SiC-6H** | Wurtzite | 3.080 | 15.117 | | 4.46 |
| **Si** | Diamond | 5.431 | | | 3.59 |
| **$Al_2O_3$** | Rhombohedral | 4.758 | | 12.982 | 7.50 |
| **w-AlN** | Wurtzite | 3.110 | | 4.979 | 2.2 |

Table 2.2 Physical properties of common substrates used in the GaN heteroepitaxy.

III-Nitride semiconductors, such as, GaN have distinct advantages over other non-heterogeneous semiconductor like Silicon Carbide (SiC). Though both are wide bandgap semiconducting material suitable for high power and high frequency applications, GaN based semiconductors can form heterojunction, which creates a triangular potential well

at the interface. The electrons accumulated in the potential well constitute a two-dimensional electron gas (2DEG). The electrons in the 2DEG gas possess an increased mobility in comparison to the electrons in the bulk of the active material. Unlike SiC MOSFET, the mobility of the confined electrons in the potential well will be less affected by the surfaces and interfaces in the heterostructure based devices. The key material parameters of GaN, as well as other competing semiconducting materials, are shown in the table 2.3.

| **Semiconducting Material** | | **Silicon (Si)** | **Germanium (Ge)** | **Gallium Arsenide (GaAs)** | **Silicon Carbide (SiC-4H)** | **Gallium Nitride (GaN)** |
|---|---|---|---|---|---|---|
| **Properties** | Unit | | | | | |
| **Bandgap** | eV | 1.1 | 0.66 | 1.42 | 3.26 | 3.45 |
| **Mobility at 300 K (μ)** | $cm^2/V.s$ | 1500 (e)<br>450 (hole) | 3900 (e)<br>1900 (hole) | 8500 (e)<br>400 (hole) | 700 (e) | 1000-2000(e)<br>30 (hole) |
| **Critical electric field** | MV/cm | 0.3 | 0.1 | 0.4 | 3 | 3.3 |
| **Saturated (peak) electron velocity** | $\times 10^7$ cm/s | 1.0<br>(1.0) | | 1.3<br>(2.0) | 2.0<br>(2.2) | 2.5<br>(3.1) |
| **Thermal conductivity** | W/cm. K | 1.5 | 0.6 | 0.5 | 4.5 | > 1.5 |

Table 2.3 Key material parameters of various semiconducting materials.[9]

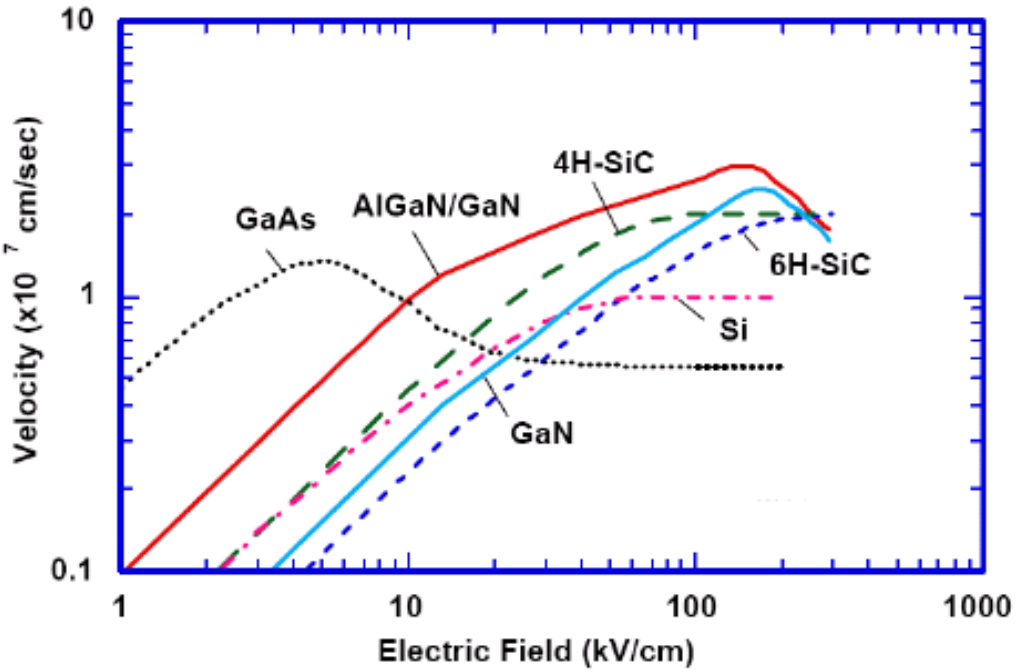


Fig. 2.2 Electron velocity vs. electric field characteristics of various semiconductors.[10]

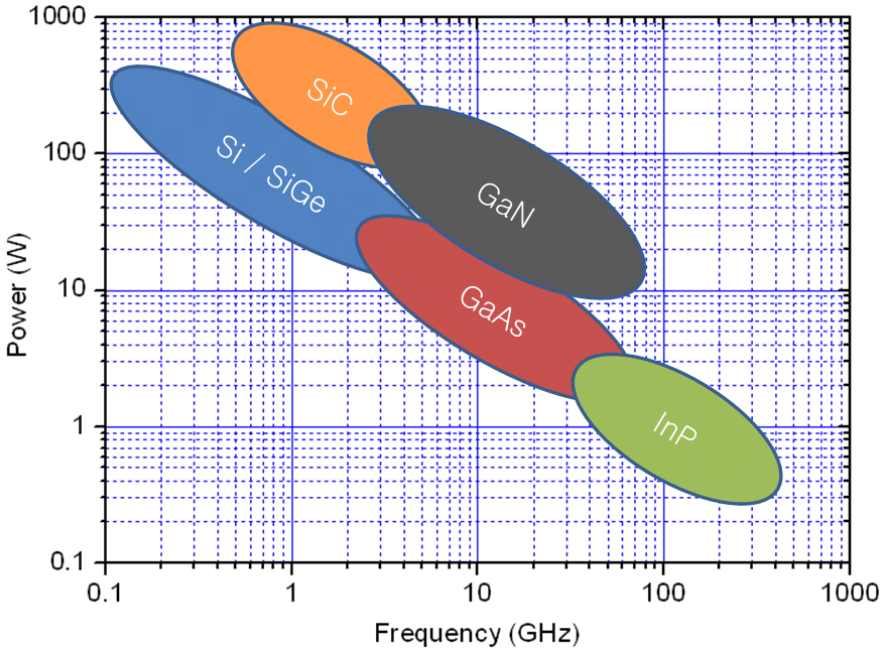


Fig. 2.3 Power and frequency capabilities of common semiconducting materials. (Reproduced from[11])

At higher electric field, velocity of the carriers essentially is the saturated drift velocity ($v_{sat}$). This property is very important for the device to operate in the high frequency and high power applications. As depicted in the Fig. 2.2, saturated drift velocity in Si and GaAs are limited within the values of $1\times10^7\ cm/sec$, whereas bulk GaN has higher value of $1.4\times10^7\ cm/sec$.[12] This value is even higher in case of AlGaN/GaN heterostructure due to the formation of the 2 dimensional electron gas at the heterojunction. In addition, GaN offers the better capabilities in the power vs. frequency spectrum as shown in Fig. 2.3 making it promising material system for high power and high frequency application.

**2.2 Applications**

GaN is a wide bandgap semiconducting material, which is piezoelectric, biocompatible, and also resistant to ionizing radiation. Material properties such as direct bandgap, chemical/thermal stability, higher mobility, higher saturation velocity makes it an auspicious material for use in electronics, optoelectronics and bioelectronics based applications. Application area of GaN based devices span from household consumer electronics to military applications.

Violet and blue lasers based on GaN technology are the preferred type of lasers for imaging and data storage applications. The relatively shorter wavelength (blue laser – 405 nm) allows the storage of greater amount of data in the same size that has been used by conventional semiconductor laser (GaAs based red laser – 650 nm). In addition, GaN based solid-state light emitting diodes (LEDs) are used to build full color display with

higher efficiency. Also, the steady improvements in the solid-state electronic devices are getting further push with the incorporation of the superior semiconducting materials such as GaN. Next generation power amplifiers and communication system based on GaN will help to improve the efficiency, reduce the size, and simplify the overall fabrication process. In addition, superior chemical/thermal stability, non-toxicity to the living cells, highly sensitive due to the two dimensional electron gas (2DEG) lying very proximity to the surface etc. make the GaN based devices a highly desirable for the sensor application.[13,14]

### 2.3 GaN crystal structure

III-Nitride semiconductors can crystallize in wurtzite (Wz) hexagonal close pack structure, zinc blende (ZB) cubic crystal structure and rock salt (NaCl) structure.[15] However, wurtzite structure is the thermodynamically stable structure for bulk AlN, InN, and GaN.[16] Nonetheless, zinc blende structure of GaN and InN can be epitaxially grown on $\{011\}$ crystal planes of cubic substrate such as Si, SiC, GaAs. On the other hand, existence of rock salt structure is possible at high-pressure condition and is not very useful for practical application.[17,18] Wurtzite crystal structure is a hexagonal close pack (HCP) structure with a single lattice basis. This structure is fully described with the use of three lattice parameters $\vec{a}$, $\vec{c}$ and $\vec{u}$. The hexagonal basal length is denoted as $\vec{a}$, height of the unit cell as $\vec{c}$ and the internal dimensionless parameter representing the Ga and N bond-length in the multiplicity of $\vec{c}$ as $\vec{u}$. In the case of ideal HCP lattice structure, $\vec{c}/\vec{a} = \sqrt{8/3}$. GaN in wurtzite structure can be of two different polarities along the $[0001]$ direction and $[000\bar{1}]$ direction. In the $[0001]$ polarity crystal, the top surface

contains the Ga atom and is called the Ga-polarity; whereas in the $[000\bar{1}]$ polarity crystal, the top surface contains the N atom and is referred as the N-polarity as shown in Fig 2.4. These two faces are not equivalent to each other and thus give the different physical and chemical properties to the crystal. The basic GaN crystal parameters for the wurtzite and zinc blende structure at room temperature are given in table 2.4.

| Property | GaN Hexagonal | GaN Cubic |
|---|---|---|
| Structure | Wurtzite | Zinc Blende |
| Stability | Stable | Meta-stable |
| Lattice constants (300K) | a = 0.3189 nm<br>c = 0.5185 nm | 0.450 nm |
| Density (300K) | 6.095 $g.cm^{-3}$ | 6.100 $g.cm^{-3}$ |
| Linear Thermal Expansion Coefficient (300 K) | a: $5.59x10^{-6}$ $K^{-1}$<br>c: $7.75x10^{-6}$ $K^{-1}$ | -- |
| Refractive Index | 2.67 at 3.38 eV | 2.9 at 3 eV |
| Energy Gap (300K) | 3.45 eV | 3.23 eV |
| Bandgap nature | Direct | Direct |

Table 2.4 Material properties for wurtzite and zinc blende structure of GaN.[19]

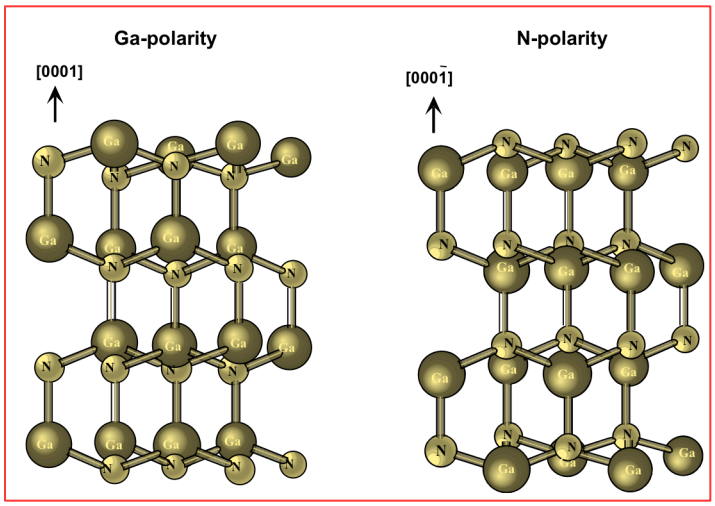


Fig 2.4 GaN crystal structure. (reproduced from[20])

## 2.4 Polarization in GaN

Polar semiconductors with wurtzite crystal structure, such as GaN, AlN and InN exhibit macroscopic polarization properties. The separation of center of negative charges due to the electron cloud and center of positive charge due to atomic nuclei constitutes an atomic dipole with a dipole moment $\vec{p}$. The polarization state of the material is then defined as the dipole moment per unit volume and expressed as

$$\vec{P} = \sum_i N_i \langle \vec{p}_i \rangle \qquad [2.1]$$

where $\vec{P}$ is the total polarization, $\langle \vec{p}_i \rangle$ is the average dipole moment of the $i^{th}$ atom, and $N$ is the average number of dipoles per unit volume. The polarization field in semiconductor allows the suitable tailoring of the carrier dynamics and optical properties of the devices. The large ionicity of the Ga-N bond and the noncentrosymmetric nature (the [0001] and [000$\bar{1}$] directions are crystallographically distinct) causes a very large component of the

spontaneous polarization in the material with a net dipole along the $\vec{c}$ axis. For the ideal wurtzite crystal structure, $\vec{u}$ assumes a value of 0.375, whereas $\overrightarrow{c_0}/\overrightarrow{a_0}$ ratio has a value of 1.633. However, an experimental value of both $\vec{u}_0$ and $\overrightarrow{c_0}/\overrightarrow{a_0}$ deviates from the ideality and gives rise to the spontaneous polarization. As the lattice non-ideality factor increases, parameter $\overrightarrow{c_0}/\overrightarrow{a_0}$ deviates from the ideal value and the spontaneous polarization increases. The theoretical values for the magnitude of the spontaneous polarization of the binary nitrides are given in the table 2.5.

| Parameter | GaN | InN | AlN | Ideal |
|---|---|---|---|---|
| $\overrightarrow{c_0}/\overrightarrow{a_0}$ | 1.6259 | 1.6116 | 1.6010 | 1.633 |
| Spontaneous polarization($C/m^2$) | -0.081 | -0.032 | -0.029 | - |

Table 2.5 Lattice non-ideality and spontaneous polarization value of the nitrides.[21,22]

## 2.5 Heterostructure physics

Heterostructure consist of two or more layers of different semiconducting materials grown on top of each other. The interface between these layers is commonly referred as heterojunction or heterointerface. The property of such a heterostructure depends upon the physical parameters of the epitaxial layers, such as lattice constants, crystal structure, band gap, etc. and plays an important role in heterostructure devices including field effect transistors (FET), bipolar junction transistors (BJT), lasers and light emitting diodes (LED). When two semiconducting materials are brought in physical contact, the alignment of the interface gap can be straddled (type I), staggered (type II) or

broken (type III), depending upon the energy gap as a result of the specific semiconducting materials.

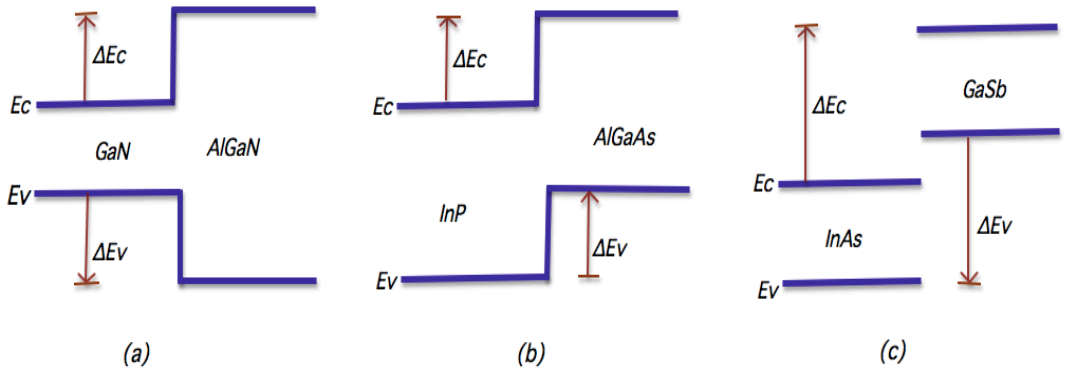


Fig. 2.5 Types of heterostructure energy band alignments: (a) Type I or straddled structure (b) Type II or staggered structure (c) Type III or broken structure.

Consider two semiconducting materials forming a heterostructure with different energy band gaps $E_{G1}$ and $E_{G2}$. Because of the difference in the energy band gaps, the conduction and valance bands of the two materials becomes discontinuous across the heterointerface. The difference in the energy between the conduction band edge and the valence band edge at the interface is called the conduction band offset $\Delta E_C$ and valence band offset $\Delta E_V$.

Heterostructures are classified according to the alignment profile of the conduction and valance bands of the two semiconductors as types I, II and III. The most common heterostructure is the type I or straddled alignment as in the AlGaN/GaN and AlGaAs/GaAs material system as sketched in Fig. 2.5(a). In this alignment, the band gap

of the wider band gap material entirely overlaps the band gap of the smaller band gap material and the sum of the conduction band offset and valence band offset is equal to the difference in the energy band gap $\Delta E_G$.

Fig. 2.5(b) shows the staggered alignment of the semiconductor heterostructure energy bands. In this type of the alignment, the step of the valence and the conduction energy bands goes in the same direction. The valence band of the smaller gap material might lie below that of the larger gap material or the conduction band might lie above that of the larger gap material. The energy band gap offset is equal to the difference between the conduction band offset and valence band offset. When the staggering becomes extreme and band gaps cease to overlap, resulting alignment is called broken gap alignment as shown in Fig. 2.5(c). Some experimentally determined band alignment values for each of the heterojunctions are shown in the Fig. 2.6 below[23]

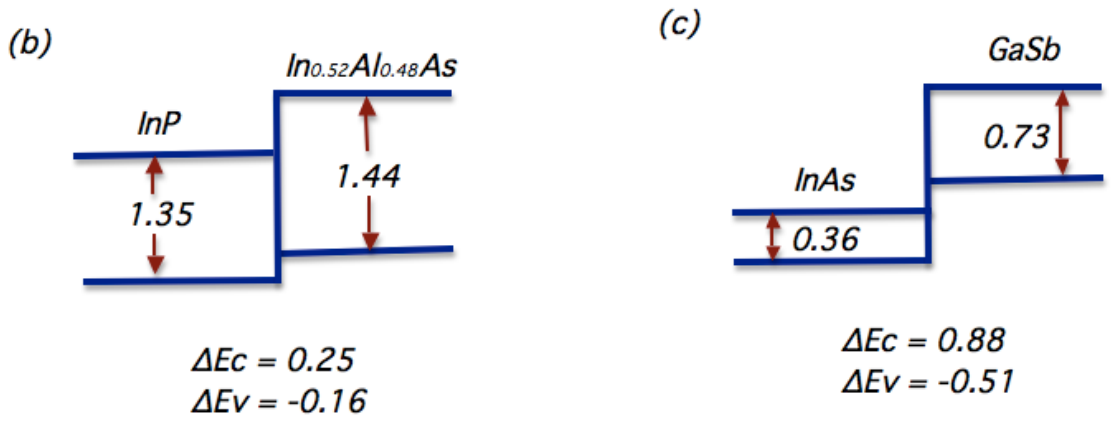


Figure 2.6 Experimental values for the heterostructure band offsets (a) straddled alignments (b) staggered alignments (c) broken alignments in electron volts (eV).

## 2.6 AlGaN/GaN heterostructure

Nitride semiconductors, in particular GaN and its heterostructure with AlGaN, offers remarkable material properties suitable for the fabrication of the high performance electronics, optoelectronics and bioelectronics devices. The AlGaN/GaN heterostructure is created when a thin AlGaN barrier layer (doped or undoped) is grown on top of a relatively thick GaN layer. This material structure, which forms a heterostructure, has different energy band gaps $E_g$, work functions $q\varphi_s$, permitivities $\epsilon_s$, electron affinities $\chi_s$, and the resulting band structure determines the behavior of the devices. In AlGaN/GaN heterostructure, AlGaN is the wider band gap semiconductor and GaN is the narrower band gap semiconductor. At the interface of the two semiconductors, there will be a band gap discontinuity $\Delta E_g$, arising from the differences in the band gap energies of the two materials and given as

$$\Delta E_g = \Delta E_c + \Delta E_v \qquad [2.2]$$

with $\Delta E_c$ being the conduction band offset and $\Delta E_v$ being the valence band offset. The discontinuity in the conduction band creates a triangular potential well with the highly mobile two dimensional electron gas (2DEG), which will be described in detail later. The band diagram in Fig. 2.7 shows a sharp dip in the conduction band edge at the AlGaN/GaN heterointerface. Due to the relatively small thickness of the potential well as compared to the length and the width, the electronic states of the 2DEG are in discrete state perpendicular to the interface. On the other hand, they exhibit a continuous distribution in two dimensions parallel to the interface.

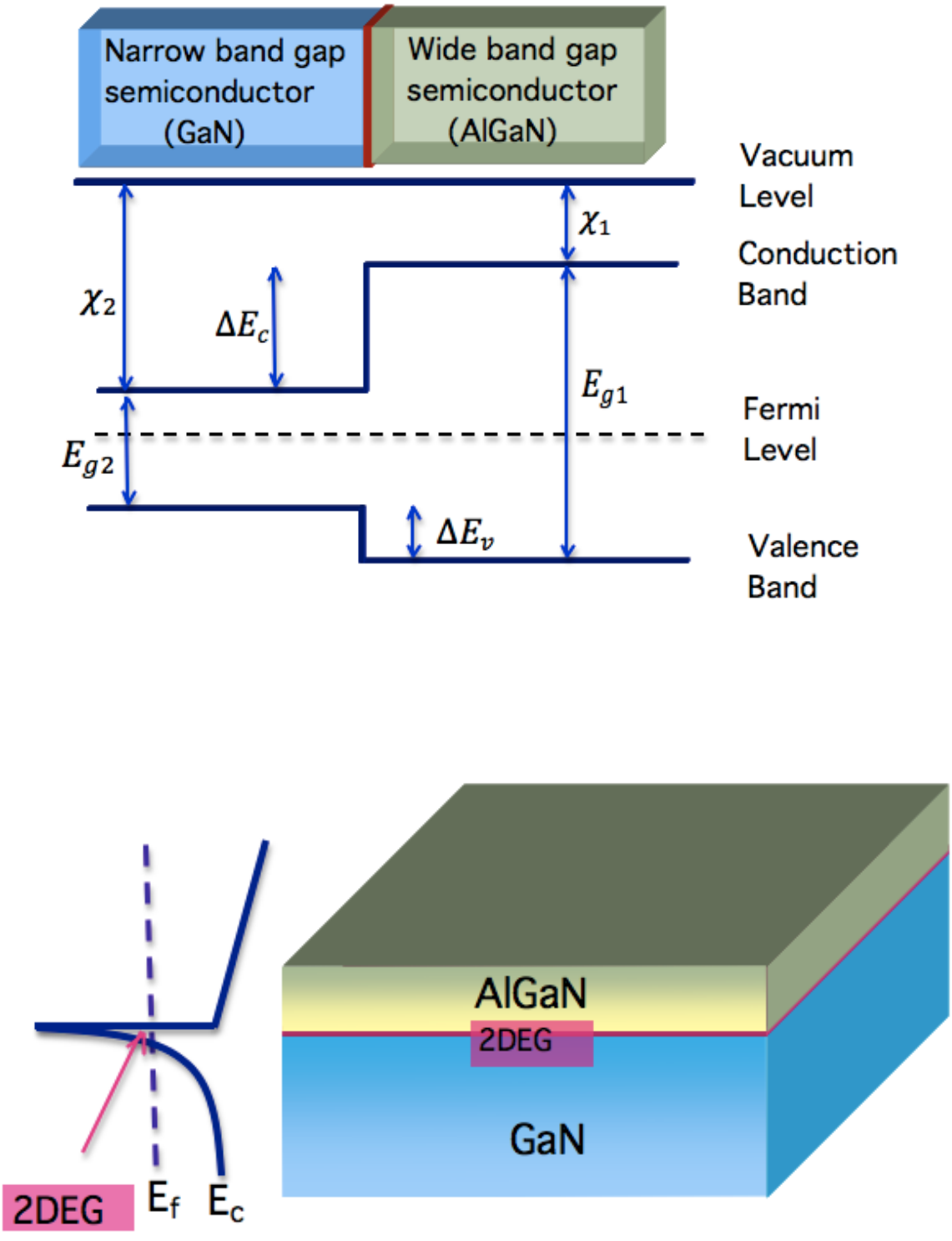


Fig. 2.7 Schematic band structure of AlGaN/GaN heterostructure.

AlGaN/GaN heterostructure exhibits a strong polarization field creating a 2DEG sheet carrier density ($n_s$) in the order of $\sim 10^{13}\ cm^{-2}$ at the interface even without an intentional doping. This sheet charge density is roughly four to five times higher than that of AlGaAs/GaAs heterostructure. This helps to increase the device's current handling capabilities. Further, GaN possesses an energy band gap value of 3.4 eV, which will be even higher for its alloyed compounds like AlGaN. This feature enables the GaN based heterostructure devices to support peak internal electric fields about ten times higher than that of silicon and gallium arsenide.[24] Higher electric field strength results in a higher electrical breakdown voltage, a requirement for high power devices. A higher electron saturation velocity minimizes the internal device delays. All these fortuitous combination makes GaN and its associated heterostructure suitable for high power, high frequency and high temperature application. The sheet carrier density at the interface depends upon parameters, such as thickness of the epitaxial AlGaN layer, Al mole fraction, surface states, which will be discussed in section 2.10.

**2.7 Polarization in AlGaN/GaN heterostructure**

Two types of polarization, namely the spontaneous polarization ($\vec{P}_{SP}$) & the piezoelectric polarization ($\vec{P}_{PZ}$) contribute to the total macroscopic polarization in the AlGaN/GaN heterostructure.

$$\vec{P} = \vec{P}_{SP} + \vec{P}_{PZ} \qquad [2.3]$$

Since Ga and N atoms do not lie on the same plane, AlGaN and GaN wurtzite crystal

structure is asymmetric along the [0001] direction. Because of this lack of symmetry and the large ionicity of the covalent bond in wurtzite structure, a large spontaneous polarization exists along the [0001] direction. This spontaneous polarization is the built in polarization field that exists in the unstrained crystal and is the intrinsic property of the III-Nitrides.

Piezoelectric polarization arises from the lattice constant mismatch at the heterointerface and increases with the increase in the strain at the interface. As the lattice constant of the AlN and GaN crystal are sufficiently different, the AlGaN layer, which is grown pseudomorphically on top of the GaN layer, gets strained. This deformation of lattice at the heterointerface induces the piezoelectric polarization. The spontaneous and piezoelectric polarization in GaN wurtzite crystal structure can be expressed as

$$\vec{P}_{SP} = P_{SP}\vec{z} \quad [2.4]$$

$$\vec{P}_{PZ} = e_{33}\boldsymbol{\epsilon_z} + e_{31}\left(\boldsymbol{\epsilon_x} + \boldsymbol{\epsilon_y}\right) \quad [2.5]$$

$$\epsilon_z = (c - c_0)/c_0 \quad [2.6]$$

$$\epsilon_x = \epsilon_y = (a - a_0)/a_0 \quad [2.7]$$

where $\vec{z}$ is the direction of the epitaxial layer growth, $\vec{x}$ and $\vec{y}$ are the direction of the basal plane perpendicular to the crystal growth, $a_0$ & $c_0$ are the lattice constant of the unstrained structure, $a$ & $c$ are the lattice constant of the strained structure, $\epsilon_z$ is the strain along the [0001] or $\vec{z}$ direction, $\epsilon_x = \epsilon_y$ are the basal plane strain along the $\vec{x}$ and $\vec{y}$ direction, $e_{33}$ & $e_{31}$ are the piezoelectric coefficients as given in the table 2.6.[25,26,27]

The relation between the lattice constants is given as

$$\frac{c - c_0}{c_0} = -2\,\frac{C_{13}}{C_{33}}\,\frac{a - a_0}{a_0} \qquad [2.8]$$

where $C_{13}$ and $C_{33}$ are the elastic constants as given in Table 2.6. Using Equation [2.8] and [2.5], we get the total piezoelectric polarization as

$$\vec{P}_{PZ} = 2\,\frac{a - a_0}{a_0}\left(e_{31} - e_{33}\,\frac{C_{13}}{C_{33}}\right)\vec{z}. \qquad [2.9]$$

The Ga-face AlN and GaN wurtzite crystal structure has negative spontaneous polarization (pointing towards the substrate), whereas the N-face structure has it in the opposite direction. For Ga-face GaN and AlN wurtzite structure, $(e_{31} - e_{33}\,C_{13}/C_{33}) < 0$. Thus the piezoelectric polarization is negative for tensile $(a > a_0, c < c_0)$, and positive for compressive $(a < a_0, c > c_0)$ strained barriers. As stated above, total polarization in the AlGaN/GaN heterostructure is the sum of the spontaneous and piezoelectric polarizations. If the polarizations orient in the opposite direction, its effect will be in the reduction in the net polarization. Thus, for the higher confinement of the 2 dimensional electron gas (2DEG) at the interface, polarizations should orient in the same direction as depicted in Fig. 2.8 (b). When the polarity changes from Ga-face to N-face, the sign of spontaneous and piezoelectric polarization also changes accordingly. As a consequence, confinement of the electrons at the interface becomes difficult.

| Parameter | AlN | GaN |
|---|---|---|
| $a_0(\text{Å})$ | 3.112 | 3.189 |
| $c_0(\text{Å})$ | 4.982 | 5.185 |
| $e_{31}\ (C/m^2)$ | - 0.600 | - 0.490 |
| $e_{33}\ (C/m^2)$ | 1.460 | 0.730 |
| $C_{13}\ (GPa)$ | 120[a] ,108[b] | 70[a] , 103[b] |
| $C_{33}\ (GPa)$ | 395[a] , 373[b] | 379[a] , 405[b] |
| $\vec{P}_{SP}(C/m^2)$ | - 0.081 | - 0.029 |
| | [a]Experimental | [b]Calculated |

Table 2.6 Lattice parameters for AlN and GaN wurtzite crystal structure.[26,27,28]

In AlGaN/GaN heterostructure, the GaN layer is usually several orders of magnitude thicker than the AlGaN layer. It is assumed that bulk GaN is fully relaxed; therefore its polarization vector only contains the spontaneous polarization component $\vec{P}_{SP}^{GaN}$. On the other hand, in the AlGaN layer, in addition to the spontaneous component of the polarization $\vec{P}_{SP}^{AlGaN}$, strain induced piezoelectric component $\vec{P}_{PZ}^{AlGaN}$ also contributes to the total polarization as shown in Fig 2.8 (b). If both GaN and AlGaN layers are relaxed as in Fig. 2.8 (a), heterostructure lacks the piezoelectric polarization.

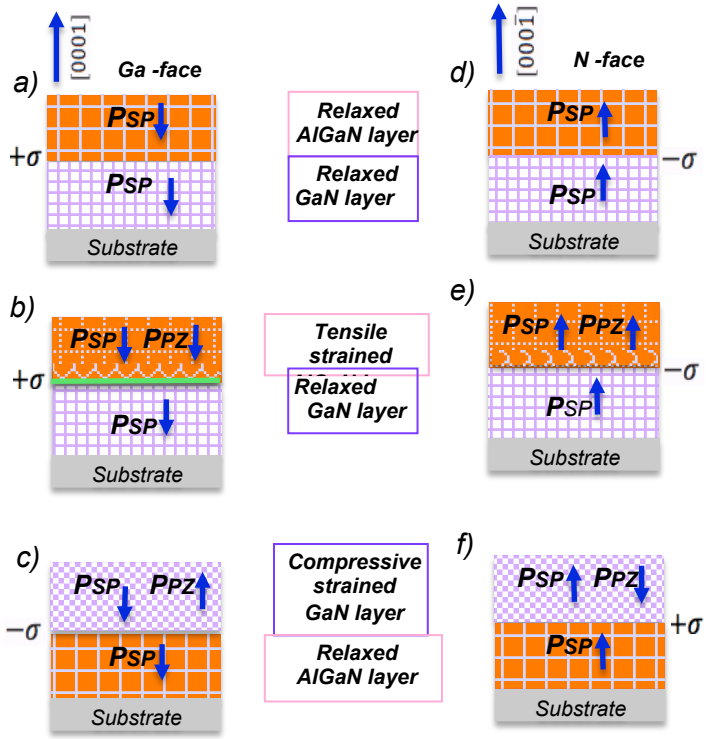


Figure 2.8 Spontaneous and piezoelectric polarization direction in Ga-face and N-face, strained and relaxed AlGaN/GaN heterostructures. (Adapted from [18])

## 2.8 Carrier density distribution in AlGaN/GaN heterostructure

Due to the difference in the spontaneous polarizations between the AlGaN & GaN, and piezoelectric polarization from the abrupt change in the strain at the heterointerface between these materials, polarization sheet charge density arises at the heterointerface. Using Gauss's law, polarization induced electrostatic charge density ($\rho_{pol}$) can be given as the spatial variation of sum of the spontaneous and piezoelectric polarization fields as[29]

$$\nabla . \vec{P} = \nabla . \left( \vec{P}_{SP} + \vec{P}_{PZ} \right) = - \rho_{pol} \qquad [2.10]$$

It is evident that the discontinuity in the polarization at the heterointerface is associated with the polarization sheet charge density ($\sigma_{int}$) as

$$\sigma_{int} = \vec{P}_{bottom} - \vec{P}_{top}$$

$$= \left( \vec{P}_{SP} + \vec{P}_{PZ} \right)_{bottom} - \left( \vec{P}_{SP} + \vec{P}_{PZ} \right)_{top}$$

$$= \left( \vec{P}_{SP} \right)_{GaN} - \left( \vec{P}_{SP} + \vec{P}_{PZ} \right)_{AlGaN} \qquad [2.11]$$

In the Ga-face AlGaN/GaN heterostructure, a positive bound sheet charge density $+\sigma$ will be present at the heterointerface and corresponding negative sheet charge density $-\sigma$ at the top part of AlGaN layer. To compensate the positive sheet charge density at the interface, electrons are attracted by this positive charges. Electrons that gets accumulated at the GaN side of the interface forms a conductive channel. The high electric field caused by this interfacial charge helps to form and confine the sheet carrier density called 2 dimensional electron gas (2DEG). Even if the relaxed heterostructure without the strain as depicted in Fig. 2.8 (a) (for thicker AlGaN barrier layer), the difference in the spontaneous polarization gives rise to the small amount of confined 2DEG at the GaN side of the interface. Whereas in Fig. 2.8(b), the pseudomorphically grown tensile strained thin AlGaN barrier layer gives rise the piezoelectric polarization. This increased discontinuity in total polarization charges increases the bound charge density ($\sigma_{int}$) at the interface and correspondingly the 2DEG sheet carrier density increases. If the GaN is grown on top of the relaxed AlGaN barrier layer, GaN gets compressively strained and

the resulting piezoelectric polarization has the reversed field direction as in Fig. 2.8 (c) and (f).

The total polarization induced sheet carrier density at the heterointerface as a function of Al mole fraction in $Al_xGa_{1-x}N$ barrier layer can be calculated in terms of linear interpolations between the physical properties of AlN and GaN, and deduced from the:[30]

lattice constants:

$$a_0(x) = (-0.077x + 3.189)10^{-10}\ m \qquad [2.12]$$

$$c_0(x) = (-0.203x + 5.189)10^{-10}\ m \qquad [2.13]$$

elastic constants:

$$c_{13}(x) = (5x + 103)\ Gpa \qquad [2.14]$$

$$c_{33}(x) = (-32x + 405)\ Gpa \qquad [2.15]$$

and spontaneous polarization

$$\vec{P}_{SP}(x) = (-0.052x - 0.029)\ {}^{C}/_{m^2} \qquad [2.16]$$

with $(x)$ being the amount of Al mole fraction in AlGaN barrier layer. By combining above equations, the general expression for the polarization induced sheet carrier density for both Ga-faced and N-faced AlGaN/GaN heterostructure is given as:

$$|\sigma(x)| = \left|\vec{P}_{PZ}(Al_xGa_{1-x}N) + \vec{P}_{SP}((Al_xGa_{1-x}N) - \vec{P}_{SP}(GaN)\right|,$$

$$|\sigma(x)| = \left|2\left(\frac{a(0)-a(x)}{a(x)}\right)\left\{e_{31}(x) - e_{33}(x)\frac{C_{13}(x)}{C_{33}(x)}\right\} + \vec{P}_{SP}(x) - \vec{P}_{SP}(0)\right| \quad [2.17]$$

## 2.9 Source of 2DEG sheet carrier concentration

In a strained and undoped Ga-face wurtzite AlGaN/GaN heterostructure, surface donor states of the AlGaN barrier layer are considered to be the source of 2DEG electrons.[31] The heterostructure contains the following space charge components as depicted in Fig. 2.9: 1) polarization induced charges at the AlGaN/GaN interface $(+\sigma)$ and AlGaN surface $(-\sigma)$ respectively; 2) negative charges due to the sheet electrons density $(n_s)$ at the 2DEG; 3) charges due to the ionized donors in the AlGaN layer $(+\sigma_{AlGaN})$; 4) charges due to the ionized surface states $(\sigma_{surface})$; and 5) buffer charges $(\sigma_{buffer})$ arising from the GaN buffer layer.

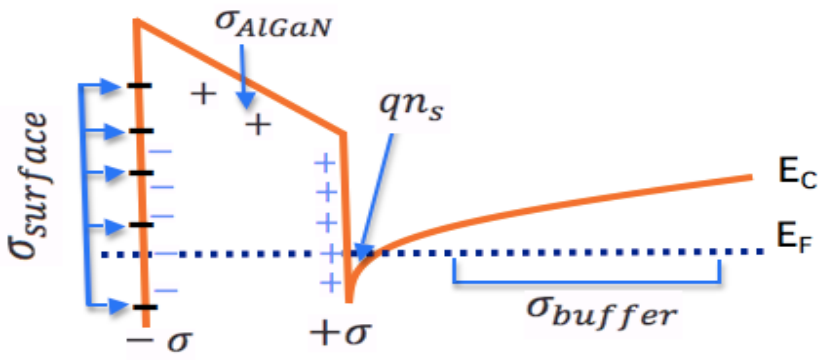


Fig. 2.9 Schematic illustration of the conduction band diagram of the AlGaN/GaN heterostructure showing various space charge components.

In the absence of an external electric field, the sum of the various space charge components in the heterostructure must be zero. Solving for the overall charge neutrality,

$$+\sigma - \sigma + \sigma_{AlGaN} + \sigma_{surface} - \sigma_{buffer} = qn_s \qquad [2.18]$$

With the polarization induced bound charges $\pm\sigma$ balancing each other owing to their dipole nature, their contribution in the 2DEG will be zero. For an undoped AlGaN barrier layer without ionized donors in it, $+\sigma_{AlGaN} = 0$. In addition, $\sigma_{buffer}$ must be negative in order to confine the 2DEG at the interface and its magnitude must be minimized for the well-designed device. Considering these assumptions, we can write

$$\sigma_{surface} = qn_s \, . \qquad [2.19]$$

Thus the total numbers of electrons in the 2DEG are equal to the numbers of ionized states in the surface and are most likely originated from the donor-like surface states. For an undoped $Al_xGa_{1-x}N$/GaN HFET structure with a Schottky contact, an analytical expression for the 2DEG sheet carrier concentration at the AlGaN/GaN interface as a function of the aluminum alloy composition $(x)$ of the $Al_xGa_{1-x}N$ barrier layer is given by[32],

$$n_s(x) = \frac{\sigma(x)}{e} - \left[\frac{\varepsilon_0 \varepsilon(x)}{d_{AlGaN} e^2}\right][e\varphi_b(x) + E_F(x) - \Delta E_c(x)] \qquad [2.20]$$

where $\sigma(x)$ is the polarization induced bound sheet charge density at the AlGaN/GaN heterojunction, $e$ is the charge of an electron, $\varepsilon_0$ is the permittivity of the free space, $\varepsilon(x)$ is the relative dielectric constant of the $Al_xGa_{1-x}N$ layer, $d_{AlGaN}$ is the thickness of the $Al_xGa_{1-x}N$ barrier layer, $e\varphi_b(x)$ is the Schottky barrier height, $E_F(x)$ is the Fermi level

energy with respect to the GaN conduction band-edge energy, and $\Delta E_c(x)$ is the conduction band offset at the $Al_xGa_{1-x}N/GaN$ interface.

The Fermi level $E_F(x)$ is given by[33]

$$E_F(x) = E_0(x) + \left[\frac{\pi\hbar^2}{m^*(x)}\right] n_s(x) \qquad [2.21]$$

where $m^*(x) \approx 0.22m_e$ is the effective electron mass and $E_0(x)$ is the ground state sub-band level of the 2DEG density and is given by

$$E_0(x) = \left[\frac{9\pi\hbar^2}{8\epsilon_0\sqrt{8m^*(x)}} \frac{n_s(x)}{\epsilon(x)}\right]^{2/3} \qquad [2.22]$$

and the band offset $\Delta E_c(x)$ is determined by[34]

$$\Delta E_c(x) = 0.7\left[E_g(x) - E_g(0)\right] \qquad [2.23]$$

Also, for AlGaN structure, the band gap energy $E_g(x)$ in $eV$ is given by[35]

$$E_g(x) = 6.13x + 3.42(1-x) - x(1-x) \qquad [2.24]$$

## 2.10 Factors influencing 2DEG density

### 2.10.1 Critical thickness of AlGaN barrier layer

In the AlGaN/GaN heterostructure with an undoped AlGaN barrier layer, polarization induced charges gives rise to a constant electric potential. Surface states from the thick barrier layer pin the surface potential, whereas they remain un-ionized for

the thin AlGaN barrier layer. With the assumption that donor-like surface states are positive when empty and neutral when occupied, the 2DEG density ($n_s$) depends upon the occupancy of the surface states and thus on its energy relative to the Fermi level ($E_F$). If these states lie sufficiently below the Fermi level, then their contribution to the 2DEG will be zero and there will be no 2DEG. When the barrier layer starts to grow, surface donor state energy ($E_D$) lies below the conduction band edge. With the increasing barrier thickness, ($E_F - E_D$) starts to decrease and reaches to a critical thickness given by[36]

$$t_{critical} = (E_D - \Delta E_C)\frac{\epsilon_{AlGaN}}{(+\sigma)q} \qquad [2.25]$$

where $E_D$ is the surface donor state energy, $\Delta E_C$ is the conduction band offset at the AlGaN/GaN interface, $+\sigma$ is the polarization induced bound charge density at the AlGaN/GaN interface, $\epsilon_{AlGaN}$ is the relative dielectric constant and $q$ is the charge of an electron.

At a critical thickness, donor state energy reaches up to the Fermi level and electrons from the occupied surface states start to move to the empty conduction band states. This process makes the surface states positive and creates the 2DEG at the AlGaN/GaN interface. With the increasing barrier thickness, the Fermi level remains at the surface donor energy states and more and more electron continue to transfer to the conduction band. In the case of barrier thickness ($t$) just beyond the critical thickness, 2DEG density ($n_s$) increases rapidly and gradually approaches to $+\sigma/q$ for $t \gg t_{critical}$ as given by the following equation.

$$qn_s = (+\sigma)\left[1 - \frac{t_{critical}}{t}\right] \qquad [2.26]$$

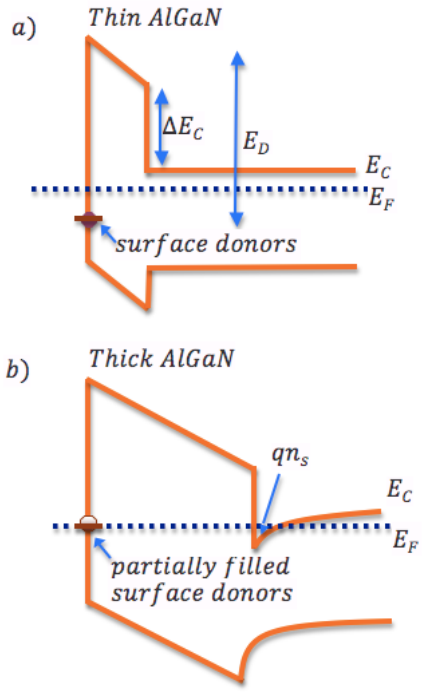


Figure 2.10 Schematic illustration of the surface donors model showing undoped AlGaN barrier thickness a) less than the critical thickness with no 2DEG density b) greater than the critical thickness with the formation of 2DEG density at the heterointerface.

### 2.10.2 Al mole fraction (x) in $Al_xGa_{1-x}N$ barrier layer

The Aluminum (Al) mole fraction ($x$) in the $Al_xGa_{1-x}N$ layer has its pronounced effect in the 2DEG density in $Al_xGa_{1-x}N$/GaN heterostructure. Normal Al concentration in the $Al_xGa_{1-x}N$ structure is in between 20% to 30%. Higher Al content in the barrier layer results in a larger energy bandgap than GaN, larger thermal and lattice mismatch, and thus more strain at the interface. This corresponds to larger polarization charge density at the AlGaN surface and $Al_xGa_{1-x}N$/GaN heterointerface and hence the higher 2DEG density.[37] If the Al concentration is too high, it introduces the higher defect

density and degrades the device performance. In general, concentration of Al is controlled to achieve the high 2DEG density without degrading the device. Moreover, if the surface states and the corresponding Fermi level pinning are ignored, higher percentage of Al decreases the affinity of the $Al_xGa_{1-x}N$ barrier layer and thus increases the Schottky barrier height. Higher Al mole fraction in the barrier layer also helps to suppress the 2DEG electron wavefunction penetration into the AlGaN layer by increasing the conduction band discontinuity and thus helps to minimize the electron scattering. Fig. 2.11 shows the polarization induced sheet charge density as a function of Al mole fraction.

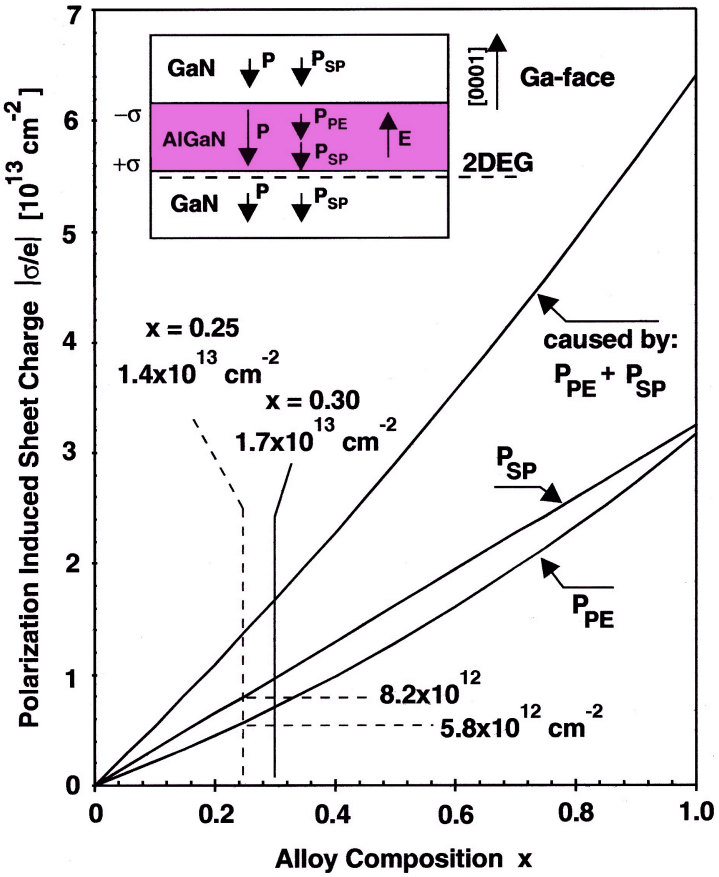


Fig. 2.11 Calculated sheet charge density caused by spontaneous and piezoelectric polarization at the lower interface of a Ga-face GaN/AlGaN/GaN heterostructure vs. alloy composition of the barrier layer. (Reproduced from[38])

## 2.11 Effect of cap layer on AlGaN/GaN heterostructure

A thin cap layer can be incorporated on top of the barrier layer to improve the ohmic contacts by reducing the contact resistance, to reduce the gate leakage by increasing the Schottky barrier height and also to improve the reliability of the devices by partially passivating the surface states.[39,40,41] In general, 2DEG sheet carrier density increases and saturates with the increase in the AlGaN barrier layer thickness, whereas it decreases and saturates with the increasing GaN cap layer thickness. Growing GaN cap layer to the AlGaN/GaN heterostructure introduces additional piezoelectric polarization field on the AlGaN barrier layer, which is oriented in opposite direction to the conventional piezoelectric polarization due to the AlGaN/GaN heterostructure. The additional negative polarization charge at the upper heterointerface increases the electric field at the AlGaN barrier layer and decreases the 2DEG density. With the increase in the GaN cap layer thickness, valence band shifts upwards and ultimately reaches to the Fermi level (Fig 2.13). This forms a 2 dimensional hole-gas (2DHG) density at the upper GaN/AlGaN interface, which hinders further increase in the electric field in the AlGaN layer and saturates the 2DEG density.[42]

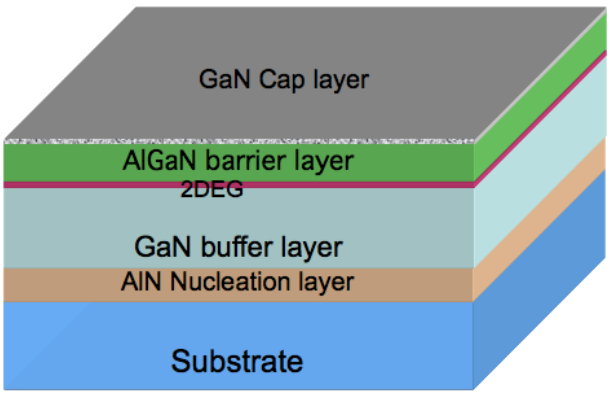


Fig. 2.12 Heterostructure depicting GaN/AlGaN/GaN HFET wafer.

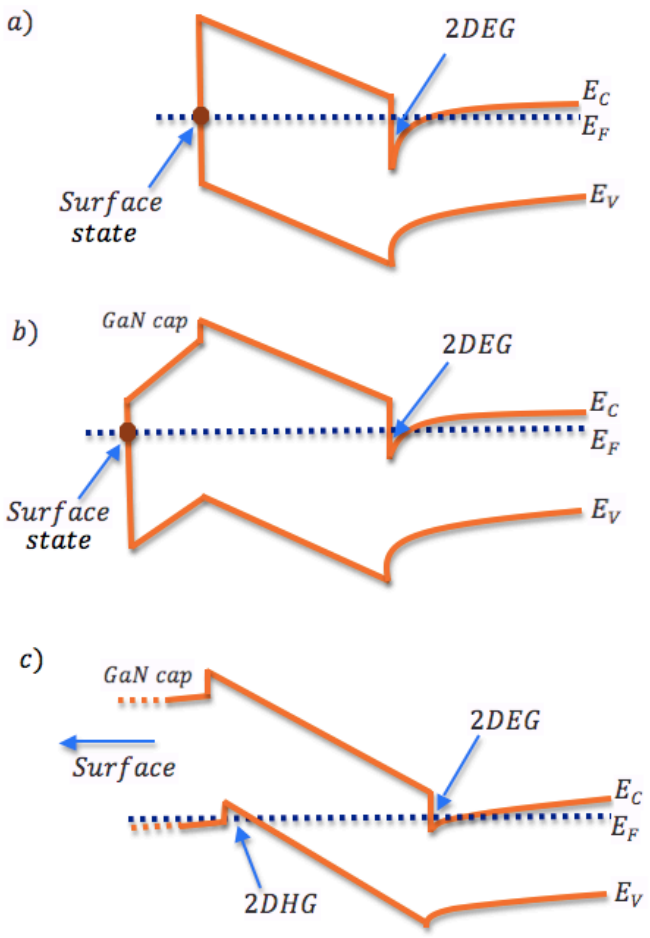


Fig. 2.13 Schematic band diagrams of the AlGaN/GaN heterostructure: a) without the GaN cap layer b) thin GaN cap layer c) thick GaN cap layer.

## 2.12 Contacts on semiconductor

In order to have a useful practical application, a semiconductor needs to make a contact with the outside world. This is achieved by depositing suitable metal on the designated area of the semiconductor. In general, two types of contacts are realized by this metallic deposition, namely: Schottky contact and ohmic contact. Schottky contact is utilized in switching and rectification purpose, whereas low resistance ohmic contact provides the interconnection between the devices and other integrated circuits. A very

simple description of these metal-semiconductor contact is given below.

### 2.12.1 Schottky contact

When a metal is placed in contact with a semiconductor, a potential barrier develops between them that prevents the charge carriers to freely move from one to another. In order to cross the potential barrier, charge carriers must have energy higher than the barrier height known as Schottky barrier height ($\phi_b$). For n-type semiconductor, Schottky barrier height is given by,

$$\phi_b = \phi_m - \chi \qquad [2.27]$$

where $\phi_m$ is the work function of the contact metal and $\chi$ is the electron affinity of the semiconductor. Before the contact, Fermi level in the semiconductor is above that of the metal as shown in the Fig. 2.14(a). As they are brought in contact, electrons from the conduction band in the semiconductor start flowing into the lower energy states into the metal. The charge transfer continues until the chemical potential in the semiconductor reaches in equilibrium with the Fermi energy of the metal, as the Fermi energies of two materials must be equal under thermal equilibrium. This phenomenon bends the band structure and aligns the Fermi level of the two materials. The Schottky model suggests that the barrier height is independent of the semiconductor doping. However, the transport property across the barrier is highly affected by the doping of the semiconductor.[43] Also, the electrons in the conduction band of the semiconductor must overcome the built-in potential barrier to move into the metal. This built-in potential barrier ($V_{bi}$) is given by

$$V_{bi} = \phi_b - \phi_n \qquad [2.28]$$

where $\phi_n$ is the magnitude of the potential difference between the conduction energy band ($E_c$) and Fermi energy level ($E_f$). Reverse biasing increases the semiconductor to metal barrier potential, whereas forward biasing decreases the barrier height facilitating the flow of the electrons across the junction. In both cases, however, the metal to semiconductor barrier height essentially remains the same.

As given above, Schottky barrier height essentially is the function of metal work function and semiconductor electron affinity. Metal with higher work function such as Platinum (5.65 eV), Palladium (5.12 eV), Nickel (5.15 eV) etc. results in higher barrier height. For GaN, platinum is shown to have the highest barrier height of about 1.1 eV [44], whereas titanium tends to give lowest value of about 0.58 eV.[45]

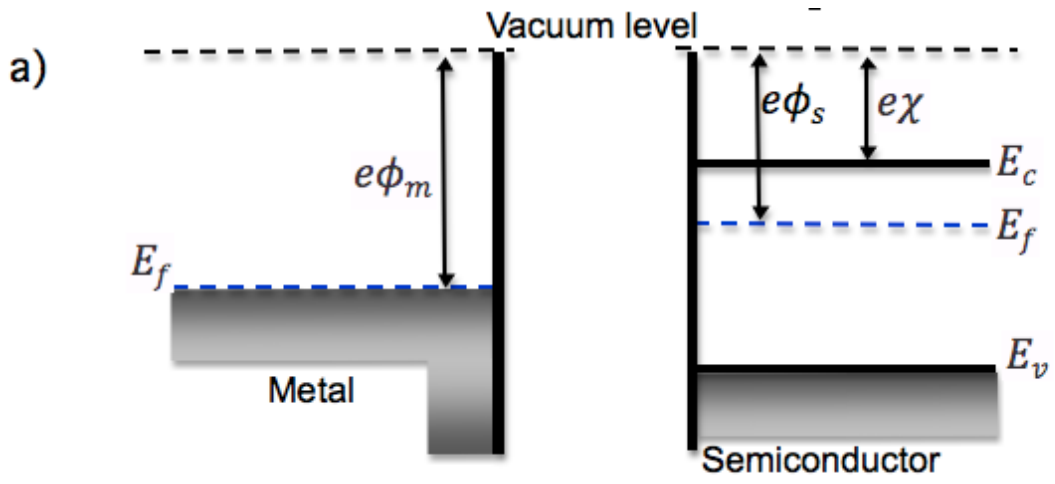

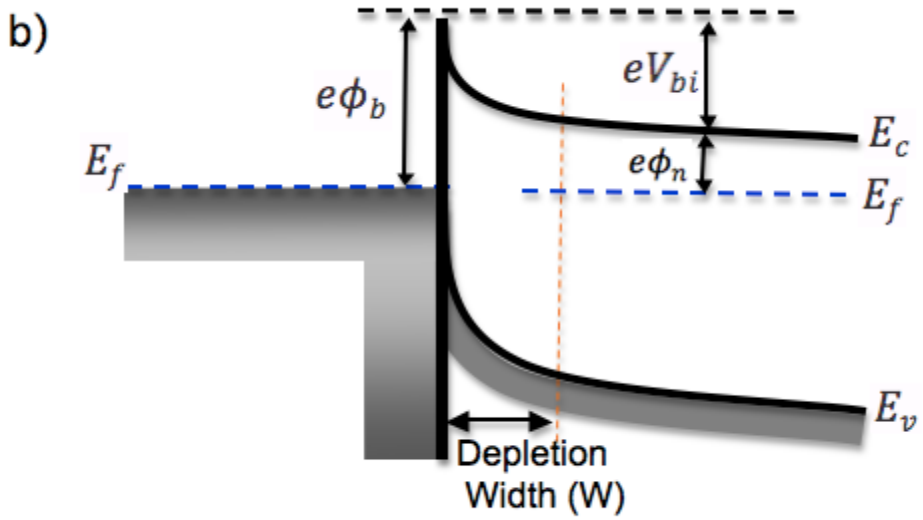


Fig. 2.14 a) Energy band diagram of a metal and n-type semiconductor before contact. b) Ideal energy-band diagram of the metal-semiconductor contact in thermal equilibrium.

### 2.12.2 Ohmic contact

The carrier transport across the Schottky contact primaryly depends upon the Schottky barrier height and depletion width as shown the Fig. 2.14(b). If these parameters are reduced significantly, the contact becomes ohmic. If the Schottky barrier height across the metal semiconductor junction is zero or negative, the carriers can move across the metal semiconductor junction, in or out, with a minimal resistance. This type of contact is called an ohmic contact. Barrier height is the property of the material and can be lowered with the suitable choice. Thermal annealing is frequently performed to alloy the metal into the semiconductor, which can also lower the barrier height. In addition, thinner barrier width increases the tunneling probability to facilitate the carrier transport.

In ohmic contact, contact resistance plays a key role in the device characteristics

such as knee voltage, maximum drain current, transconductance, maximum cutoff and oscillation frequency. In order to improve the performance of the device, the contact resistance of the ohmic contact must be minimized. Also, lower surface roughness, higher edge acuity, higher thermal stability, etc. are also desirable for the operation of the sub-micron devices in the high temperature and high voltage application.

In AlGaN/GaN HFET transistor, Ti/Al based metallization scheme is widely used as an ohmic contact metal.[46] When the Ti/AlGaN structure is annealed at high temperature (~850 ℃), titanium nitride (TiN) will be formed at the interface creating nitrogen vacancies in the AlGaN layer.[47,48] These nitrogen vacancies are known to act as n-type doping, facilitating the electron transport mechanism. In addition to improving adhesion of metal to semiconductor, the contact resistance is significantly lowered with the alloying of the metal into the semiconductor.

**References**


[1] Y. Borodovsky, "Marching to the beat of Moore's law", Proc. of SPIE **6153**, 23 (2006).

[2] J. Tang, G. Niu, Z. Jin, J. D. Cressler, S. Zhang, A. J. Joseph, and D. L. Harame, "Modeling and characterization of SiGe HBT low-frequency noise figures-of-merit for RFIC applications," IEEE Trans. Microw. Theory Tech. **50**, 2467 (2002).

[3] D Bhattacharaya, "Gallium arsenide digital integrated circuits", Bull. Mater. Sci. **13**, 135 (1990).

[4] M. Levinshtein, S. Rumyantsev and M. Shur, "Properties of advanced semiconductor materials," United Kingdom: John Wiley & Sons, (2001).

[5] H.-S. P. Wong, "Beyond the conventional transistor", IBM J. Res. & Dev. 46, **133** (2002).

[6] R. W. Keyes, "Figure of merit for semiconductors for high speed switches," Proc. IEEE, **60**, 225 (1972).

[7]B. J. Baliga, "Semiconductors for high-voltage, vertical channel field-effect transistors," J. Appl. Phys. **53**, 1759 (1982).

[8] B. J. Baliga, "Power semiconductor device figure of merit for high – frequency applications," IEEE Electron Device Lett. **10**, 455 (1989).

[9] S. J. Pearton, F. Ren, A. P. Zhang and K. P. Lee, "Fabrication and performance of GaN devices", Mater. Sci. Engi. R **30,** 55 (2000).

[10] R.J. Trew, “High-frequency solid-state electronic devices”, IEEE Trans. Electron Device **52**, 638 (2005).

[11] G Aroshvili, "GaN HEMT and MMIC design and evaluation," Masters Thesis, University of Gavle, (2008).

[12] A. F. M. Anwar, S. Wu, and R. T. Webster, ``Temperature dependent transport properties in GaN, AlGaN, and InGaN semiconductors," IEEE Trans. Electron Device **48**, 567 (2001).

[13] G. Steinhoff, O. Purrucker, M. Tanaka, M. Stutzmann, and M. Eickhoff, “$Al_xGa_{1-x}N$ -A new material system for biosensors”, Adv. Funct. Mater. **13**, 841 (2003).

[14] U. K. Mishra , P. Parikh and Y.-F. Wu "AlGaN/GaN HEMTs—An overview of device operations and applications", Proc. IEEE **90**, 1022 (2002).

[15] H. Schulz, K. H. Thiemann, “Crystal structure of AlN and GaN”, Solid State Comm. **23**, 815 (1977).

[16] H. Morkoç, “Handbook of nitride semiconductors and devices”, Wiley, New York, Vol. 1 (2008).

[17] P. E. Van Camp, V. E. Van Doren, J. T. Devreese, “High pressure structural phase transformation in gallium nitride”, Soild State Comm. **81**, 23 (1992).

[18] V. Rawat, D. N. Zakharov, E. A. Stach, and T. D. Sands, "Pseudomorphic stabilization of rocksalt GaN in TiN/GaN multilayers and superlattices", Phys. Rev. B **80**, 024114 (2009).

[19] M. E. Levinshtein, S. L. Rumyantsev and M. S. Shur, "Properties of advanced semiconductor materials", New York, John Wiley & Sons, (2001).

[20] O. Ambacher, B. Foutz, J. Smart, J. R. Shealy, N. G. Weimann, K. Chu, M. Murphy, A. J. Sierakowski, W. J. Schaff, L. F. Eastman, R. Dimitrov, A. Mitchell, and M. Stutzmann "Two dimensional electron gases induced by spontaneous and piezoelectric polarization in undoped and doped AlGaN/GaN heterostructures" J. Appl. Phys. **85**, 3222 (1999).

[21] Bernardini F, Fiorentini V and Vanderbilt D, "Spontaneous polarization and piezoelectric constants of III-V nitrides", Phys. Rev. B **56** R10 024 (1997).

[22] O. Ambacher, "Growth and applications of Group III-nitrides", J. Phys. D: Appl. Phys. 31, 2653 (1998).

[23] E. T. Yu, J. O. McCaldin, and T. C. McGill, "Band offsets in semiconductor heterojunctions," Solid State Phys. **46**, 1 (1992).

[24] M. A. Khan, G. Simin, S. G. Pytel, A. Monti, E. Santi and J. L. Hudgins, "New developments in gallium nitride and the impact on power electronics", on Proc. of IEEE Power Electronics Specialist Conference (2005).

[25] F. Bernardini, V. Fiorentini, and D. Vanderbilt, "Spontaneous polarization and piezoelectric constants of III-V nitrides", Phys. Rev. B **56**, R10024 (1997).

[26] K. Tsubouchi, K. Sugai, and N. Mikoshiba, "AlN material constants evaluation and SAW properties on $AlN/Al_2O_3$ and AlN/Si", IEEE Ultrason. Symp. **1**, 375 (1981).

[27] A. F. Wright, "Elastic properties of zinc-blende and wurtzite AlN, GaN, and InN", J. Appl. Phys. **82**, 2833 (1997).

[28] Y. Takagi, M. Ahart, T. Azuhato, T. Sota, K. Suzuki, and S. Nakamura, "Brillouin scattering study in the GaN epitaxial layer", Physica B **219 & 220,** 547 (1996).

[29] E. T. Yu, X. Z. Dang, P. M. Asbeck, S. S. Lau and G. J. Sullivan, "Spontaneous and piezoelectric polarization effects in III-V nitride heterostructures.," J. Vac. Sci. Technol. B **17**, 4 (1999).

[30] O. Ambacher, B. Foutz, J. Smart, J. R. Shealy, N. G. Weimann, K. Chu, M. Murphy, A. J. Sierakowski, W. J. Schaff, L. F. Eastman, R. Dimitrov, A. Mitchell, and M. Stutzmann "Two dimensional electron gases induced by spontaneous and piezoelectric polarization in undoped and doped AlGaN/GaN heterostructures" J. Appl. Phys. **85**, 3222 (1999).

[31] J. P. Lbbeston, P. T. Fini, K. D. Ness, S. P. DenBaars, J. S. Speck, and U. K. Mishra, "Polarization effects, surface states, and the source of electrons in AlGaN/GaN heterostructure field effect transistors", Appl. Phys. Lett. **77**, 250 (2000).

[32] E. T. Yu, G. J. Sullivan, P. M. Asbeck, C. D. Wang, D. Qiao, and S. S. Lau

"Measurement of piezoelectrically induced charge in GaN/AlGaN heterostructure field-effect transistors", Appl. Phys. Lett. **71**, 2794 (1997).

[33] M. S. Shur, "GaN and related materials for high power applications", Mater. Res. Soc. Symp. Proc. **483**, 15 (1998).

[34] G. Martin, A. Botchkarev, A. Rockett, and H. Morkoc, "Valence-band discontinuities of wurtzite GaN, AlN, and InN heterojunctions measured by x-ray photoemission spectroscopy", Appl. Phys. Lett. **68**, 2541 (1996).

[35] D. Brunner, H. Angerer, E. Bustarret, R. Hopler, R. Dimitrov, O. Ambacher, and M. Stutzmann, Optical constants of epitaxial AlGaN films and their temperature dependence", J. Appl. Phys. **82**, 5090 (1997).

[36] J. P. Lbbeston, P. T. Fini, K. D. Ness, S. P. DenBaars, J. S. Speck, and U. K. Mishra, "Polarization effects, surface states, and the source of electrons in AlGaN/GaN heterostructure field effect transistors", Appl. Phys. Lett. **77**, 250 (2000).

[37] E. T. Yu and M. O. Manasreh, "III-V nitride semiconductors: Applications & devices" (Optoelectronic Properties of Semiconductors and Superlattices, V 16) New York : Taylor & Francis, (2003).

[38] O. Ambacher, J. Smart, J. R. Shealy, N. G. Weimann, K. Chu, M. Murphy, W. J. Schaff, L. F. Eastman, R. Dimitrov, L. Wittmer et al. "Two-dimensional electron gases induced by spontaneous and piezoelectric polarization charges in N- and Ga-face AlGaN/GaN heterostructure", J. Appl. Phys. **85**, 3222 (1999).

[39] Th. Gessmann, J. W. Graff, Y.-L. Li, E. L. Waldron, and E. F. Schubert, "Ohmic contact technology in III nitrides using polarization effects of cap layers", J. Appl. Phys. **92**, 3740 (2002).

[40] E. T. Yu, X. Z. Dang, L. S. Yu, D. Qiao, P. M. Asbeck, S. S. Lau, G. J. Sullivan, K. S. Boutros, and J. M. Redwing, "Schottky barrier engineering in III–V nitrides via the piezoelectric effect", Appl. Phys. Lett. **73**, 1880 (1998).

[41] S. L. Selvaraj, T. Ito, Y. Terada, and T. Egawa, "AlN/AlGaN/GaN metal-insulator-semiconductor high-electron-mobility transistor on 4 in. silicon substrate for high breakdown characteristics", Appl. Phys. Lett. **90**, 173506 (2007).

[42] Sten Heikman, Stacia Keller, Yuan Wu, James S. Speck, Steven P. DenBaars, and Umesh K. Mishra, "Polarization effects in AlGaN/GaN and GaN/AlGaN/GaN heterostructures", J. Appl. Phys. **93**, 10114 (2003).

[43] M. Shur, "Physics of semiconductor devices", Prentice Hall, Englewood Cliffs, 207 (1990).

[44] S. N. Mohammad, Z. Fan, W. Kim, O. Aktas, A. Botchkarev, A. Salvador, and H. Morkoc, "Near ideal platinum-GaN Schottky diodes", Electron. Lett. **32**, 598 (1996).

[45] Binari, S.C. Dietrich, H.B. Kelner, G. Rowland, L.B. Doverspike, K. Gaskill, D.K. "Electrical characterization of Ti Schottky barriers can n-type GaN" Electron. Lett. **30**, 909 (1994).

[46] F. M. Mohammed, L. Wang, I. Adesida, and E. Piner, "The role of barrier layer on Ohmic performance of Ti/Al-based contact metallizations on AlGaN/GaN heterostructures", J. Appl. Phys. **100**, 023708 (2006).

[47] A. N. Bright, P. J. Thomas, M. Weyland, D. M. Tricker, C. J. Humphreys, and R. Davies, "Correlation of contact resistance with microstructure for Au/Ni/Al/Ti/AlGaN/GaN ohmic contacts using transmission electron microscopy", J. Appl. Phys. **89**, 3143 (2001).

[48] R. C. Glass, L. M. Spellman, and R. F. Davis, "Low energy ion-assisted deposition of titanium nitride ohmic contacts on alpha (6H)-silicon carbide", Appl. Phys. Lett. **59**, 2868 (1991).

# Chapter 3

## Semiconductor processing techniques

### 3.1 Introduction

This chapter describes semiconductor processing techniques and equipment used for fabrication of AlGaN/GaN heterojunction field effect transistors. Theoretical description along with detailed experimental procedures and recipes of the fabrication employed in this dissertation are explained. Processing techniques include sample cleaning, lithography, mesa isolation, metallization, annealing, and device packaging, and are described below.

### 3.2 Surface contaminants

Semiconductor wafer surface can easily get contaminated during the storage and device fabrication process. Contaminations generally originate from the ambient air, processing materials (chemicals, gases, water, etc.), manufacturing tools and personnel operating them in a clean room. These contaminants can easily get adsorbed into the wafer surface, lie onto the electrically sensitive area and can cause the catastrophic failure of the device. The most common contaminants encountered during the device fabrication are discussed below.

#### 3.2.1 Particles

Particles are the major source of contaminants encountered during the processing of the semiconductor devices. As the feature size of semiconductor devices continues to shrink, size of the contaminant particle becomes more and more important. The particle size distribution in the ambient air lies in the range of 1 nm to 10 μm and peaks at around 5 μm and 0.1 μm.[1] In general, tolerable surface adsorbed particle size needs to be at least 10 times smaller than the minimum feature size of the device.[2] If these contaminants are present in the less sensitive area of the devices, their effect will be less critical.

### 3.2.2 Metallic ions

Presence of electrically active metallic contaminants in the semiconductor wafer can alter the electrical characteristics of the device and degrade the performance and reliability of the devices. These contaminants primarily originate from the liquid chemicals, water as well as handling and processing tools. Among all the metallic contaminants, most common contaminants are iron (Fe), copper (Cu), aluminum (Al) along with the ionic metals like sodium (Na) and calcium (Ca).

### 3.2.3 Chemicals

Chemical processing can contaminate the wafer leading to the unwanted effect such as etching from the undesired area, creating compounds that become hard to remove from the surface, etc. Among others, chorine (Cl) is the major chemical contaminants.

### 3.2.4 Organic contaminants

Organic compounds in volatile form are present in ambient air as well as in clean room air in large amounts. They can adsorb to the semiconductor surface very easily.

Photoresists during the device processing and organisms like bacteria can also contribute as particulate contaminants and degrade the device performance.

### 3.2.5 Oxides/ moisture

Native oxides can grow very easily on the exposed surfaces of most of the semiconductor wafers and can affect the metallic contacts & other electrical/optical properties. Moisture from ambient and residue from the wet processes can alter the surface properties and are also considered as a contaminants. They can shift the electrical parameters and makes the reproducibility of the manufacturing process difficult.

## 3.3 GaN/AlGaN/GaN HEMT wafer

For the experiment, we have used the HEMT (high electron mobility transistor) wafer with GaN/AlGaN/GaN heterostructure grown on Si (111) substrate. The HEMT wafer was grown at SVT Associates, Inc. and the structure consisted of 0.3 μm thick resistive AlN buffer layer, 1.2 μm thick resistive GaN layer, 20 nm thick $Al_{0.25}Ga_{0.75}N$ layer, and 2 nm thick GaN cap layer.

### 3.3.1 Cleaning

Since the wafer surface can easily get contaminated with the various contaminants discussed above, an effective and convenient cleaning method is very important to ensure the proper device functionality. Entire cleaning process of the fabrication was done inside a fume hood, which is shown in Fig 3.1. The wafer was first diced into $5mm \times 5mm$ square pieces and ultrasonically cleaned in the organic solvents in the following order: acetone, trichloroethylene (TCE), acetone, methanol, and methanol. The cleaning was

done for the time of 5 minutes in each solvent. The first acetone and TCE was used to complete degrease the organic contaminants from the wafer surface. Second acetone served as a solvent to dissolve the TCE. First methanol was solvent for the acetone, whereas second fresh methanol served to further cleaning the sample. Since the methanol is dissolvable in water, the sample was then rinsed in DI water to remove the residues of the solvents. In addition to the organic contaminants, the sample needs further cleaning for ionic contaminants and native oxides. For this, the sample is placed in a mixture of Hydrochloric acid (HCl) and DI water in a 1:1 ratio and heated at 110℃ for 10 minutes. This acid cleaning procedure is found to be effective and also gives the smaller C/N (carbon/nitrogen) ratio.[3] In addition, it increases Cl (chlorine) concentration on the surface and reduces the oxygen coverage on the surface.[4] Cl surface termination might be beneficial since it promotes adhesion of metals like Ni, Au, Pd, Pt on GaN surface and hinders re-oxidation of the surface.[5,6] Finally, the sample is thoroughly rinsed in the DI water, blow dry with nitrogen and examined with optical microscope for the cleanliness.

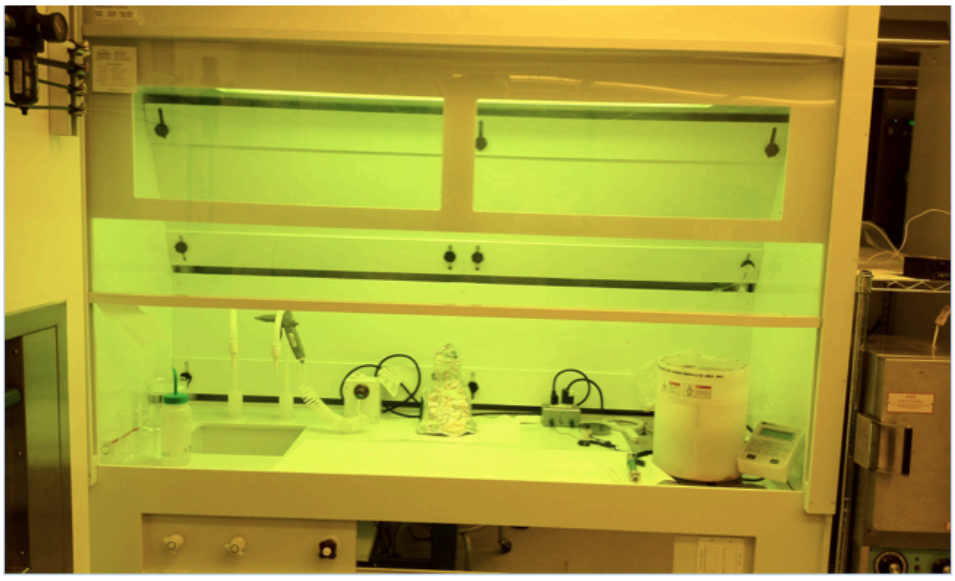

Fig. 3.1 Sample cleaning fume hood.

## 3.4 Device fabrication

The fabrication of integrated circuit requires various chemical and physical processes including litho patterning, thin film deposition, etching, etc. Lithography is fundamental to all of these processes, which forms 3 dimensional relief images of the pattern on the polymer for the subsequent transfer of the pattern on the wafer. The technologies involved in the fabrication process are discussed below.

### 3.4.1 Photolithography

Photolithography is an optical process that involves exposure tool, mask, resist and multiple processing steps to accomplish pattern transfer from a mask to resist, and then to substrate. The important parameter of the lithography is the spatial resolution of the system, which defines the minimum feature size. The minimum feature size depends on the optical elements, radiation wavelength as well as in the resist used. To achieve the higher resolution, exposure radiation needs to have shorter wavelength. In general, there are three modes used in optical lithography namely; contact, projection and proximity mode. The optical resolution of each method depends on the minimum feature size it can produce. In contact lithography as sketched in Fig. 3.2 (a), the mask is in contact with the photoresist with an unchanged magnification and yields a moderate resolution of about 1 μm or better. However, mask damage due to the residues of photoresists, scratching, imaging of the undesirable particles, etc. are the main disadvantage of this mode. There are two approaches in the contact mode: soft contact and hard contact. The distinction between them lies in the fact that a soft contact uses lesser pressure to keep the mask and photoresist in contact as compared to that of the hard contact.

As shown in Fig. 3.2 (b), the proximity mode consists of photo mask and resist,

which are separated by some gap. This mode gives the similar magnification but slightly smaller resolution than in the contact mode due to a phenomenon called diffraction of the light. In projection mode as in Fig. 3.2 (c), mask is placed at a certain distance from the resist with the optical system in between the resist and mask. This mode gives the demagnification of the mask image and also higher resolution. However, this method requires the expensive equipment and complicated set up.

The minimum feature size (MFS) is associated with the diffraction effect, and is typically in the order of wavelength of the radiation used in exposure. The resolution of the optical lithography system scales with wavelength and numerical aperture ($NA$) according to the modified Rayleigh criterion as[7]

$$Resolution = k_1 \frac{\lambda}{NA} \quad [3.1]$$

$$Depth\ of\ focus = k_2 \frac{\lambda}{(NA)^2} \quad [3.2]$$

where process constants $k_1$ and $k_2$ are measures of difficulty in printing a given dimension with the given resist-exposure system combination, $\lambda$ is the wavelength of the radiation used to carry out the imaging, $NA$ is the numerical aperture of the imaging system. The above equations [3.1] & [3.2] shows that decreasing the wavelength and increasing the numerical aperture can obtain better resolution. The tradeoff however is that the depth of focus gets decreased. The wavelength of the light (radiation), or charged particles used in the lithography system has progressed from the blue wavelengths (436 nm) to UV (365 nm) to deep-UV (248 nm) to today's extreme UV (10-14) nm radiations. As visible light is far less expensive to produce, manipulate and propagate as compared

to the electromagnetic radiation and x-rays, cost and ease of production are the probable tradeoff.

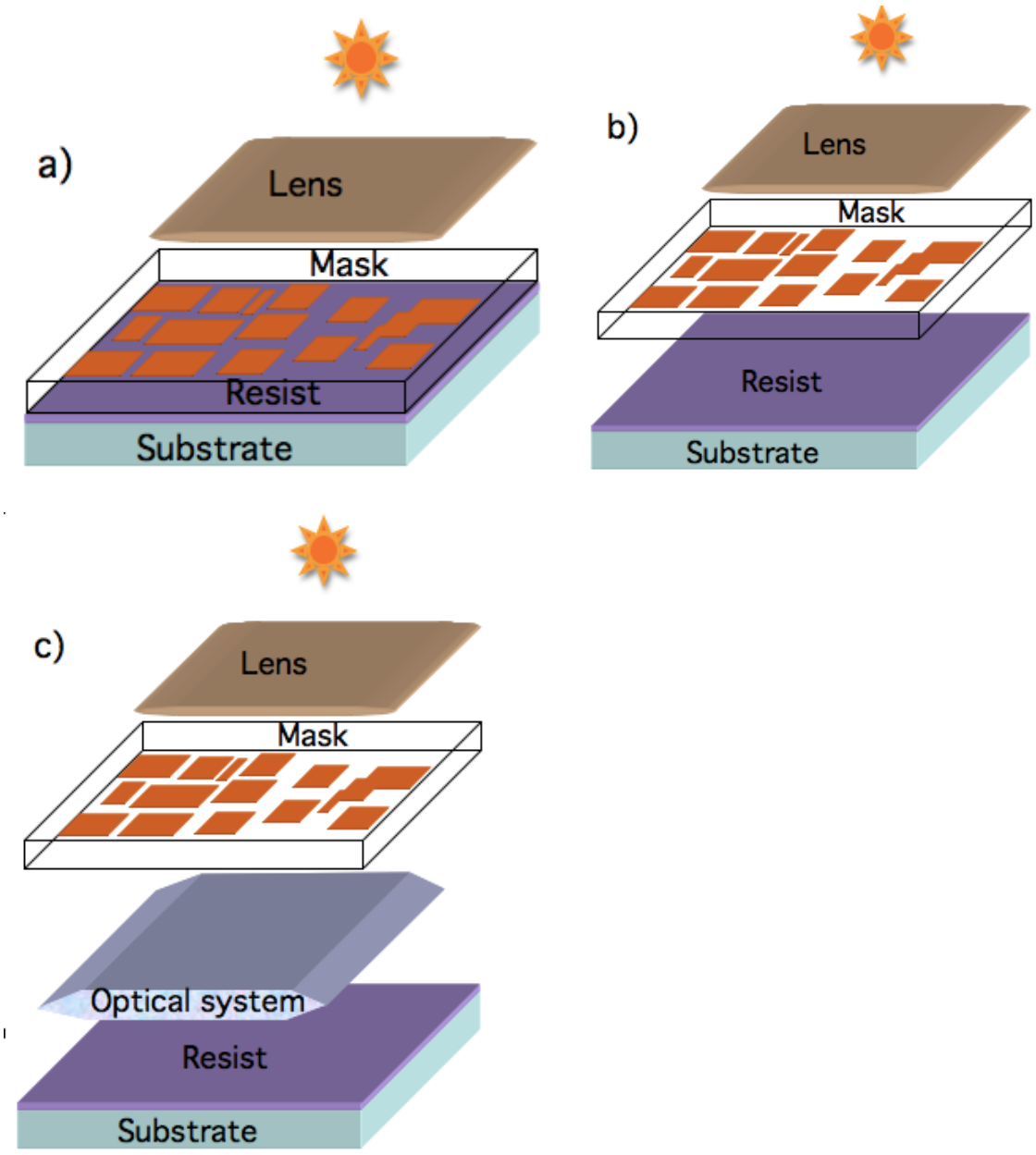


Figure 3.2 Schematic illustrations of various illumination methods for an optical lithography: a) contact mode b) proximity mode and c) projection mode.

During all the fabrication process in this thesis, image reversal photoresist, AZ® 5214-E, which is capable of both positive and negative tone mode, in image reversal mode has been used. The first step of the photolithography process begins with the dispensing a controlled volume of radiation sensitive polymer called as photoresist on the center of the cleaned wafer. Spin coating produces a photoresist film of uniform thickness across the sample and this thickness depends on the various factors, such as speed of the spinner, viscosity of the resist, humidity, substrate, substrate topography, etc. is given by[8]

$$Thickness = k\frac{p^2}{\omega^{1/2}} \qquad [3.3]$$

where $k$ is the spinner constant, $p$ is the resist solid content in percentage and $\omega$ is the rotational speed of the spinner in RPM/1000. The sample with resist on it is then spin coated at 4000 RPM (rotation per minute) for 30 seconds and subsequently soft backed at 110 ℃ for 60 seconds. This step helps to drive off the solvents from the resist and promotes adhesion of the resist on the substrate. Further, soft bake makes resist less viscous thus becomes less susceptible to the particulate contamination. The average thickness of the resist after this coating was approximately 1.4 μm.

In the next step of the lithography process, the sample with resist on it is aligned and exposed to the radiation of mercury (Hg) arc lamp at an power of ~ 160 watt (measured at 400 nm) for 30 seconds. Alignment and exposure tool in use is Karl Suss MJB3 photo-mask aligner as shown in Fig. 3.3. Clear field mask with the soft contact illumination mode is adopted in all of the fabrication process (dark field mask = opaque background and clear images; clear field mask = clear background and opaque images).

After exposure, the sample is hard baked at 110 ℃ for 60 seconds for the image

reversal to take place. This is the most critical step of the image reversal process. After this step, exposed area of the photoresist crosslinks and becomes insoluble in developer whereas unexposed area remains photoactive.

The sample is next flood exposed (no mask) for 60 seconds. This step makes the previously unexposed area of the photoresist soluble in the developer solution. Next, sample is developed in a 1:3 diluted solution of AZ 400K and DI water. The overall result gives the negative image of the mask pattern with the desired undercut as shown in the Fig. 3.4. The key advantage of using image reversal process is that the slope of the photoresist can be controlled for better resolution and easier lift-off.

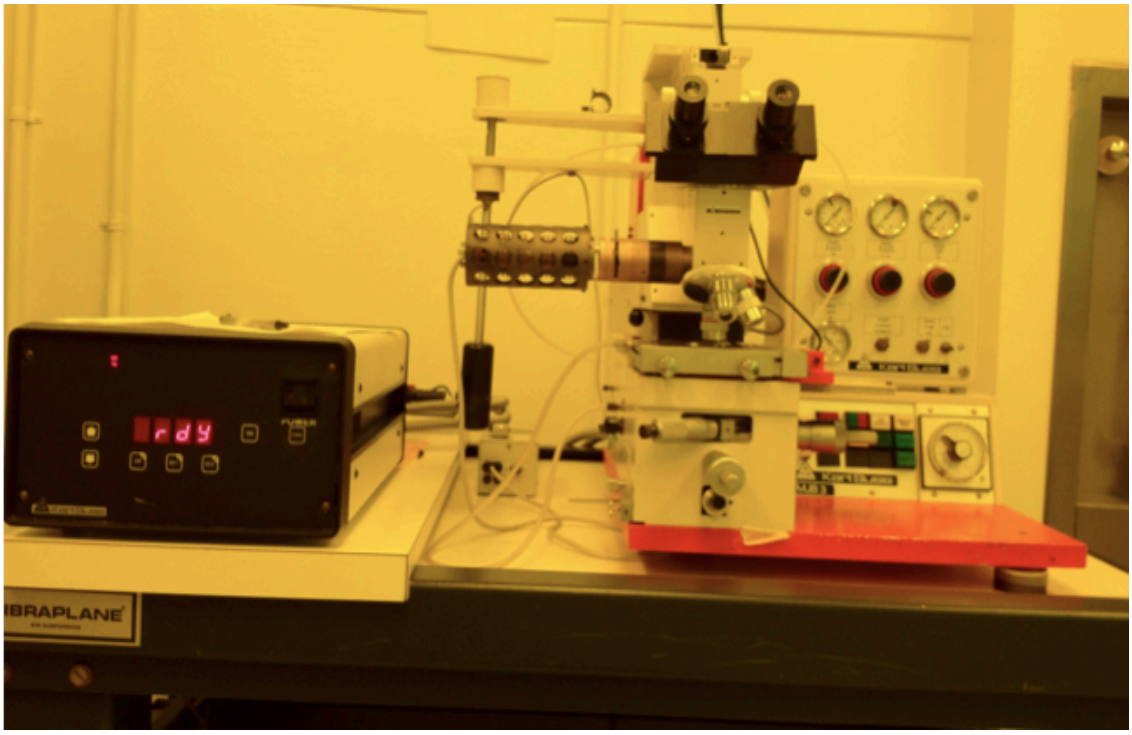


Fig. 3.3 Karl Suss MJB3 photomask aligner.

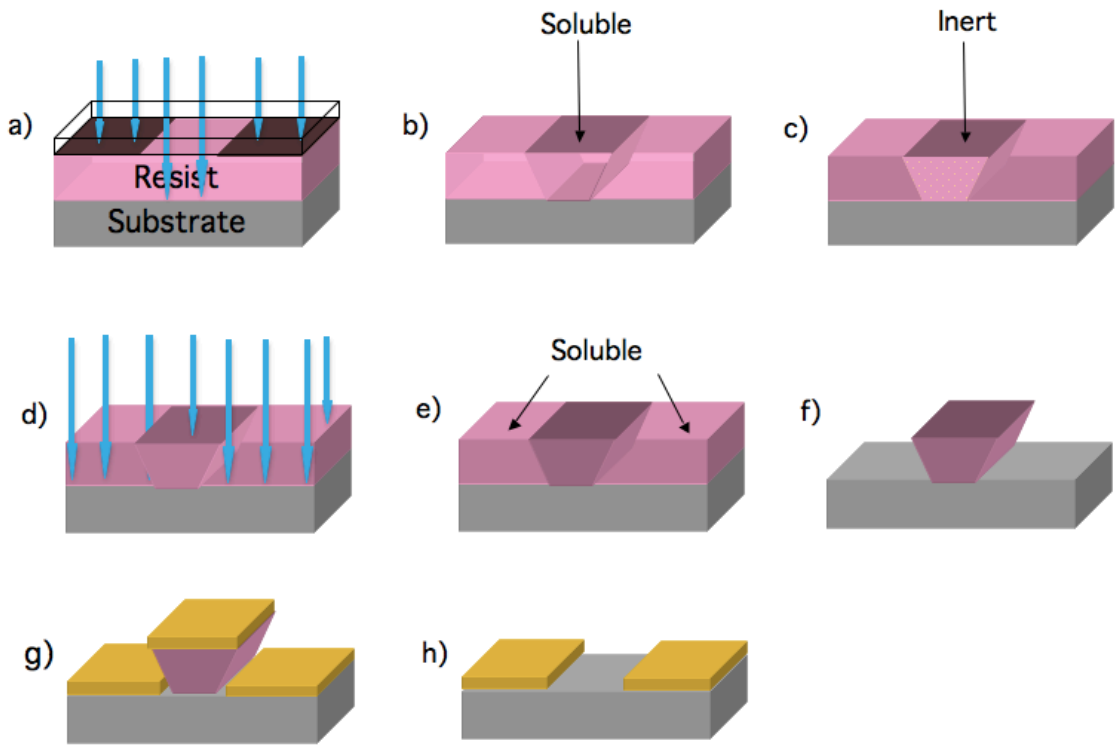


Figure 3.4 Illustration of the image reversal lithography process: a) aligned and exposed to the radiation b) soluble exposed portion after the exposure c) inert exposed portion of the resist after hard backed d) flood exposure without the mask e) resist not exposed to radiation at first place gets soluble f) after development, the area exposed at first place remains g) sputtering deposition of the metals h) lift-off.

### 3.4.2 Plasma processing

Plasma process in semiconductor processing generally involves the surface modification by depositing or removing the materials. The low-pressure plasma discharge comprises of highly energetic free electrons in "cold" state.[9] The low-temperature plasma comprises of atoms, molecules and radicals with highly excited electrons. The sufficiently high energy overcomes the molecular bonding of the process gas, sustaining the plasma process at relatively lower temperature, which would otherwise require the higher temperature. The following plasma processes are used in the etching and depositing process.

#### 3.4.2.1 Metal deposition: magnetron sputtering

Sputtering is a physical vapor deposition process used to deposit film of atoms from the source material (target) onto the substrate. In the sputtering process, sputtering chamber is filled with noble gas, such as argon (Ar). A negative potential of few hundred volt is supplied to the target. Positively charged ions of the noble gas are attracted and accelerated towards the target. In the process, the impinging ions transfer their momentum to the surface atoms of the target. If the momentum in both direction and their magnitude is greater than the surface binding energy, a target atom will get ejected or sputtered. The sputtered atoms leave the surface with several eV in energy, which are much higher compared to the evaporated atoms, which have energy around 0.1 eV. This high energy helps to form a dense film on the substrate in the thin film growth process. Further, sputtering offers better process control such as film thickness, and film properties such as grain size and step coverage as compared to the evaporation.

In the DC magnetron sputtering system, a permanent magnet is placed beneath the target in such a way that its magnetic field projects parallel to the target surface. As the direction of applied electric field is perpendicular target surface, the $\boldsymbol{E}\times\boldsymbol{B}$ field establishes a closed and continuous field path for the electrons. Thus the plasma density is highest within the maximum $\boldsymbol{E}\times\boldsymbol{B}$ field resulting a higher sputtering rate.

The power source to the sputtering system may be DC or RF. DC source can be built to supply higher power as compared to the RF source giving higher deposition rate. However, DC source is used for the sputtering of conducting target, whereas RF source makes the sputtering of the dielectric material possible.

Thin film deposition described in this work is done by the DC (direct current)

magnetron sputtering system as shown in Fig. 3.5. The vacuum chamber consists of four sputtering guns, which is equipped with chimneys to facilitate the deposition and prevent the cross-contamination. Samples are mounted on the top rotational plate, which is about 15 cm from the target. After the chamber is pumped down to a sufficiently low base pressure of about $10^{-8}$ torr to remove the contaminants, argon gas is introduced into it at the rate of 100 sccm for 5 minutes to fill the chamber. After the argon pressure inside the chamber gets stable at 15 millitorr, DC voltage is applied between the target (cathode) and the substrate (anode) to start the plasma process and the deposition. Chilled water lines are maintained beneath the targets to cool them down during the sputtering process. A short pre-sputtering event removes the trapped impurities from the target surface. This follows the deposition of metal thin films on the photo-patterned sample as shown in Fig. 3.4 (g).


Fig. 3.5 DC Magnetron sputtering system for the deposition of the metallic thin film.

### 3.4.2.2 Reactive ion etching

Except for the particular crystallographic direction, etching of the GaN based material becomes quite challenging by conventional wet etch approach.[10] To overcome this problem, dry etching has become a preferred device patterning and isolation technique in processing GaN and other compound semiconductor material. Because of the low chemical reactivity and high bond strength (8.92 eV/atom) of GaN, device isolation and thus the etching is exclusively done by dry etching techniques. Reactive Ion Etching (RIE) makes use of both physical and chemical components of etch mechanisms to obtain the dimensional profile and fast etch rate. In RIE chamber, plasmas are generated between two electrodes with the application of RF electromagnetic field at an excitation frequency of 13.65 MHz. Samples are placed on the lower electrode on which lighter electron species from the plasma easily gets adsorbed polarizing it negatively. The build up electric field accelerates the positive ions in the plasma toward the sample and enhances the highly anisotropic etching process. Fig. 3.6 shows the custom made RIE system used in this dissertation. This system consists of RF power supply (Advanced Energy's RFX-600), an impedance matching unit (Advanced Energy's ATX-600), and cylindrical vacuum chamber with a wafer platter, which is positioned at the bottom of the chamber. This wafer platter is electrically isolated from the rest of the chamber. Gas is fed through the mass flow controller in the chamber and exhausted through the vacuum pump outlet. At the beginning, chamber is pumped down to a pressure level of about 10 mTorr. A fluorine containing gas, in particular, $NF_3$ is introduced in the chamber with a flow rate of 9 sccm. After the pressure inside the chamber gets stable at around 35 mTorr, RF power is turned on to initiate the plasma. Forward power is set to about 21 watt and

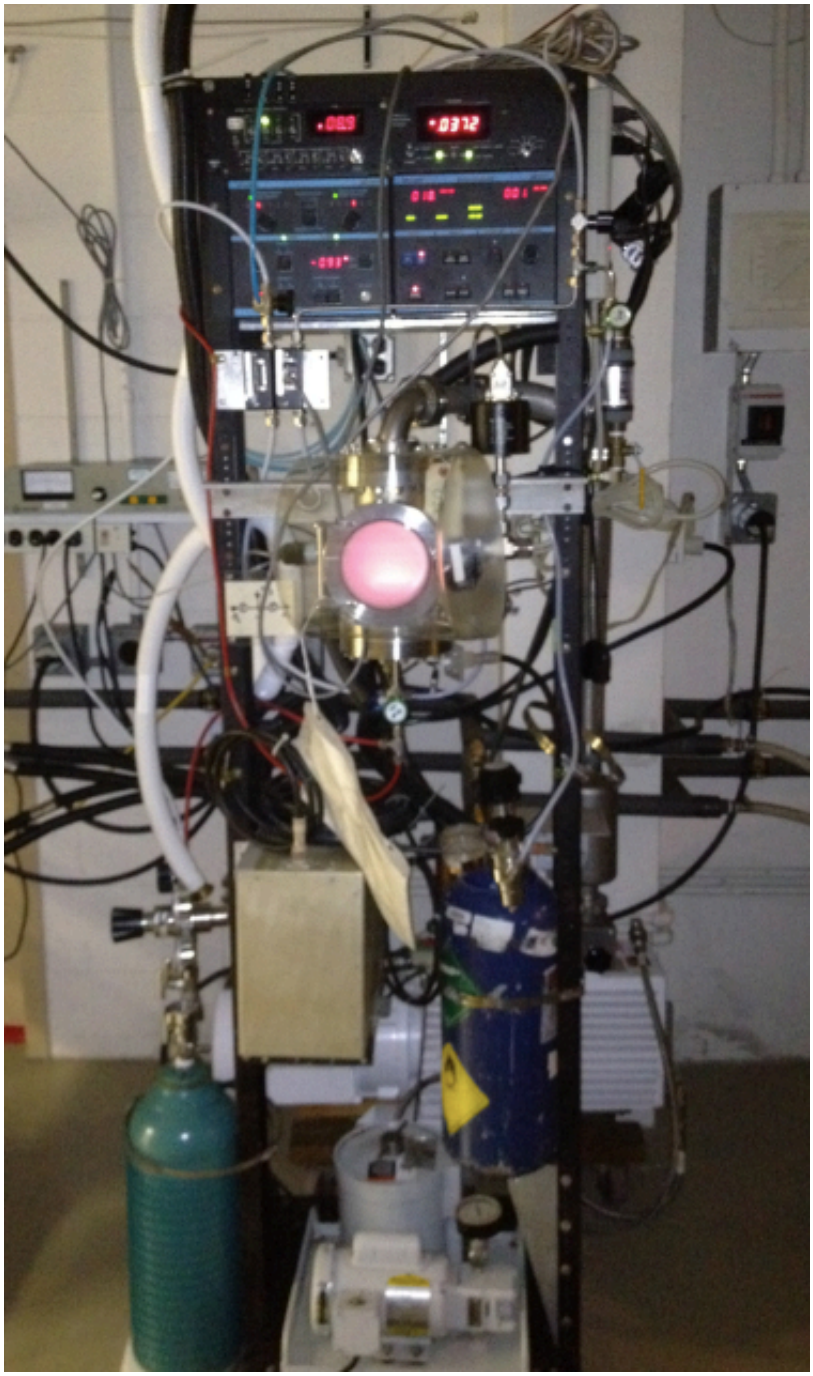

Fig. 3.6 Photograph of the reactive ion etching system.

the reflected power is set to a minimum value with the help of impedance matching unit. During the etching process, voltage difference of about -120 V builds up between the electrodes. The amount of the DC bias that develops within a process system depends on the system design and other process variables. DC bias refers to the DC component of the RF power that is developed between the cathode and anode of the RF plasma vacuum chamber. This DC component is blocked from the RF generator by the capacitors that are employed in the impedance-matching networks. The DC bias is a controllable parameter, which indicates the change in response to the change in process parameters such as molecular densities & ratios of the process gases, cathode/anode surface area ratios, RF power densities, pressure level & stability, etc. Molybdenum/Nickel was used as a protective mask material and hydrogen peroxide ($H_2O_2$) was used to etch off the Molybdenum after the etching process. $NF_3$ based plasma was chosen in order to have a planer process. The reactive component of the gas is fluorine and nitrogen is the carrying component. The fluorine implantation into the AlGaN and GaN layer can deplete the 2DEG density at the heterointerface and provide the active device isolation. The device isolation achieved by this method is comparable to that obtained by using $Cl_2$ plasma.[11] In addition to the ion implantation, some of the energetic ion physically sputter the atom from the sample surface and the etch rate during the process was 3.3 $nm$ per minute.

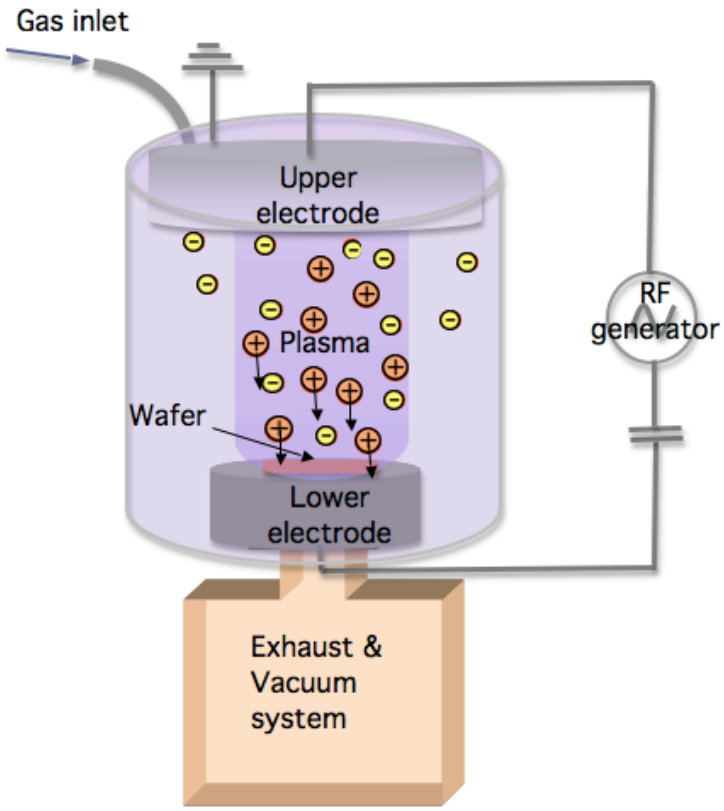


a)

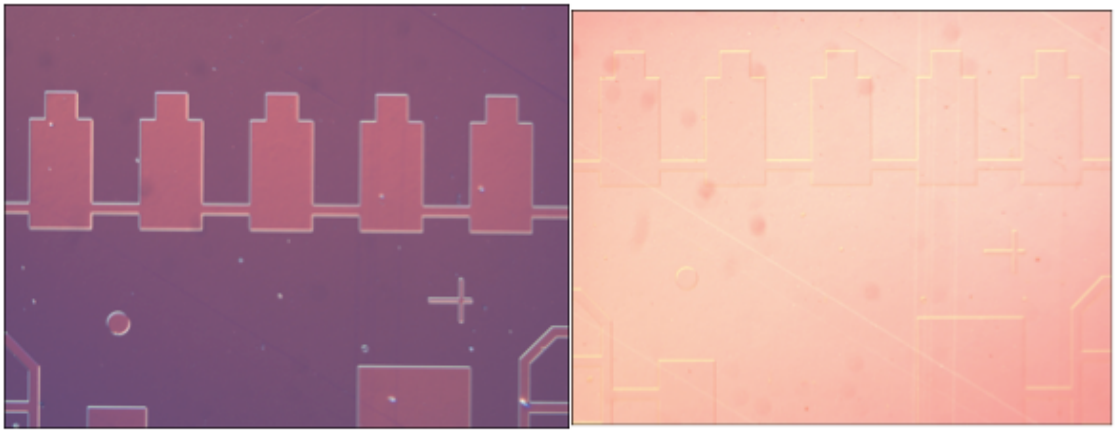

b) c)

Fig. 3.7 a) Schematic illustration of the reactive ion etching system. b) Top view of the AlGaN/GaN HEMT mesa structure with Mo/Ni sacrificial mask. c) Sample with mesa pattern after lift-off.

### 3.5. Rapid thermal annealing

Rapid thermal annealing (RTA) is a process of alloying and inter-diffusing multilayers of contact metals and semiconductor atoms at the metal-semiconductor interface in order to reduce the electrical voltage drop. Proper control of process parameters, such as temperature, time, ambient, etc. are very important to create low resistance metal-semiconductor contacts. In the fabrication of AlGaN/GaN HEMT, RTA is done to realize the good ohmic contact. This process alters the electrical properties of the contacts and can be optimized accordingly. Fig. 3.8 shows the custom-made strip heater RTA system. It consists of a vacuum chamber, a variable transformer (which controls the current through the carbon heating strip), and an infrared optical pyrometer (which is calibrated with the black body emission and focused at the edge of the sample to monitor the temperature). After loading the sample, the chamber was pumped down to a base pressure of $2\times10^{-7}$ torr to remove the possible moisture and contaminant gases. Then the research grade nitrogen gas was filled into the chamber. With the sample in place on the strip and gas flow on, current was ramped-up to anneal the sample at 750°C temperature for the amount of 30 seconds. Afterwards, the current was turned off, and the temperature was immediately brought down to a room temperature.

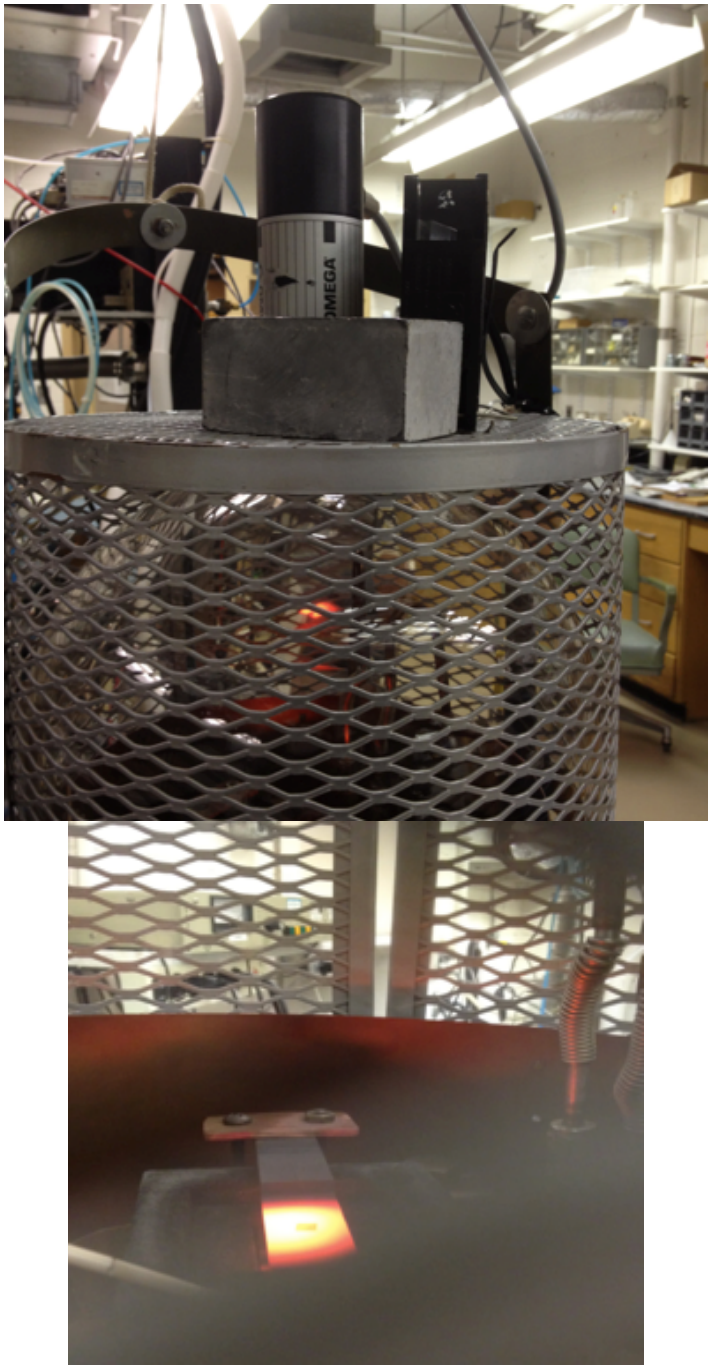

Fig. 3.8 Rapid thermal annealing chamber with the infrared pyrometer and carbon strip heating system (top). Close-up photograph of the carbon strip during annealing (bottom).

### 3.6 Lift-off

Lift-off is a lithographic pattern transfer process to a resist-patterned substrate by depositing a material over it and dissolving the resist to the suitable solvent to "lift-off" the material that is being deposited on top of the resist. Lift-off can be accomplished by immersing the substrate into acetone, since acetone easily dissolves the photoresist. Lift-off primarily depends upon the film quality of the deposited material. If the film is dense and thick, it will become more impermeable to the solvent and will take longer to lift-off. Moreover, pre-bake & film deposition temperature, exposure dose, resist developer parameters, etc. also affects the overall lift-off process. The general lithography with the lift-off process is shown in the Fig 3.4 in which a photo-patterned and metal deposited substrate is processed for lift-off. During the lift-off, photoresist under the metallic film was removed with the solvent, whereas metallic film that was deposited directly on the substrate remains. Image-reversal lithography process, which makes the lift-off process easy by creating an undercut profile with a negative slope, had been used in this dissertation.

### 3.7 Wire bonding

Wire bonding is a process in which a thin metal wire is welded onto the packaging pad and the metallized device in the integrated circuit (IC) by a solid-state ultrasonic/thermosonic welding. The bonding primarily depends upon the combination of normal bond force $F_B$, normal impact force $F_I$, bonding temperature as well as ultrasonic tangential force $F_T(t) = F_T \sin(2\pi f t)$, with $f$ being the ultrasonic frequency and $t$ being the time. In general, wire bonding can be of ball-wedge bonding and wedge-wedge

bonding as shown in the Fig. 3.9 (d). West bond 545657E-79 semi-automatic wedge-ball bonder had been used for the bonding. In the ball-wedge bond, first bond (ball bond) is performed on the substrate pad and the second bond (wedge bond) is performed on the device. The bonding head uses thermosonic mechanism in which ultrasonic vibration and thermal heating makes an electrical connection with the bonding pad and the device to produce an electrically conductive and mechanically strong bond. A high voltage DC current creates an arc between the electric flame off (EFO) unit and the tail of the wire beneath the capillary. Surface tension reforms the shape of the molten wire into the spherical ball known as a free air ball (FAB). The capillary holding FAB touches the bonding pad with an impact force resulting in an initial deformation. This is followed by the plastic deformation of the ball due to the normal bonding force, ultrasonic energy and the thermal energy. This results into the first ball bond on the substrate. The capillary is then guided on to the second bonding location. With the normal bonding force, ultrasonic & thermal energy, wire is deformed and bonded to the sample. In order to align the bonding position, the bonding system can be moved in the three axes, namely: X, Y and Z. X and Y axes are driven by micromanipulator for positioning, and held by pneumatic brakes for bonding, whereas Z axis is manipulated by the programmable motor to create an arc for the connection. The heated clamping stage provides the thermal energy, which also holds the substrate to be bonded.

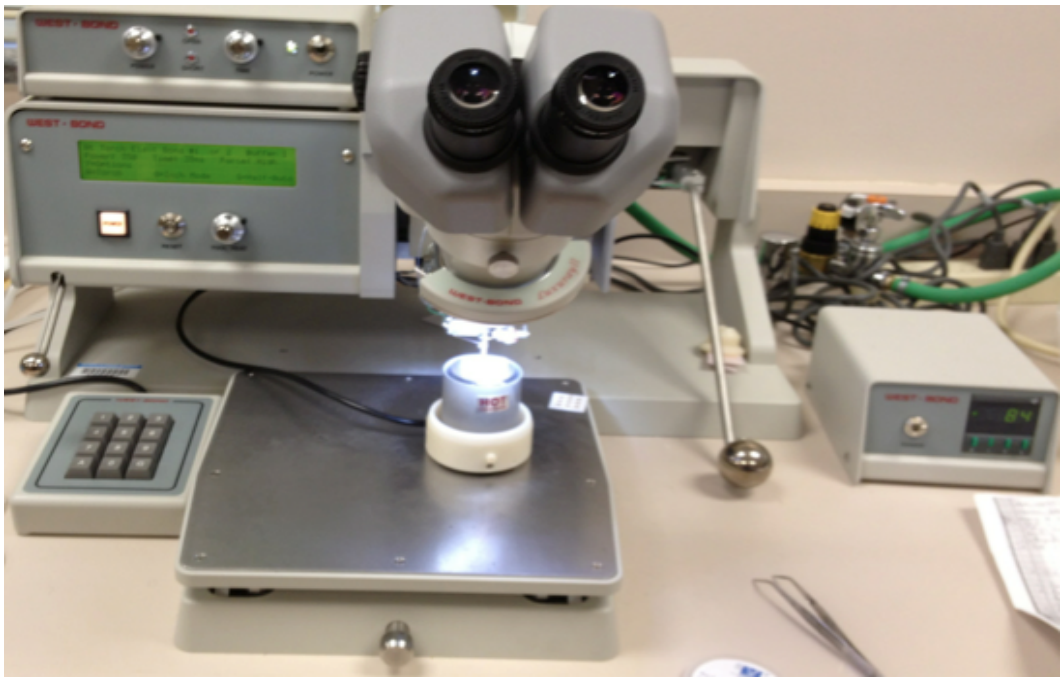

a)

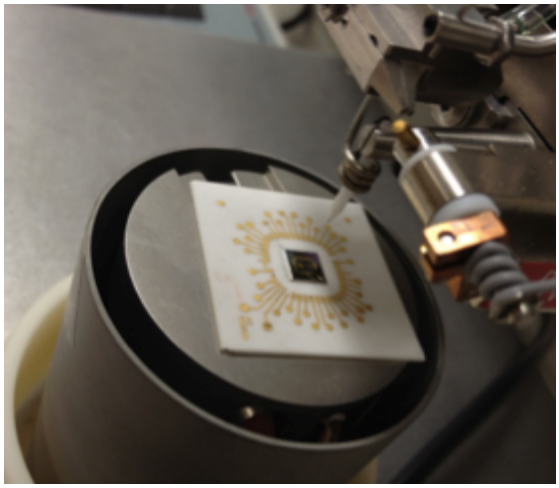

b)

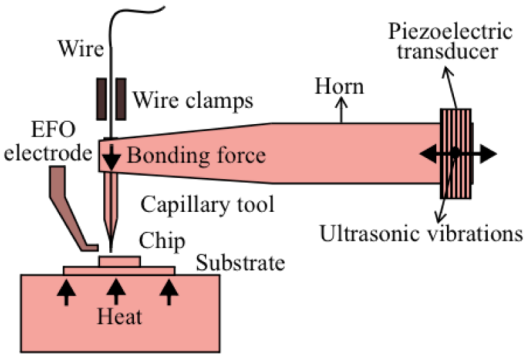


c)

d)

Fig. 3.9 a) Photograph of west bond thermosonic bonder b) Close up view of the tool c) Schematic diagram of the thermosonic wire bonding process (Reproduced from[12]) d) Side view of the ball-wedge bond and wedge-wedge bond. (Reproduced from[13])

### 3.8 Encapsulation

The electrical sensing mechanism of the field effect transistor based biosensor involves the aqueous solution of the biomolecules to be immobilized on the gate electrode. This requires the aqueous sample in the gate electrode be effectively isolated from the source and drain electrodes to avoid any electrical shorting. At the same time, the encapsulant needs to be biocompatible, mechanically & thermally stable, and good adhesive to the substrate.

Encapsulants frequently used to create a microchannel and other free standing structure in bioMEMS includes: polydimethlysiloxane (PDMS) elastomer, SU-8 and photopatternable silicone (PPS). Though biocompatible, PDMS is formed by relief casting and might be more challenging to create a mechanically isolated microstructures. On the other hand, SU-8 is high in autofluorescence, making it less desirable in high-contrast fluorescence imaging.[14] PPS combines the features such as biocompatible, low autofluorescence, better alignment capabilities with moderately high resolution ($\sim 10\ \mu m$). For the purpose, commercially available photopatternable spin-on silicone (PPS, Dow Corning, WL-5150) has been used to create a microreservoir at the gate electrode and encapsulate the source and drain electrode of the HEMT.

In order to create a desired microstructure, standard soft-lithography based microfabrication techniques have been used in this study. Processing steps are similar to that of the negative photoresist process with different parameters and includes:

1) Spin-coating of PPS
2) Pre-exposure bake (soft bake)
3) UV exposure

4) Post-exposure bake (post bake)
5) Development
6) Hard bake

At first, few milliliters of PPS elastomer was poured over the wire bonded device and spun to achieve a uniform layer. In order to promote the adhesion, it was first spun at 500 RPM for 10 seconds and followed by 1500 RPM for 30 seconds to achieve the uniformity and desired thickness.

The first thermal treatment of the processing was done by backing it at 110℃ for 150 seconds. This step reduces the solvent content, makes it less viscous and increases the adhesion. The soft bake does not crosslink the PPS, but reduces the tackiness making it easier to handle.

After the prebake, the sample was exposed to broadband UV radiation for the time of 5 minute 30 seconds in order to activate the photosensitive catalysts present in the PPS. In order to cross-link the PPS elastomer, sample was baked at 150 ℃ for 55 seconds. This is the most crucible step in the processing and appreciably affects the resolution of the pattern. The cross-linking of the exposed part makes it insoluble in the developing solution. The sample was then dipped into the developer solution for 25 seconds and spun at 5000 rpm for 2 minutes. The spin rate and time can be varied to optimize the resolution. Once the pattern was verified, the device was then hard baked at 150 ℃ for 30 minutes to cure the tackiness.

**References**

[1] J. H. Seinfeld and S. N. Pandis, "Atmospheric chemistry and physics: from air pollution to climate change" New York: Wiley, (1998).

[2] P. A. Kittle, "Surface treatment of semiconductor substrates", Patent, **US 6,797,071 B2** (2004).

[3] A. Kuliev, V. Kumar, R. Schwindt, D. Selvanathan, A. M. Dabiran, P. Chow, I. Adesida, "0.15 μm gate-length AlGaN/GaN HEMTs with varying gate recess length", Solid State Electron. **47**, 117 (2003).

[4] S. W. King, J. P. Barnak, M. D. Bremser, K. M. Tracy, C. Ronning, R. F. Davis and R. J. Nemanich, "Cleaning of AlN and GaN surfaces", J. Appl. Phys. **84,** 5248 (1998).

[5] M. Dialea, F. D. Aureta, N. G. Van der Berga, R. Q. Odendaala, W. D. Roosb, "Analysis of GaN cleaning procedure", Appl. Surf. Sci. **246**, 279 (2005).

[6] L. L. Smith, S. W. King, R. J. Nemanich, R. F. Davis, "Cleaning of GaN surfaces", J. Electron. Mater. **25**, 805 (1996).

[7] M. Rothschild, T. M. Bloomstein, T. H. Fedynyshyn, R. R. Kunz, V. Liberman, M. Switkes, N. N. Efremow, Jr., S. T. Palmacci, Jan H.C. Sedlacek, D. E. Hardy, and A. Grenville, "Recent trends in optical lithography", Lincoln Laboratory Journal **14**, 2 (2003).

[8] S. A. Campbell, The science and engineering of microelectronic fabrication, 2nd Ed.,

Oxford University Press, New York, NY (2001).

[9] R. Williams, "Modern GaAs processing methods", Artech House, Boston, 153 (1990).

[10] D. A. Stocker E.F. Schuber, and J. M Redwing, "Crystallographic wet chemical etching of GaN", Appl. Phys. Letts. **73**, 2654 (1998).

[11] Ruonan Wang, Yong Cai, Wilson C. W. Tang, Kei May Lau and Kevin J. Chen, "Device isolation by plasma treatment for planar integration of enhancement/depletion-mode AlGaN/GaN high electron mobility transistors", Jpn. J. Appl. Phys. **46,** 2330 (2007).

[12] A. S. Shah PhD thesis "Mechanical and tribological aspects of microelectronic wire bonding", http://uwspace.uwaterloo.ca/handle/10012/5109 (2010).

[13]J. Schwizer, M. Mayer, and O. Brand, 'Force sensors for microelectronic packaging applications", Springer, Berlin Germany (2005).

[14] S. P. Desai, B. M. Taff, and J. Voldman, "A Photopatternable silicone for biological applications" Langmuir **24**, 575 (2008).

# Chapter 4

## AlGaN/GaN high electron mobility transistor for DNA hybridization detection

### 4.1 Introduction

It has been shown that field-effect transistor (FET) based sensor can be used for the detection of biomolecules.[1,2,3,4] The FET-based sensor was also employed for the detection of deoxyribonucleic acid (DNA) hybridization. This method offers a "label-free" route to detect the biomolecules due to the intrinsic molecular charges and the counter-ions they attract. The FET sensors amplify the change in surface potential during the immobilization and hybridization event, and provide fast electrical readout. In addition, the FET sensors are based on the well-established microfabrication technology, which makes their incorporation into the electronic circuit convenient.

Due to its intrinsic materials and device characteristics, DNA biosensors based on AlGaN/GaN high electron mobility transistor (HEMT) are considered to be superior to conventional FET-based ones.[5] 1) AlGaN and GaN are chemically inert, and thermally and mechanically stable to be used in a harsh biochemical environment. 2) The energy band gap of these materials are wide to minimize spurious electrical signal from being generated.[6] 3) They possess high concentration of sheet carrier that was induced by the spontaneous and piezoelectric polarization, providing increased sensitivity. In the AlGaN/GaN heterostructure, band bending occurs on the upper part of the GaN layer, creating a highly mobile 2-dimensional electron gas (2DEG). This conductive channel

lies proximity to the surface and is highly sensitive to the minute change in the surface potential caused by the immobilization and hybridization of the DNA strands. 4) Also, HEMT-based DNA sensor can be operated without the reference electrode, which greatly reduces the volume of the reagents necessary for the detection and also simplifies the experimental setup.

Over the years, many different strategies have been employed to immobilize the biomolecule on the FET.[1,2,7,8] Among them, attachment of the thiolated probe DNA on the gold gate electrode has been used widely. This immobilization chemistry involves substantial rearrangement of the DNA films: possibly changing from virtually flat on the Au gate electrode to the tethering via one or two bases in addition to the thiol-Au bonding[9] thereby directly affecting the surface potential over the time.

Among the reported results; Kang *et al*[2] reported the increase in the drain current while Wang *et al*[3] and Alur *et al*[4] showed the decrease in the drain current upon immobilization of the thiolated probe on the HEMT. Though highly sensitive, this approach potentially present the higher possibility of the non-specific binding due to the charged biomolecule interacting very closely with the metal surface. Other groups have also shown the successful attachment of the probes directly on the semiconductor surface.[7] Without the rectifying effect of Schottky contact, direct attachment of the DNA probes on the semiconductor surface generates small electrical signal, thereby decreasing the overall sensitivity. In order to minimize the non-specific binding while retaining its sensitivity, we functionalize the gate electrode of the HEMT with self-assembled monolayers (SAMs) of alkanethiols to covalently bind the aminated probe. The role of the mercaptoundecanoic acid (MUA) SAMs in binding of the probe onto the gold surface has been well

studied.[10,11,12] This modification of the surface adds the overall length only by 1-3 nm. For low ionic strength of the buffer and suitable length of the probe, change in the charge density occurs within the Debye length for the successful detection.[13] In addition to providing the alternative route for the immobilization, we believe that this surface chemistry results in better specificity. Covalent attachment of DNA probe to the SAM provides a better control over the site where the attachment occurs and also prohibits the physisorption of the probe on the gate metal by enhancing the coverage of the immobilized probe DNA. Specificity of the detection is of great importance in order to avoid the misdiagnosis and the some trade-off between specificity and the sensitivity is beneficial.

**4.2 DNA structure**

DNA is a double helix structure whose inner core consists of stacked array of heterocyclic aromatic base pairs wrapped within the negatively charged sugar phosphate backbone as shown in Fig. 4.1. The double helix is composed of individual polymer chains, commonly referred as DNA strands. Each strand, along with its sugar phosphate backbone, is made up with the 4 different base pairs namely: Adenine (A), Thymine (T), Guanine (G), and Cytosine (C) as depicted in Fig 4.1. Each base of the DNA preferably bonds with another specific base to make a double helix structure. A bonds with T, G bonds with C and vice versa. The base pairs (A, T) and (G, C) are thus known as complementary base pairs and the bonding of two complementary DNA strands is called hybridization. In the hybridized structure, one strands of the double helix extends from 5′ to 3′, and the other from 3′ to 5′. The binding of the two complementary strands is

facilitated by the hydrogen bond between the base pairs; two bond between A and T, and three bond between G and C. In an aqueous medium, DNA molecules are highly dynamic and undergo dynamic motion on a time scale of picoseconds to milliseconds.[14,15,16,17,18] Water molecules, counterions and co-ions present in the solution reshapes the structure of the DNA in a solution.

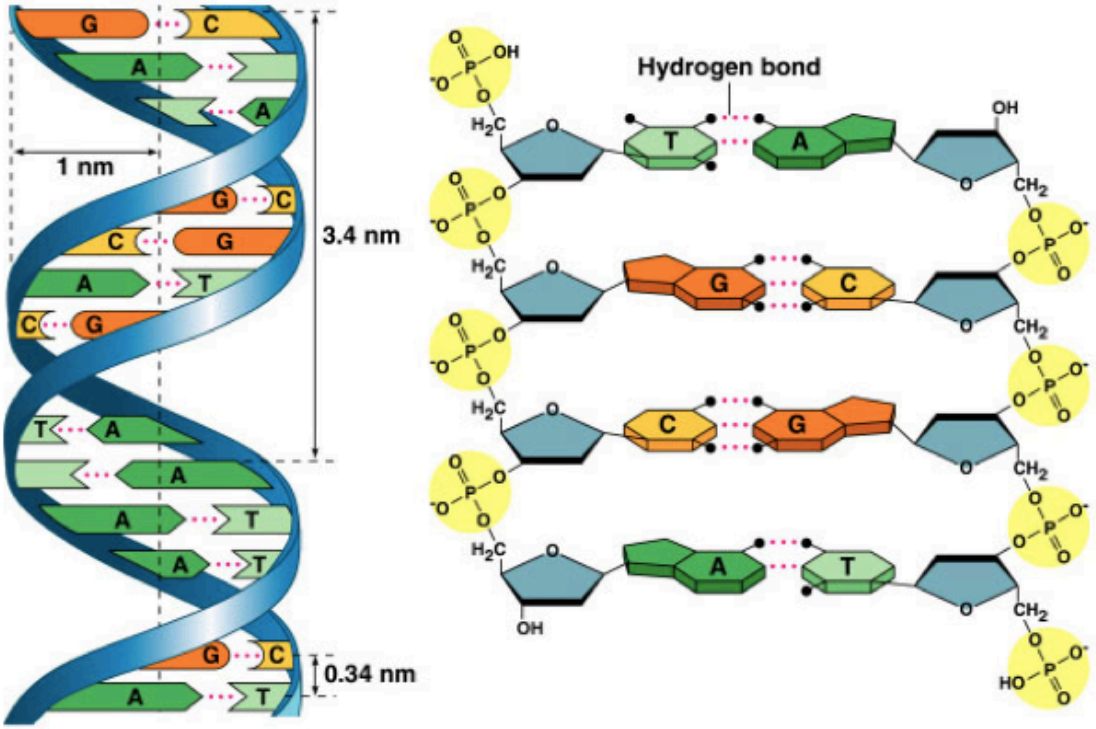

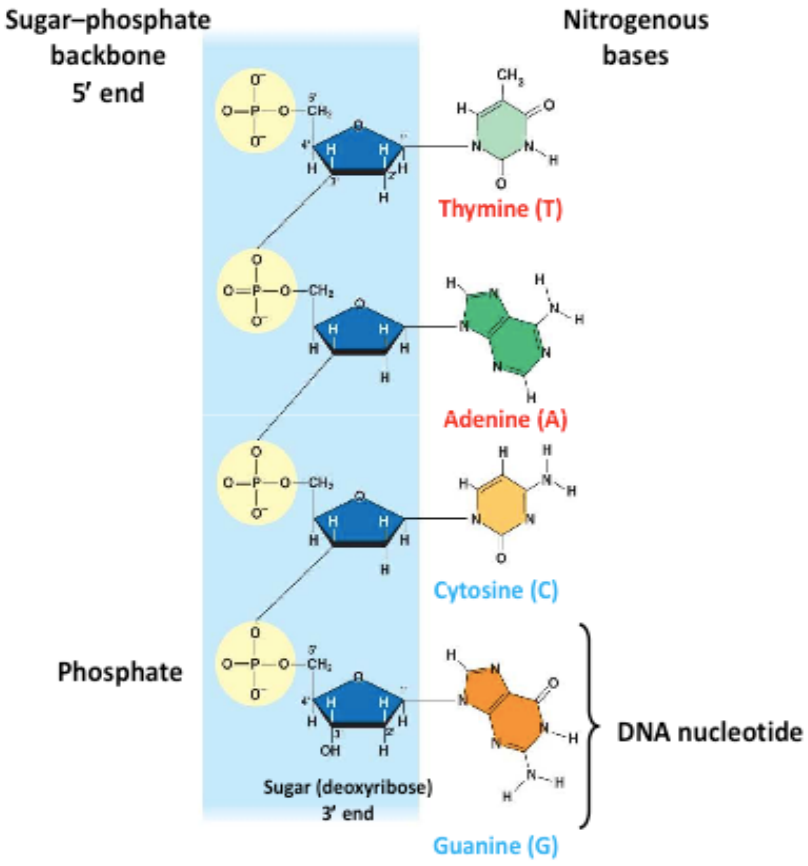


Fig. 4.1 DNA structure (Copyright © 2002 Pearson Education, Inc., publishing as Benjamin Cummings).

### 4.3 Self assembled monolayers of 11-MUA

Self assembled monolayers (SAMs) are an ordered molecular assemblies that are formed spontaneously by the adsorption of the surfactant on the solid surface. SAM of an alkanethiols are widely studied for their possible application in biosensor, nanofabrication and interface modification. The molecular structure of alkanethiol consists of thiol head group, carbon chains and tail or end group as shown in the Fig. 4.2. The thiol head group acts as an anchor and covalently bonds with the gold due to a strong affinity of sulfur to gold. The long carbon chain acts to stabilize the molecules by the Van der Waals

interactions. The tail group can be chemically modified to attach the functionalized molecules making the monolayer powerful interfacial layer.

The most common approach to grow SAM is by using the solution method. Solution based growth gives an attractive alternative because of its simplicity and does not involves any expensive equipment. In this approach, substrate is immersed into the dilute ethanol solution of thiols for about 20 hrs. Longer time of immersion helps to form more ordered molecular structure. The growth rate has been observed to be faster initially and much slower with the time. This is attributed to the aligning of the hydrocarbon chains and reorientation of the tail groups.[19,20,21,22,23,24] In addition to immersion time; solution concentration and surface structure/cleanliness also influences the monolayer density and organization.


Fig. 4.2 Schematic structure of the 11-MUA. (Reproduced from[25])

**4.4 UV-Vis absorption spectroscopy**

UV-Vis (ultraviolet-visual) absorbance spectroscopy is basically the measurement of the light absorbed by the sample. When light is passed through the sample, some of it

gets absorbed and transmitted by the sample. The difference between the incident and transmitted light is used to measure the absorbance. In UV-Vis spectrum, visible region of the spectrum comprises photons of energy between 36 to 72 kcal/mole whereas near UV to far UV region of the spectrum extends this energy range to 143 kcal/mole.[26] When the molecular transition energy of the sample matches the energy of the incoming photon, then the photon is likely to be absorbed. The absorbance can occur if,

$$\Delta E = E_{Photon} = h\nu = h\frac{c}{\lambda} \qquad [4.1]$$

where $h, \nu, c$ and $\lambda$ are plank's constant, frequency, speed and wavelength of the photon respectively. If the energy gap between the quantum states is larger, it requires photon with the smaller wavelength for the absorbance. So the different wavelength of the electromagnetic spectrum causes the different levels of molecular transitions from molecular rotational transition to electronic transition.

The 4 nucleotide bases present in the DNA has slightly different absorption spectrum and the total absorption spectrum is the average of each of them. Typical UV-Vis spectrum of DNA consists of the absorption peak near 260 nm and dip between 220 and 230 nm. The DNA solution is transparent in the visible spectrum, whereas it is almost opaque in the far ultra-violet region. The absorbance of single strand DNA is higher than that of the double strand DNA. This decrease in absorbance due to the DNA duplex formation is called hypochromic effect. Above the melting temperature of the DNA, double helix structure denatures and absorbance gets increased by about 30%. This increase in absorbance is called the hyperchromic effect and results due to the interaction between stacked dipoles in the double helix structure.

## 4.5 Experiment

For the experiment, we have used the HEMT wafer with AlGaN/GaN heterostructure grown on Si (111) substrate. The HEMT structure was grown at SVT Associates, Inc. and the structure is consisted of 0.3 μm thick resistive AlN buffer layer, 1.2 μm thick resistive GaN layer, 20 nm thick $Al_{0.25}Ga_{0.75}N$ layer, and 2 nm thick GaN cap layer. Prior to the device fabrication, the sample was cleaned in a series of organic (acetone, trichloroethylene, acetone, methanol, and methanol) solvent using an ultrasonic bath fro 5 minutes each, and in an acidic solvent (1:1 by volume of HCl + DI water) at 110°C for 10 minutes. After cleaning the sample for removal of any contaminants, mesa isolation was achieved with a reactive ion etching (RIE)/$F^-$ implantation in fluorine plasma. Mo (200 nm)/Ni (100 nm) was used as a sacrificial mask and $H_2O_2$ was used to etch the Mo after RIE. For ohmic contacts, Ti (50 nm)/Al (150 nm)/Ni (50 nm) multilayers were deposited and the sample was subsequently annealed at 750°C for 30 seconds in $N_2$ rich chamber. This helps to reduce the contact resistance and assists for better adhesion between metal and semiconductor. After annealing, layers of Cr (40 nm)/Au (100 nm) were deposited on top of the annealed ohmic contact. Schottky contact was then made by depositing Ni (30 nm) and Au (80 nm). All of these processes were performed with standard lithography, sputtering and lift-off techniques. After the wire bonding, photopatternable spin-on silicone (Dow Corning WL-5150) was used to encapsulate the device except for the active gate region with a dimension of 50μm (L) × 80μm (W) ×15μm (H) as shown in Fig. 4.3.

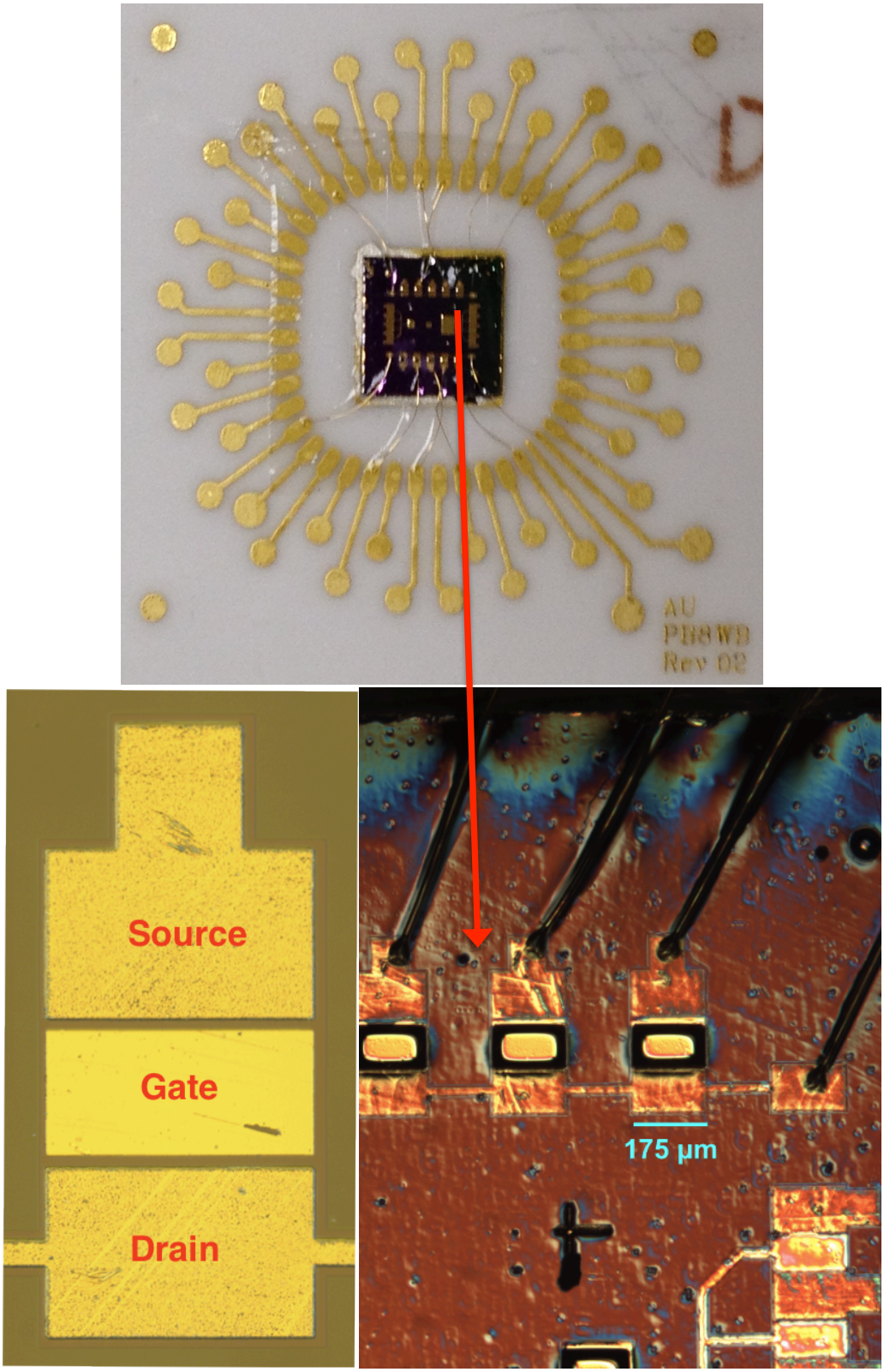


Fig. 4.3 Photograph of the packaged sensor and transistor for the detection of DNA.

The fabricated device was first cleaned in an ethanol solution and successively immersed in a 1 mM solution of 11-Mercaptoundecanoic Acid (11-MUA, $HS(CH_2)_{10}CO_2H$) in ethanol for 18 hours. Then, the OH-terminated functional group was activated into amine reactive sulfo-NHS ester with 1 hour treatment of the mixture of EDC (1-ethyl-3′- [3-dimethylaminopropyl]carbodiimide hydrochloride, $C_8H_{17}N_3.HCl$) and sulfo-NHS (N-hydroxysulfosucccinimide, $C_4H_4NNaO_6S$). The device was then washed in the DI water and subsequently used for the aminated DNA probe immobilization. The schematic illustration of the surface functionalization and probe immobilization reactions are shown in Figure 4.4.

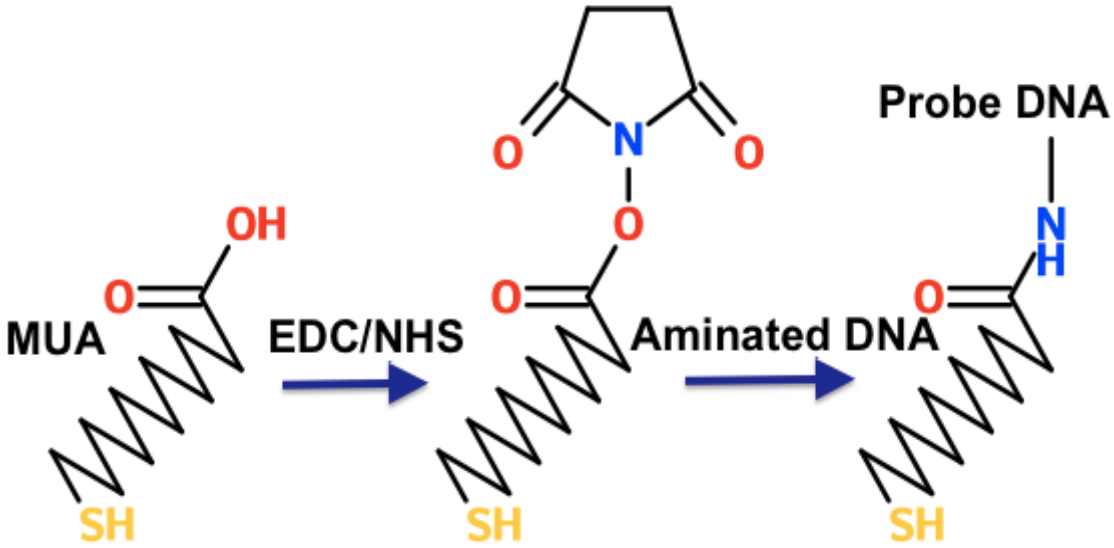


Fig. 4.4 Schematic illustration of the surface functionalization and probe DNA immobilization steps.

For the electrical detection of immobilization and hybridization of DNA sequences, three synthesized label-free 22-mer oligonucleotides were purchased from Integrated DNA Technologies, Inc. Amine modified probe DNA at the 5′ with a sequence

of 5′-/5AmMC6/CGC TTG AAG AGG TCA ATG GCC A-3′ that best represents that of salmonella was used for immobilization, while the target DNA with its complementary sequence of 5′-TGG CCA TTG ACC TCT TCA AGC G-3′ was used for the hybridization detection. As a control, 3 base pair (bp) mismatched DNA with a sequence of 5′-TGG ACA TTG ACC TAT TCA AGA G-3′ and 55 bp completely mismatched sequence was used.

A 10 µl of 1 µM probe DNA in 10 mM Tris-EDTA (TE, pH 7.4, Sigma Aldrich) buffer solution was hand-pipetted onto the functionalized gate electrode of the HFET for the probe DNA immobilization. After immobilization for 3 hours, 10 µl of the 0.1X phosphate buffered saline (PBS, pH 7.4, P4417 Sigma) buffer was hand-pipetted and carefully drawn back 2 times in order to remove the unbounded DNA strands. The device was then ready to detect the matched or mismatched DNA sequences. Exposed gate electrode of the HEMT was then treated with 5 µl of 1 µM 3 base pair mismatched and afterwards complementary target DNA in 0.1X PBS buffer. All of the electrical measurements were performed in the dark condition to avoid any parasitic effect.

**4.6 Results and discussion**

The HEMT wafer showed the 2DEG mobility ($\mu$) ~ 1700 $cm^2/V.s$ and the electron sheet career concentration ($n_s$) ~ $1.2\times10^{13}$ $cm^{-2}$ at room temperature. Adsorption of the MUA monolayer on the gold surface was studied by the X-ray photoelectron spectroscopy (XPS) measurement. Figure 4.5 shows an overview of the XPS spectrum for an ex-situ prepared 11-MUA SAM on DC magnetron sputtered gold substrate. In addition to the

gold peaks, $C_{1s}$ and $O_{1s}$ peaks are clearly visible whereas the sulfur $S_{2p}$ peak is barely visible. By using the higher resolution scan with narrower energy range and longer scan time, distinct $S_{2p}$ peak at 162.7 eV in the Figure 4.6 is observed, which is the characteristics to the gold-thiolate bond.[27] In addition, UV-Vis absorbance measurement in solution was performed to verify the DNA hybridization. The characteristic maxima near 260 nm in Figure 4.7 show the hybridization and denaturation of the DNA strands depicting the corresponding hypochromic and hyperchromic effect.

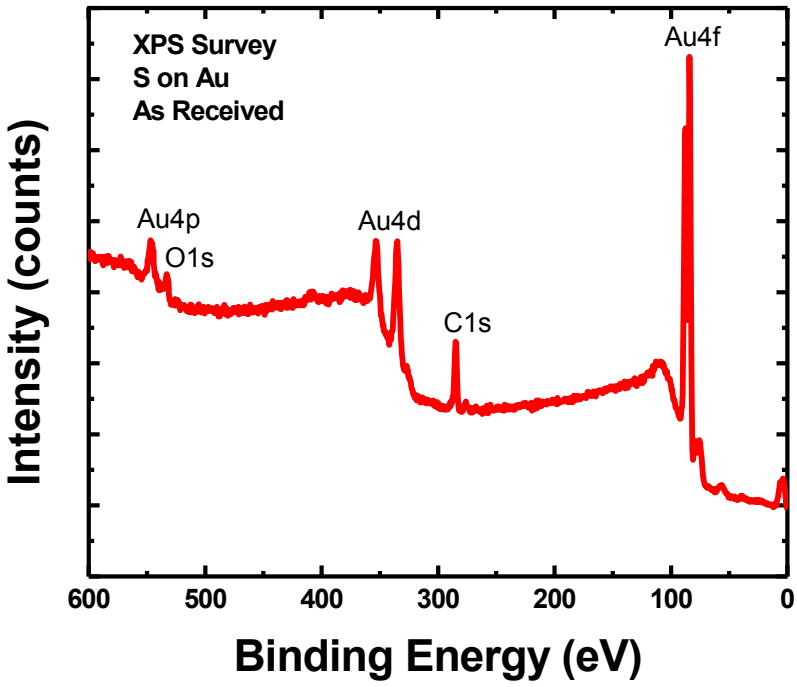


Fig. 4.5 Overview of the XPS spectrum for the MUA immobilized on the magnetron sputtered gold substrate. The sulfur signal is relatively too small to be distinguished.

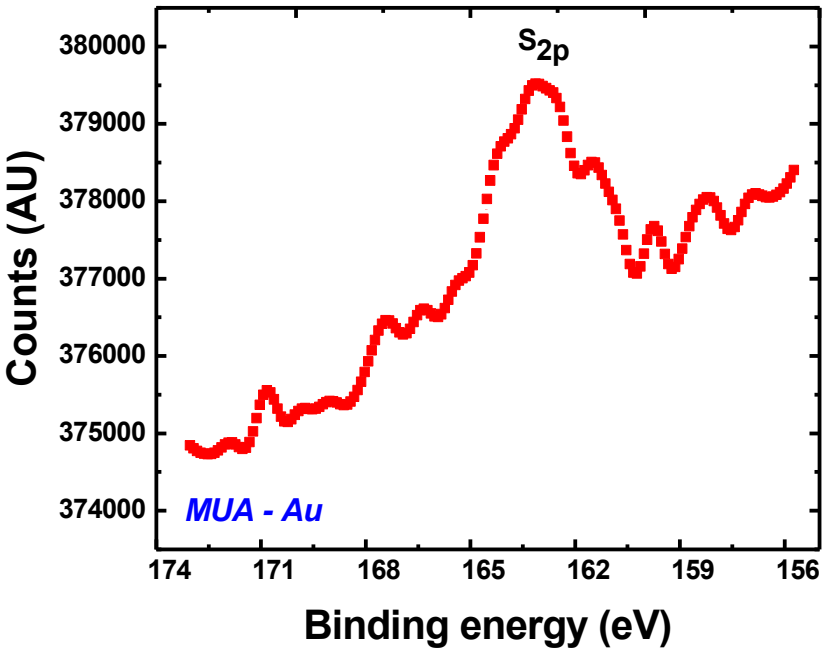


Fig. 4.6 High resolution XPS spectrum for the gold-thiol bond. S2p peak at 162.7 eV indicates the sulfur adsorption onto the gold.

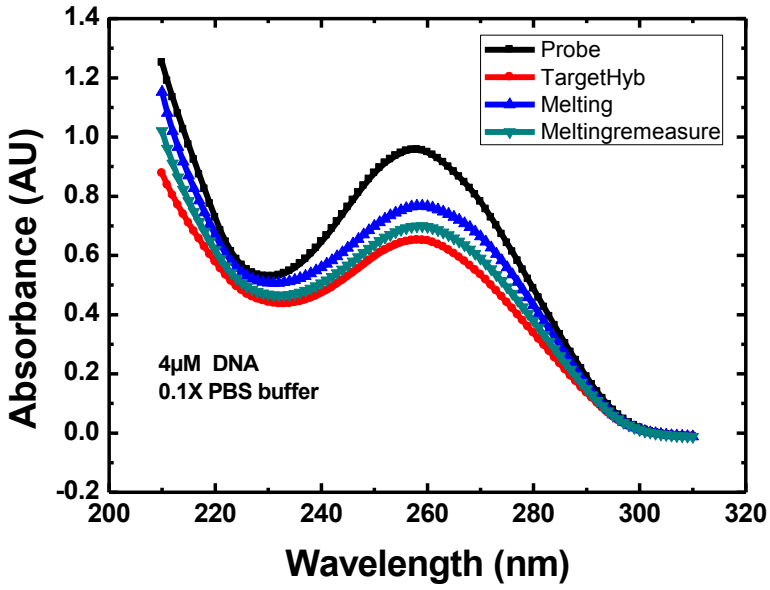


Fig. 4.7 UV-Vis absorbance spectrum of the single strand DNA, hybridized DNA and the effect of heat denaturation.

UV-Vis absorbance spectrum in Fig. 4.7 and 4.8 shows the effect of DNA hybridization and heat denaturation on the absorbance intensity count (AU). Absorbance of ssDNA is greater than the dsDNA, whereas heat denaturation increases the absorbance intensity as expected. In addition, absorbance intensity in Fig. 4.7 is higher than that of the Fig 4.8 due to the higher concentration of DNA molecules. Decreased absorbance intensity few minutes after the melting indicates the re-hybridization between the ssDNA strands.

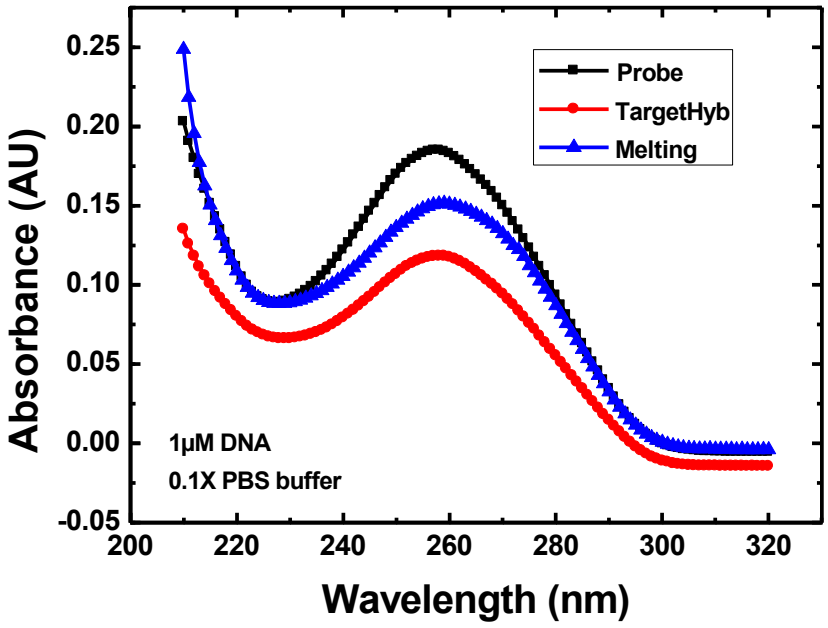


Fig. 4.8 UV-Vis absorbance spectrum of 1μM DNA molecules.

Source-drain current voltage ($I_D$-$V_{DS}$) measurement of the device just before and after the probe immobilization are shown in Figure 4.9. The source-drain current was

decreased after probe immobilization and the decrease in the drain current was around 100 μA at the source-drain bias of 1V.

In order to test the sensor in the event of DNA hybridization, the following transistor output and time-dependent experiments were performed and the results were plotted in Figures 4.10, 4.11, 4.12 and 4.13. Fig. 4.10 shows the typical output current characteristics of the transistor just before and after the hybridization with the completely matched DNA. Further, to measure of the current vs. time profile, the sensor was biased at 1 V and the source–drain current ($I_D$) was measured at an interval of 1 sec with the floating gate condition. Fig 4.11 (top) shows the effect of application of completely mismatched DNA on the probe DNA immobilized HEMT. The current vs. time profile showed very small or no change in the final current value. Fig. 4.11 (bottom) shows the output current characteristics of the transistor in the event of the application of 3 bp mismatched target DNA and complementary target DNA. The output current change was significant to distinguish the complementary and few base pair mismatched DNA sequences. In addition, specificity of the sensor is shown in Fig. 4.13. Initially, the 3 bp mismatched target DNA was introduced to the sensor, and slight decrease of the drain current by around 4 μA was observed. The same device upon the exposure of complementary target DNA showed a substantial decrease of drain current by around 25 μA, indicating hybridization of DNA.

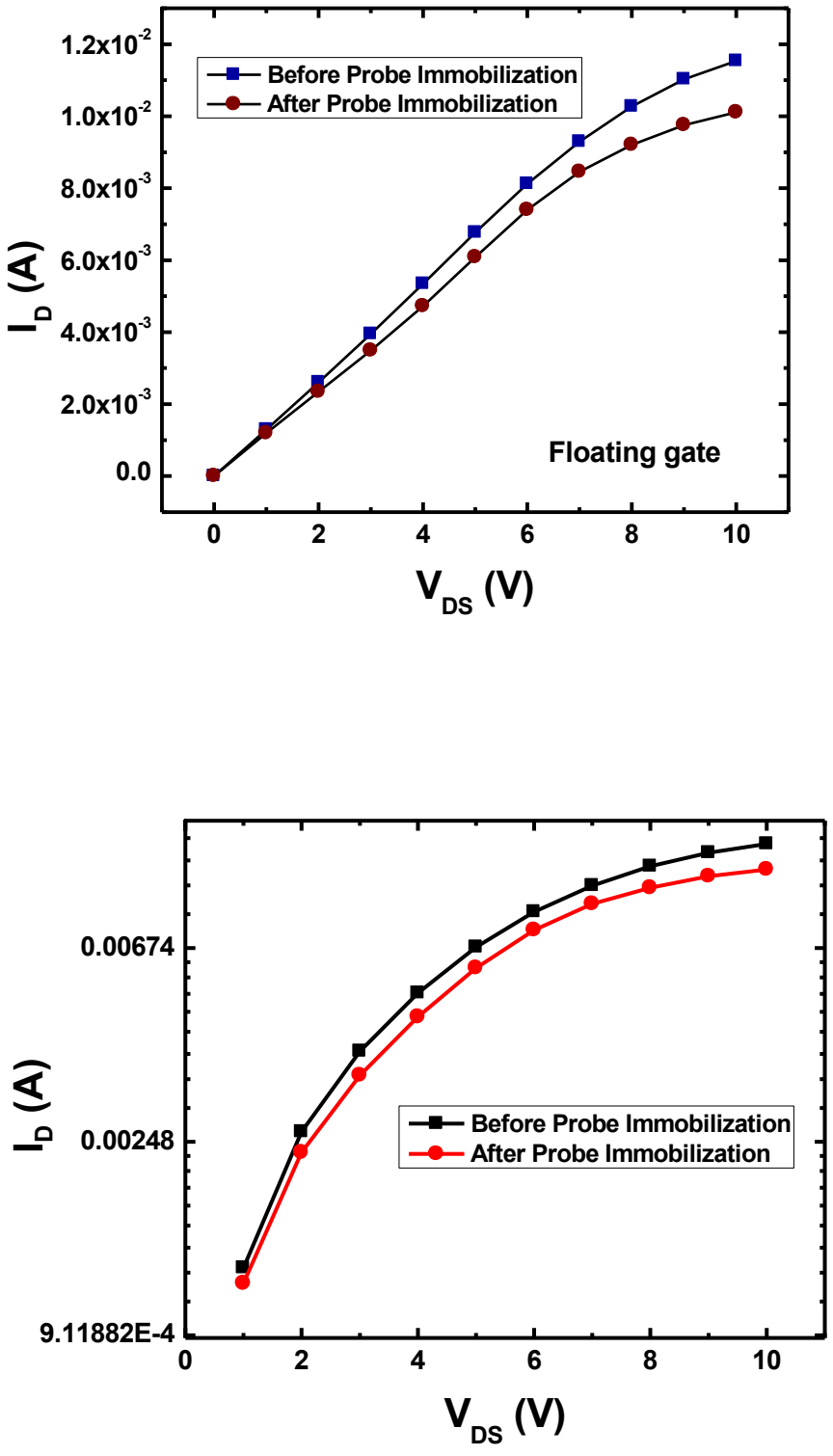


Fig. 4.9 Transistor output characteristics before and after the probe DNA immobilization.

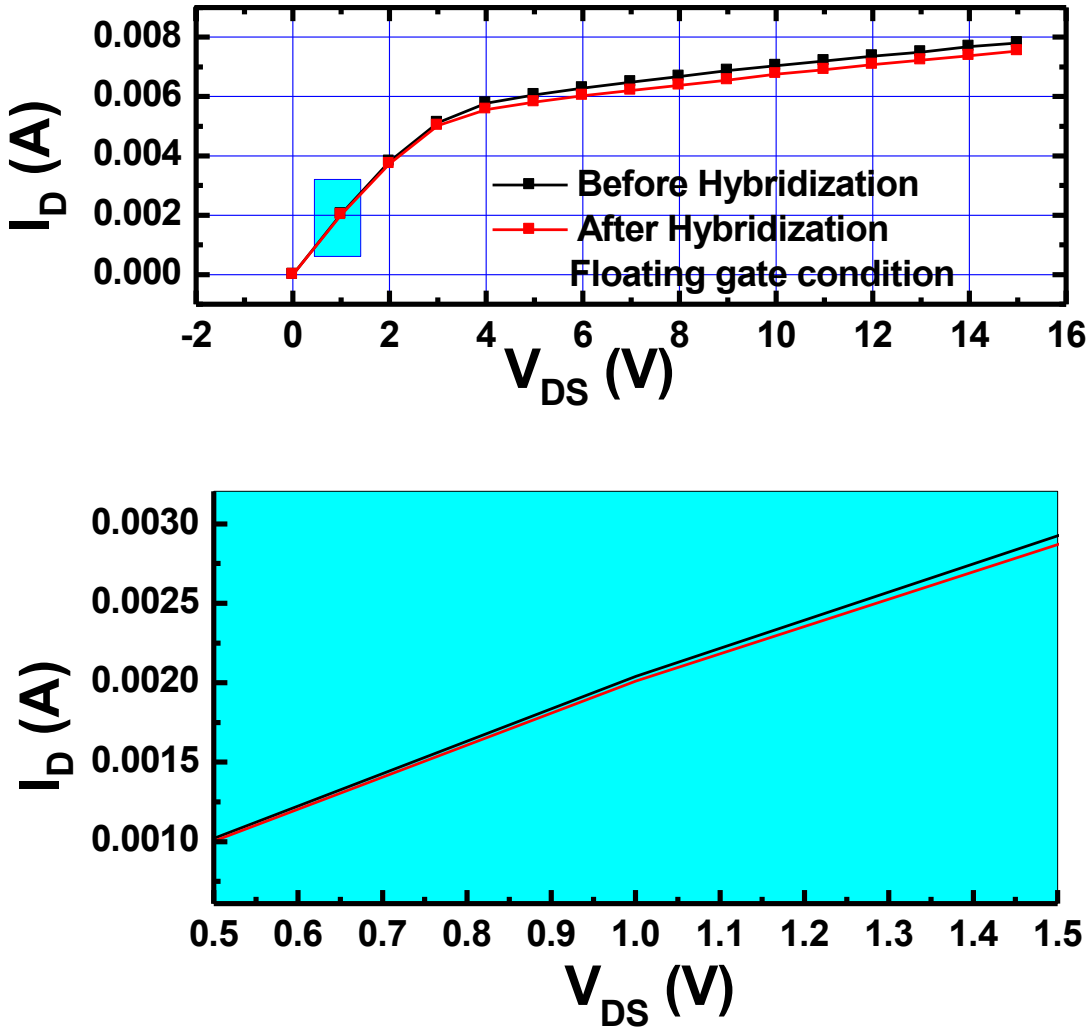


Fig. 4.10 $I_D$-$V_{DS}$ measurement of the transistor before and after the DNA hybridization (top). The small rectangular portion of the curve in top figure (in aqua color) is enlarged (bottom).

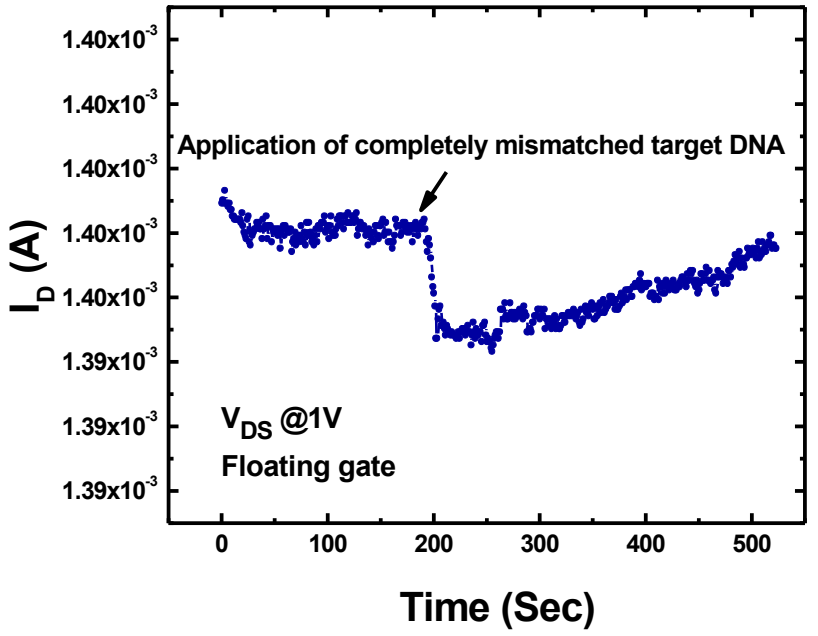


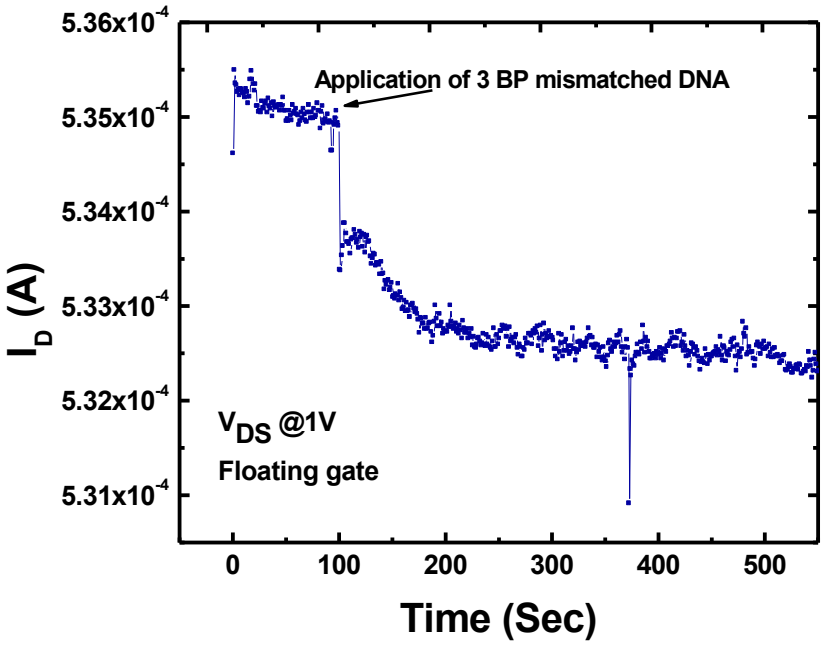


Fig 4.11 Current vs. time measurement of completely mismatched (top) and 3 base pair mismatched 1 µM target DNA. Application of the completely mismatched target DNA has very little effect on the output current characteristics.

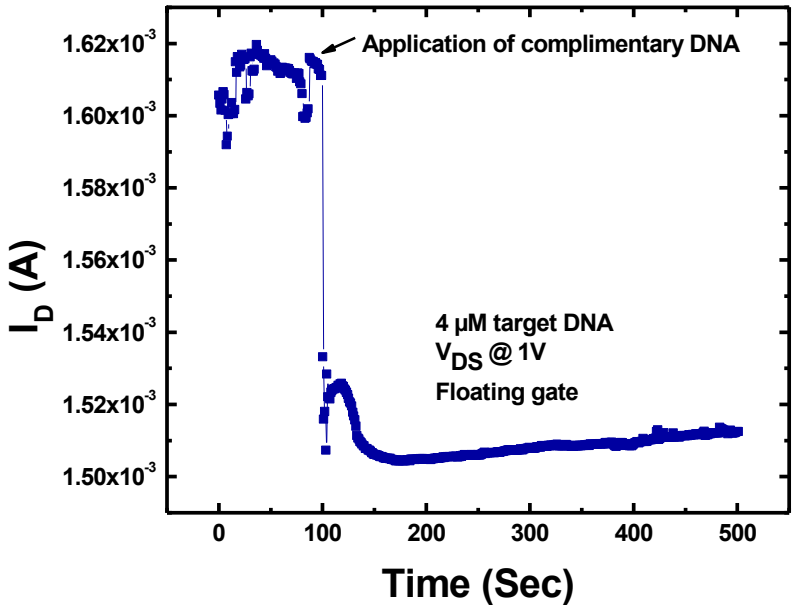


Fig. 4.12 Current vs. time measurement during the hybridization 4 µM complimentary target DNA.

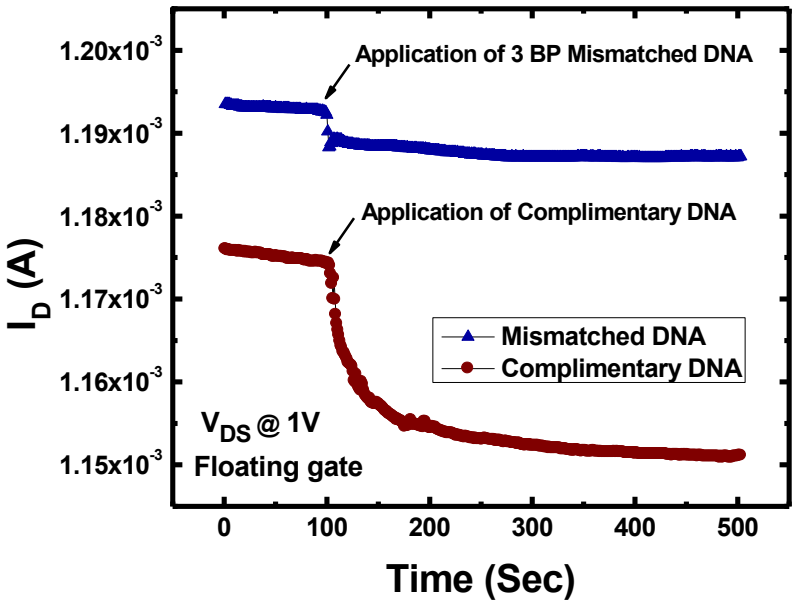


Fig. 4.13 Current vs. time hybridization measurements of 3 base pair mismatched and complimentary 1 µM target DNA.

Above results indicates that our sensing experiment exhibits high specificity, promising that the sensor with sensitivity of single base pair can be fabricated in the near future. It is hypothesized that the method of SAM-mediated immobilization of the aminated DNA may help reduce non-specific binding of the DNA on the gate electrode. We believe that use of MUA with aminated DNA provides with higher level of specific binding than direct attachment of thiolated DNA onto the gold gate does.

To explain the above results of overall decrease in the current, effect of surface modification and the charge transfer mechanism at the interface has been considered. In principle, electron and ion transfer from the electrolyte to electrode could take place in three ways, namely: electron tunneling, electrolyte permeating through the monolayer and diffusion through the possible pinhole defects.[28] Long-chain alkanethiols are known to be self-assembled into a well-ordered monolayer through van der Waal's interactions between them, effectively creating an insulating barrier. These chains typically tilt by $20^{\circ}$-$30^{\circ}$ from the surface normal, creating a strong resistance to electron and ion transfer processes. In order for a diffusion process to take place, the dimension of the pinhole defects need to be in the order of micrometer. Reported results indicated the low probability of these electron and ion transfer mechanism.[10-12,15] Thus it is suggested that the alkanethiols modified electrode-electrolyte interface as a dielectric capacitor in series with the Stern layer capacitor.[15,29] Furthermore, the Stern layer capacitance can be subdivided into two capacitance in series; namely, Helmholtz capacitance in Stern layer and the Gouy-Chapman capacitance in diffuse layer. In the case of low ionic buffer solution, Gouy-Chapman capacitance dominates the Helmholtz capacitance, thus the later can be

neglected. For higher ionic buffer solution, reverse will be true, making the detection of biomolecules in the diffuse layer impossible.

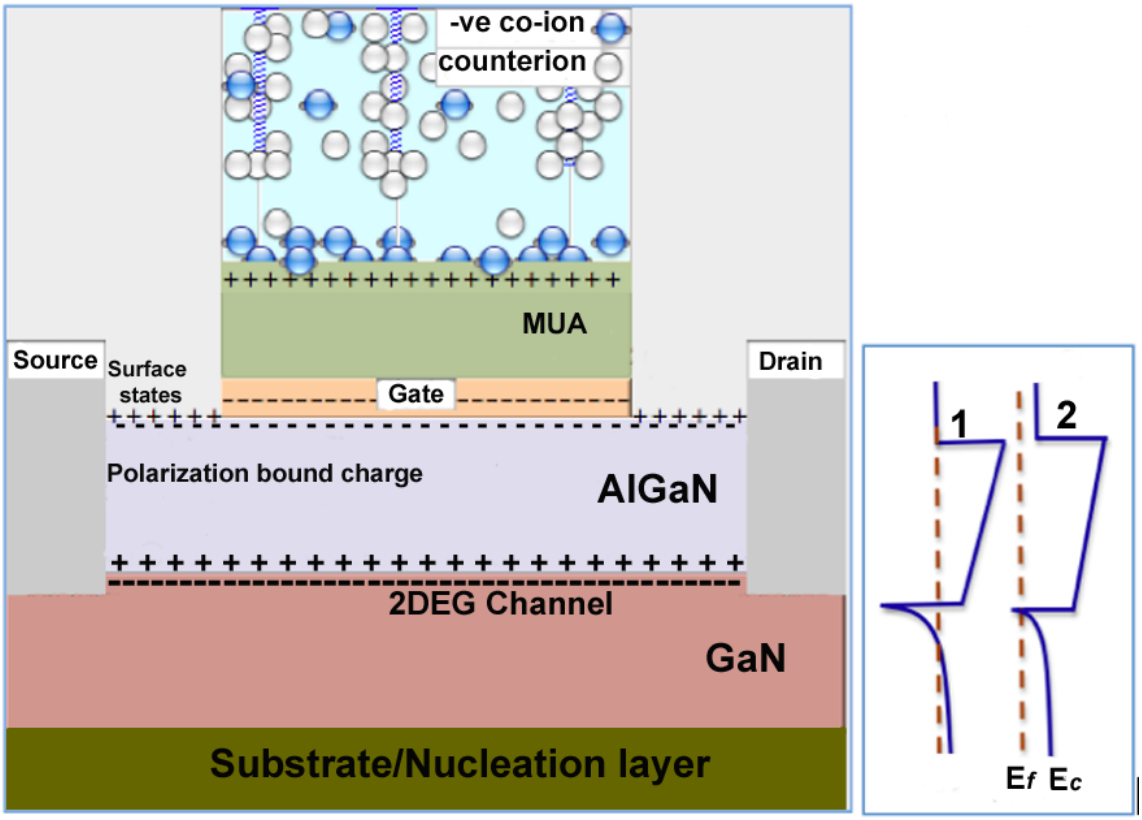


Fig. 4.14 (Left) Schematic cross-section and the interfacial capacitance at the gate electrode of the AlGaN/GaN HEMT, (Right) Bend in the conduction band arising from the DNA strands immobilization and hybridization.

As shown in Fig. 4.14 above, we suggest a capacitive model for the distribution of ions in a DNA buffer solution in contact with the charged organic interface during the immobilization and hybridization of DNA strands as: 1) Reactive thiol head group of the MUA with its net negative charge introduces negative surface potential on the gate electrode of the HEMT; 2) Positive charge of the amine-anchoring group of the probe in

physiological condition attracts negative co-ions towards it; 3) Mobile counterions such as $Na^+$, $K^+$ in the buffer solution will screen the DNA due to electrostatic interaction in the diffuse layer[7]; 4) Negative co-ions at the MUA-electrolyte interface and the ensemble of counterions that screens the DNA forms a Gouy-Chapman capacitance in diffuse layer; 5) The Debye length essentially is the thickness of the diffuse layer and is given for the monovalent electrolyte as

$$\delta = \sqrt{\frac{kT\varepsilon_e}{2Cq^2N_A}} \qquad [4.2]$$

where $k$ is the Boltzmann constant, $T$ is the absolute temperature, $\varepsilon_e$ is the permittivity of the electrolyte, $C$ is the electrolyte concentration in mol/$m^3$, $q$ is the electron charge, and $N_A$ is the Avogadro's number. Considering the 13 $mM$ NaCl buffer strength ($\delta \sim 2.8\ nm$), length of probe DNA ($22\ bp \sim 7.26\ nm$) with the spacer arm ($\sim 1.5\ nm$), only the ensemble of ions near the sensor surface should be detectible to the sensor. Hybridization essentially doubles the number of positive counterions near the sensor surface leading to the increase in the transistor output current. On the other hand, unhybridized strands being above the Debye length gets screened out and will not affect the transistor current characteristics.

In the undoped AlGaN/GaN HEMT, donor-like surface states are believed to be the substantial source of 2DEG electrons. The charge balance equation is given by[30]

$$\sigma_{Surface} + \sigma_{AlGaN} + \sigma_{Pol} + \sigma_{Buffer} - qn_s = 0 \qquad [4.3]$$

where $\sigma_{Surface}$ is the charge due to the surface states, $\sigma_{AlGaN}$ is the charge due to the ionized states in the AlGaN barrier, $\sigma_{Pol}$ is the charge induced by the polarization at the AlGaN surface $(-\sigma_{Pol})$ and AlGaN/GaN interface $(+\sigma_{Pol})$, $\sigma_{Buffer}$ is the charge due to the donor states in GaN layer, $q$ is the charge of an electron, and $n_s$ is the sheet carrier density at the 2DEG. In the undoped AlGaN/GaN HEMT, the net contribution due to the $\sigma_{AlGaN}$, $\sigma_{Pol}$ and $\sigma_{Buffer}$ on the total space charge distribution is zero. This suggests the 2DEG sheet carrier density is directly associated with the surface states. Combined with the trapped electrons in the surface states, capacitive coupling during the rearrangement of the ions during the immobilization and hybridization of the DNA molecules caused the depletion in 2DEG, and therefore reduced the drain current of the transistor. Band diagram number 1 and 2 in Figure 4.13 shows the effect of increasing negative surface potential on 2DEG carrier concentration. Sharp decrease in the small drain current in the case of 3 bp mismatched DNA sequence can be attributed to the effect of capacitive double layer in the buffer, while the gradual decrease indicates hybridization of the DNA strands.

**4.7 Summary and conclusions**

We have fabricated AlGaN/GaN HEMT based DNA sensor and have successfully demonstrated the hybridization of probe and complimentary target DNA. It is believed that amine-based biofunctionalization has enhanced specificity in DNA detection. A working model was presented to explain the detection mechanism. The overall results promise for realization of the label-free electrical DNA sensor with the specificity and sensitivity.

## 4.8 Future work

By using an extended gate field effect transistor, effect of variation in transistor characteristics on the DNA hybridization output signal can be minimized. This will make the comparative study between target sequences more reliable. Further study corresponding to different buffer and DNA concentration can give limitation of the detection.

**References**

[1]R. D-L. Rica, C. Fernández-Sánchez, C. Jiménez-Jorquera, and A. Baldi, "Spermine-induced hybridization and charge inversion at the diffuse layer of a DNA-FET", J. Phys. Chem. B **112**, 7614 (2008).

[2]B. S. Kang, S.J. Pearton, J.J. Chen, F. Ren, J.W. Johnson, R. J. Therrien, P. Rajagopal, J.C. Roberts, E.L. Piner, and K.J. Linthicum, "Electrical detection of deoxyribonucleic acid hybridization with AlGaN/GaN high electron mobility transistors", Appl. Phys. Lett. **89**, 122102 (2006).

[3] Y. Wang, W. Lu, "AlGaN/GaN FET for DNA hybridization detection", Phys. Status Solidi A **208**, 1623 (2011).

[4]S. Alur, R. Thapa, T. Ganaprakasa, Y. Wang, Y. Sharma, E. Javalosa, E. Smith, C. Ahyi, A. Simonian, M. Bozack, J. Williams, M. Park, "DNA hybridization sensor based on AlGaN/GaN HEMT", Phys. Status Solidi C **8**, 2483 (2011).

[5]G. Steinhoff, O. Purrucker, M. Tanaka, M. Stutzmann, and M. Eickhoff, "Surface functionalization and biomedical applications based on SiC", Adv. Funct. Mater. **13**, 841 (2003).

[6]U. K. Mishra, P. Parikh, Y. –F. Wu, "AlGaN/GaN HEMTs-an overview of device operation and applications", Proc. IEEE. **90**, 1022 (2002).

[7]S. U. Schwarz, S. Linkohr, P. Lorenz, S. Krischok, T. Nakamura, V. Cimalla, C.E. Nebel, and O. Ambacher, "DNA-sensor based on AlGaN/GaN high electron mobility transistor", Phys. Status Solidi A **208**, 1626 (2011).

[8]X. Tang, A.M. Jonas, B. Nysten, S. Demoustier-Champagne, F. Blondeau, P.-P. Prevot, R. Pampin, E. Godfroid, B. Iniguez, J.-P. Colinge, J.-P. Raskin, D. Flandre, and V. Bayot, "Direct protein detection with a nano-interdigitated array gate MOSFET", Biosens. Bioelectron. **24**, 3531 (2009).

[9]D. Y. Petrovykh, H. Kimura-Suda, L. J. Whiteman, and M. J. Tarlov, "Nucleobase Orientation and Ordering in Films of Single-Stranded DNA on Gold", J. Am. Chem. Soc. **125**, 5219 (2003).

[10]S.-J Ding, B.-W. Chang, C.-C Wu, M.-F. Lai, H.-C Chang, "Impedance spectral studies of self-assembly of alkanethiols with different chain lengths using different immobilization strategies on Au electrodes", Anal. Acta **554**, 43 (2005).

[11]S. Campuzano, M. Pedrero, C. Montemayor, E. Fatas, J. M. Pingarron, "Study of the size and separation of pinholes in the self-assembled thiol-porphyrin monolayers on gold electrodes", J. Electroanal. Chem. **586**, 112 (2006).

[12]X. Ding, J. Hu, and Q. Li, "Direct electrochemistry and superficial characterization of DNA-cytochrome c-MUA films on chemically modified gold surface", Talanta **68**, 653 (2006).

[13] A. Poghossian, A. Cherstvy, S. Ingebrandt, A. Offenhausser, M.J. Schoning,

"Possibilities and limitations of label-free detection of DNA hybridization with field-effect-based devices", Sens. Actuat. B **111-112**, 470 (2005).

[14] T. E. Cheatham, P. A. Kollman, "Molecular dynamics simulation of nucleic acids", Annu. Rev. Phys. Chem **51**, 435 (2000).

[15]P. N. Borer, "C-13-NMR Relaxation in 3 DNA Oligonucleotide Duplexes—Model-Free Analysis of Internal and Overall Motion", Biochemistry **33**, 2441 (1994).

[16] S. Georghiou, "Large-amplitude picosecond anisotropy decay of the intrinsic fluorescence of double-stranded DNA", Biophys. J. **70**, 1909 (1996).

[17]Z. C. Liang, J. H. Freed, R. S. Keyes, A. M. Bobst, "An electron spin resonance study of DNA dynamics using the slowly relaxing local structure model", J. Phys. Chem. B **104**, 5372 (2000).

[18]T. M. Nordlund, S. Andersson, L. Nilsson, R. Rigler, A. Graslund, L. W. McLaughlin, "Structure and dynamics of a fluorescent DNA oligomer containing the EcoRI recognition sequence: fluorescence, molecular dynamics, and NMR studies", Biochemistry **28**, 9095 (1989).

[19]O. Dannenberger, M. Buck, and M. Grunze, "Self-assembly of n-alkanethiols: a kinetic study by second harmonic generation", J. Phys. Chem. B **103**, 2202 (1999).

[20]K. A. Peterlinz, R. Georgiadis, "In situ kinetics of self-assembly by surface plasmon resonance spectroscopy", Langmuir **12**, 4731 (1996).

[21]C. D. Bain, E. B. Troughton, Y. T. Tao, J. Evall, G. M. Whitesides, R. G. Nuzzo, "Formation of monolayer films by the spontaneous assembly of organic thiols from solution onto gold", J. Am. Chem. Soc. **111**, 321 (1989).

[22]D. S. Karpovich, G. J. Blanchard, "Direct measurement of the adsorption kinetics of alkanethiolate self-Assembled monolayers on a microcrystalline gold surface", Langmuir **10**, 3315 (1994).

[23]F. Bensebaa, R. Voicu, L. Huron, T. H. Ellis, E. Kruus, "Kinetics of formation of long-chain n-nlkanethiolate monolayers on polycrystalline gold", Langmuir **13**, 5335 (1997).

[24]C. D. Bain, E. B. Troughton, Y. T. Tao, J. Evall, G. M. Whitesides, R. G. Nuzzo, "Formation of monolayer films by the spontaneous assembly of organic thiols from solution onto gold", J. Am. Chem. Soc. **111**, 321 (1989).

[25]J. Stettner, "Self assembled monolayer formation of alkanethiols on gold: growth from solution versus physical vapor deposition", PhD thesis, (2010).

[26]J. H. Choy, S. Y. Kwak, J. S. Park, Y. J. Jeon and J Portier "Intercalative nanohybrids of nucleoside monophosphates and DNA in layered metal hydroxide", J. Am. Chem. Soc. **121**, 1399 (1999).

[27]J. Stettner, P. Frank, T. Griesser, G. Trimmel, R. Schennach, E. Gilli, and A. Winkler, "A study on the formation and thermal stability of 11-MUA SAMs on Au(111)/mica and on polycrystalline gold foils", Langmuir **25**, 1427 (2009).

[28]M.D. Porter, T.B. Bright, D.L. Allara, and C.E.D. Childsey, "Spontaneously organized

molecular assemblies. 4. structural characterization of n-Alkyl thiol monolayers on gold by optical ellipsometry, infrared spectroscopy, and electrochemistry", J. Am. Chem. Soc. **109**, 3559 (1987).

[29]P. A. Noble, "Minireview: a hypothetical model for monitoring microbial growth by using capacitance measurements", J. Microbiol. Methods **37**, 45 (1999).

[30]J. P. Ibbetson, P. T. Fini, K. D. Ness, S. P. DenBaars, J. S. Speck, and U. K. Mishra, "Polarization effects, surface states, and the source of electrons in AlGaN/GaN heterostructure field effect transistors", Appl. Phys. Lett. **77**, 250 (2000).

# Chapter 5

## PZT/AlGaN/GaN heterojunction field effect transistors for reduced gate leakage current

### 5.1 Introduction

Ferroelectrics are dielectric materials that possess spontaneous polarization and also depict the non-linear polarization-electric field dependence, also known as hysteresis loop within certain temperature range.[1] Among the ferroelectric materials, lead zirconium titanate (PZT) is very interesting material because of its pronounced pyroelectric, ferroelectric and electro-optic properties.[2,3] Owing to large remnant polarization in crystalline state, it is also very attractive for the use in non volatile memory, sensors and actuators applications. Compared to small spontaneous polarization of the GaN (~2.9 $\mu C\ cm^{-2}$) and $Al_{0.3}Ga_{0.7}N$ (~4.5 $\mu C\ cm^{-2}$), $Pb(Zr_xTi_{1-x})O_3$ (PZT) exhibits much larger ($2P_r$ of ~100 $\mu C\ cm^{-2}$) remnant polarization.[4,5] This large remnant polarization can be exploited to modulate the 2-dimensional electron gas (2DEG) channel of the AlGaN/GaN HFET. Moreover, ferroelectric thin film as a gate dielectric in field effect transistor also eliminates the need of separate capacitor in the integrated circuit. Application of mechanical stress can induce the electric polarization creating an electric field and vice versa. This interesting feature is useful in many applications such as piezoelectric and pyroelectric sensors, non-volatile random access memory (NVRAM)[6], and surface acoustic wave (SAW) devices.

One of the issue that remain critical in Schottky gate conventional AlGaN/GaN HFET is the large gate leakage current which in turn leads to the device reliability problem, additional noise source and current collapse problem.[7,8,9] Different approaches, including thin gate dielectric layer deposition, were proposed and effectively implemented to alleviate this problem.[10,11,12,13,14]

High permittivity of PZT thin films have attracted increased attention as a gate dielectric on AlGaN/GaN heterojunction field-effect transistors. Generally, a material such as PZT, which is less conducting and more polar, exhibits large dielectric constant ($\kappa$), a property very useful as a gate dielectric. By incorporating physically thicker high $\kappa$ amorphous PZT film as a gate dielectric, gate leakage current can be reduced significantly without much affecting the transistor threshold voltage.

PZT thin film can be deposited using standard thin film deposition techniques, such as RF sputtering, MOCVD and also by sol-gel method. Key advantages of sol-gel deposition techniques can be attributed in its lower deposition cost, excellent control over the thickness & composition over the large substrate, shorter fabrication cycle and lower processing temperature. Lower processing temperature ensures the compatibility with the existing microfabrication technology and retains the amorphous state of the material without the grain boundary. In addition, crystalized PZT at elevated temperature remains very attractive for memory storage devices. The polarization state of the crystalized PZT layer can be switched with the application of the suitable gate bias in metal ferroelectric field effect transistor, for the use as memory storage devices.

The chemical reaction between highly polar ferroelectric material like PZT and conventional semiconducting materials such as Si and GaAs limits their direct

integration. The interfacial reaction degrades the abrupt ferroelectric-semiconductor interface, and thus the device transport properties.[15,16] In this regard; GaN with its higher chemical/thermal stability, built-in spontaneous polarization, etc. presents an attractive semiconducting substrate material to resolve the critical integration issues. Moreover, by incorporating thin interfacial layer such as MgO, PbO, etc. helps to inhibit the interfacial reaction and yields more abrupt interface.[17,18,19]

**5.2 Experiment**

For the study of the electrical properties of the PZT thin film, 0.4M PZT [$Pb(Zr_xTi_{1-x})O_3$, x=52, Inostek] on $Pt/Ti/SiO_2/Si$ wafer was spin coated at 4000 rpm for 20 seconds. Single coating yielded an uniform thickness of about 80 nm. Subsequent pyrolysis and annealing was done at 300℃ for 5 minutes and 650℃ for 30 minutes respectively. Dielectric constant was measured as 500 and 50 for crystalline PZT and amorphous PZT respectively.

AlGaN/GaN HEMT wafer with the same specification as discussed in chapter 4 has been used throughout this experiment. Different sets of devices: mesa etched and unetched, with PZT film and without PZT film were fabricated. Processing parameters such as metal and PZT film thickness, annealing temperature, etc. were kept constant between these devices. Prior to the mesa etching and contact metal deposition, the samples were cleaned in an ultrasonic bath in order to remove any organic and metallic contaminants. The organic solvents used for this purpose are acetone, trichloroethylene (TCE), acetone, methanol and methanol sequentially for 5 minutes each. Then the samples were immersed into the 1:1 by volume ratio solution of hydrochloric acid (HCl)

and deionized water (DI $H_2O$) at 110℃ for 10 minutes to remove the metallic contaminants. After cleaning the sample, mesa etching was performed with Mo/Ni metal stack as a protective mask. In order to form the ohmic contact, Ti (40 nm)/Al (150nm)/Ti (30 nm)/Ni (40 nm)/Au (80 nm) were sputtered using DC magnetron sputtering system. After lift-off, sample was loaded into the rapid thermal annealing chamber and pumped down to a pressure of $2\times10^{-7}\ torr$. The sample was then annealed at 850℃ inside the nitrogen rich chamber for 30 seconds. Prior to depositing the Schottky contact, a thin film (80 nm) of PZT was spin coated onto the device. In order to incorporate amorphous PZT thin layer onto the device, Molybdenum (Mo) was used as a sacrificial mask layer instead of photoresist. Mo being the high temperature metal can withstand the higher temperature during the pyrolysis procedure. Ni (50nm)/Au (80 nm) Schottky contact was then deposited on top of the PZT layer as depicted in Fig. 5.1 (a). Then, hydrogen peroxide ($H_2O_2$) in gentle ultrasonic bath was used to lift off. The attempt of Schottky gate deposition by lifting up molybdenum mask first and then using standard photoresist based lithography produced relatively higher gate leakage current. The degraded PZT film induced by the semiconductor processing steps might have caused the increase in the leakage current.

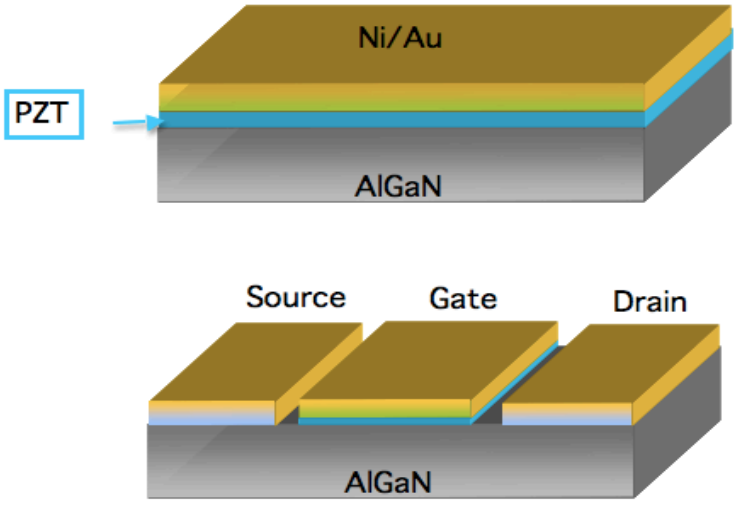


**a)**

**b)**

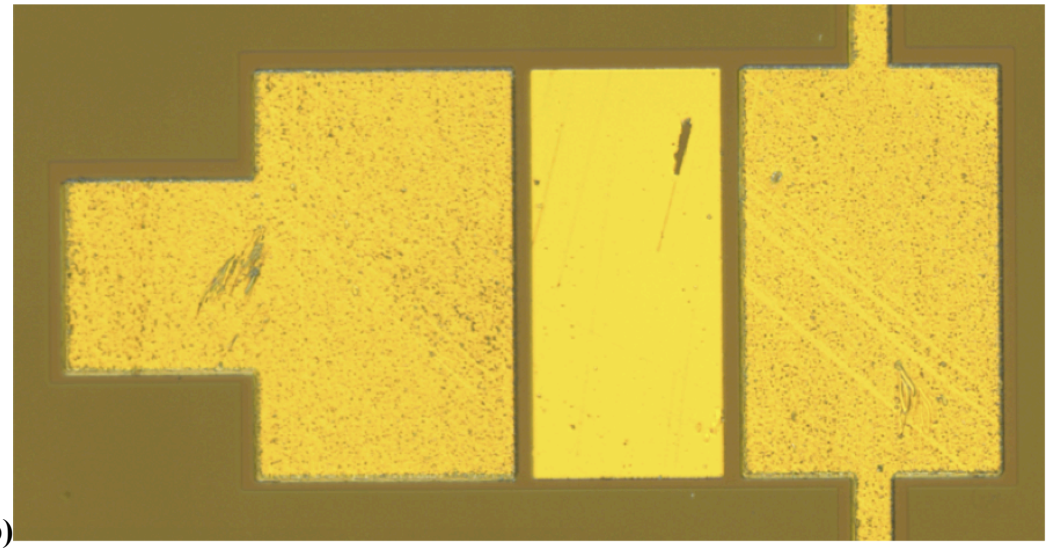

Fig. 5.1 PZT/AlGaN/GaN heterojunction field effect transistor. a) Schematic structure b) Optical micrograph of the fabricated device.

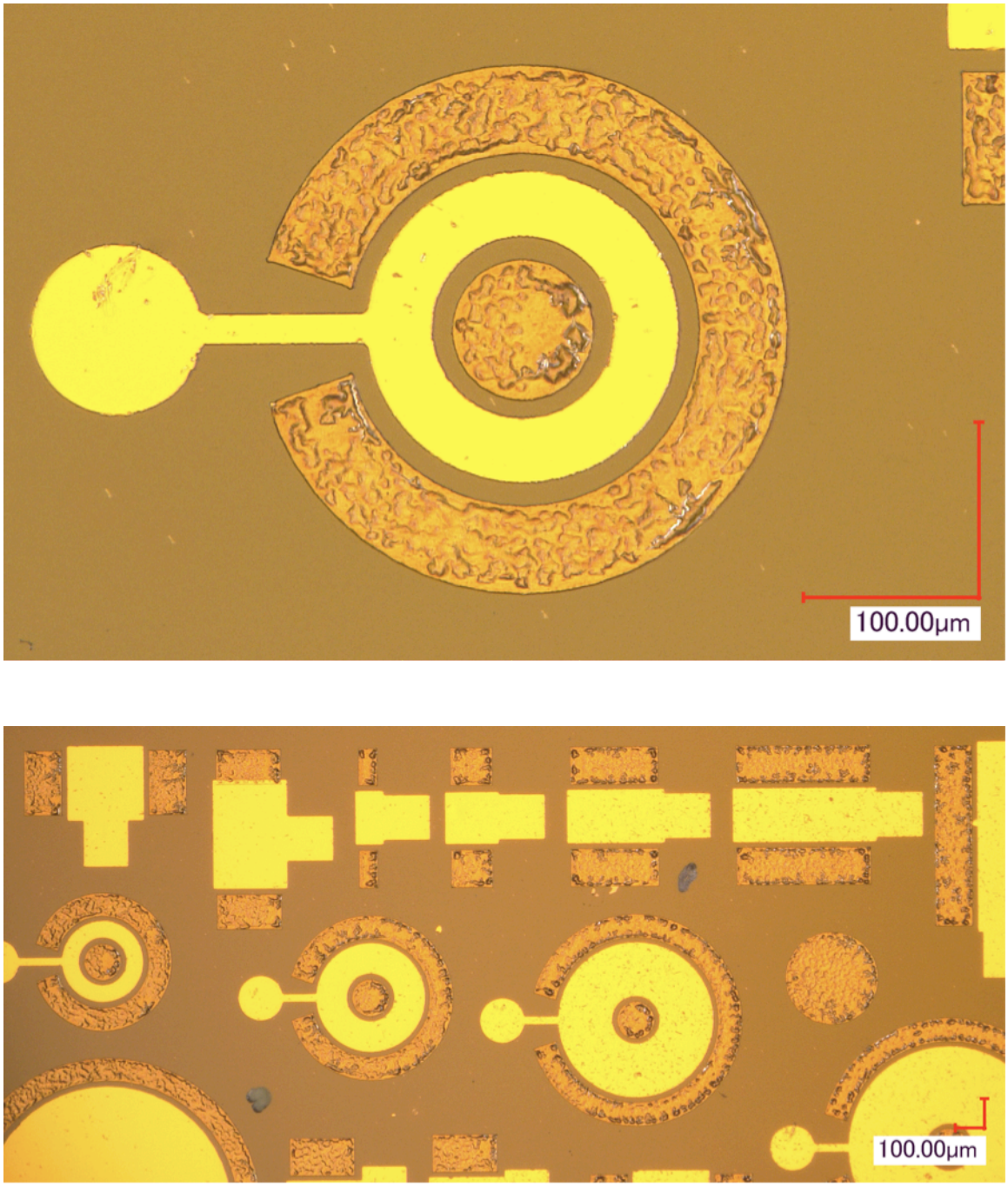


Fig. 5.2 Optical micrograph of the circular and rectangular gate PZT/AlGaN/GaN heterojunction field effect transistors.

## 5.3 Results and discussion

### 5.3.1 Output and gate leakage current characteristics

Fig. 5.3 shows the $I_D$-$V_{DS}$ characteristic of the conventional Ni/Au Schottky gate AlGaN/GaN HFET as a function of different gate bias. The output characteristics of the rectangular gate device with the gate length of 180 $\mu m$ and width of 296 $\mu m$ [without mesa etched – Fig. 5.3 (a), mesa etched – Fig. 5.3(b)], and circular gate device (without mesa etched) with the gate length of 35 $\mu m$ is shown in Fig. 5.3(c).

The distinctive difference between the rectangular gate HFET, and the circular gate HFET is in the proper control transistor output current. Output curve of the mesa unetched device (Fig. 5.3 (a)) shows very difficult to obtain the source-drain current saturation and turn-off. In addition, as the dimension of the rectangular mesa structure was about 8 $\mu m$ greater than the gate structure on each side, mesa etched rectangular gate HFET was still difficult to turn off completely (Fig. 5.3 (b)). On the other hand, circular gate HFET (Fig. 5.3 (c)) shows a complete turnoff, since the direction of the drain-source current was defined properly.

An output current characteristic of PZT/AlGaN/GaN HFET is also shown in Fig. 5.4. It shows a well-behaved saturation current and turn-off of the transistor. Compared to the conventional Schottky gate HFET, threshold voltage has increased from -4V to -6V. This loss in voltage might be attributed to the unoptimized and unannealed PZT/AlGaN interface.

From the Fig. 5.5, it is seen that gate leakage current in the amorphous PZT incorporated AlGaN/GaN HFET has reduced significantly. The difference in the gate

leakage current between the Schottky gate HFET [Fig. 5.5(a)] and PZT gate dielectric incorporated HFET [Fig. 5.5(b)] was more than 4 orders in magnitude.

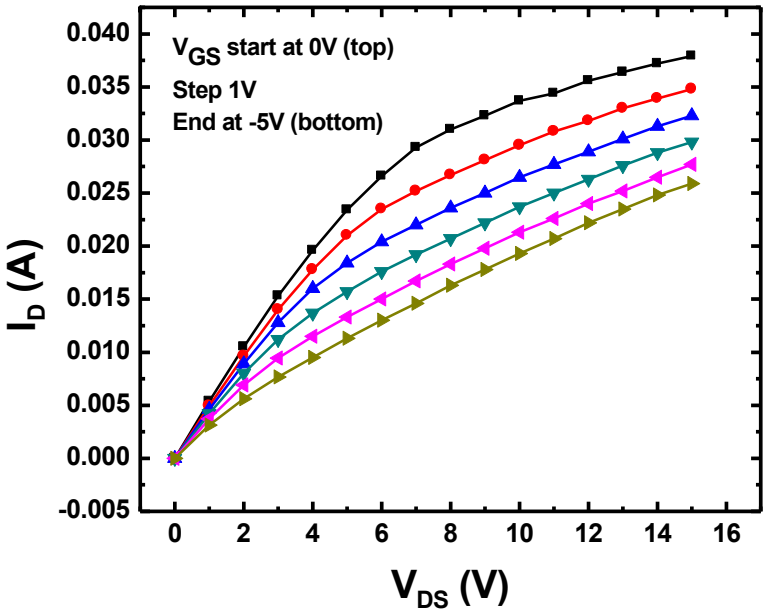


**a)**

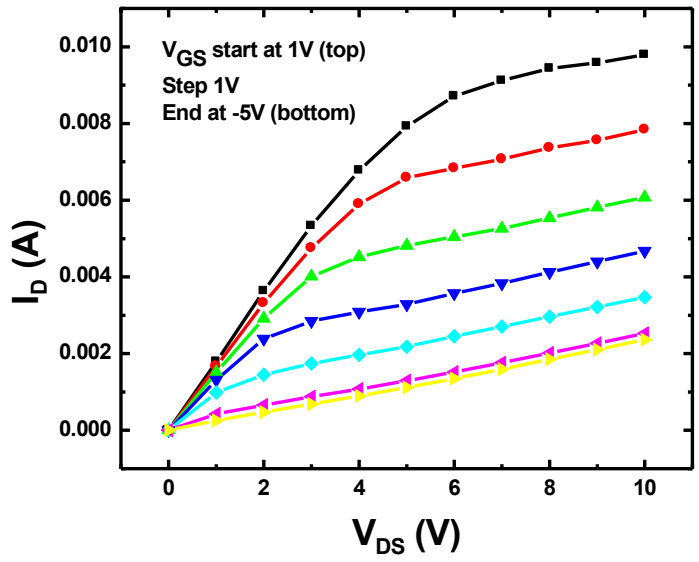


b)

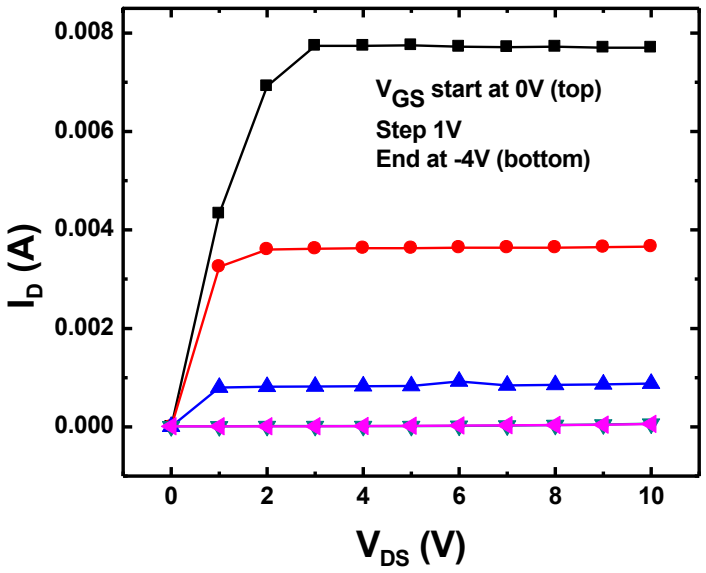


c)

Fig. 5.3 Transistor $I_D$-$V_{DS}$ characteristics of conventional Ni/Au Schottky gate AlGaN/GaN HFET. (a) $I_D$-$V_{DS}$ curve for the rectangular gate AlGaN/GaN HFET (without mesa etched) (b) $I_D$-$V_{DS}$ curve for the rectangular gate AlGaN/GaN HFET (mesa etched- dimension of the rectangular mesa structure was about 8 $\mu m$ greater than the gate structure on each side) c) $I_D$-$V_{DS}$ curve for the circular gate AlGaN/GaN HFET.

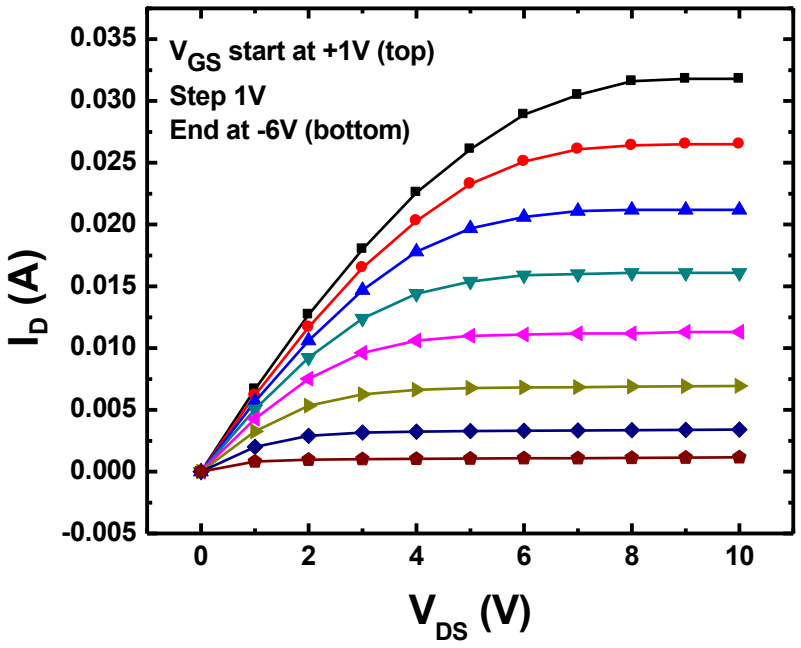


**b)**

Fig. 5.4 $I_D$-$V_{DS}$ characteristics of PZT/AlGaN/GaN HFET.

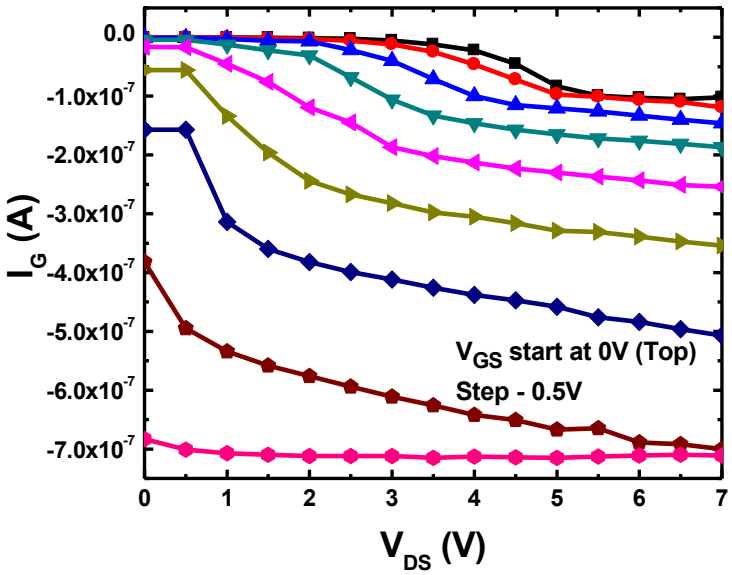


**a)**

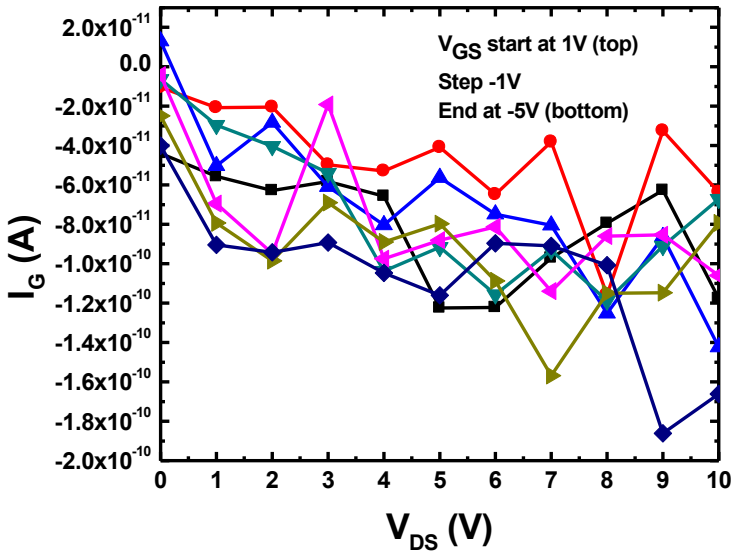


**b)**

Fig. 5.5 Gate current leakage characteristics of rectangular gate HFET. a) AlGaN/GaN HFET. b) PZT/AlGaN/GaN HFET.

The incorporated amorphous PZT thin film gate dielectric was fairly stable within the transistor operating range and showed a good current control characteristic. As shown in the Fig. 5.6 (a), PZT dielectrics sustained the gate voltage swing of +3V to -15V without the degradation. Beyond these values, significant increase in gate leakage current was observed and was similar to that of conventional Schottky gate AlGaN/GaN HFET as depicted in Fig. [5.6 (b)].

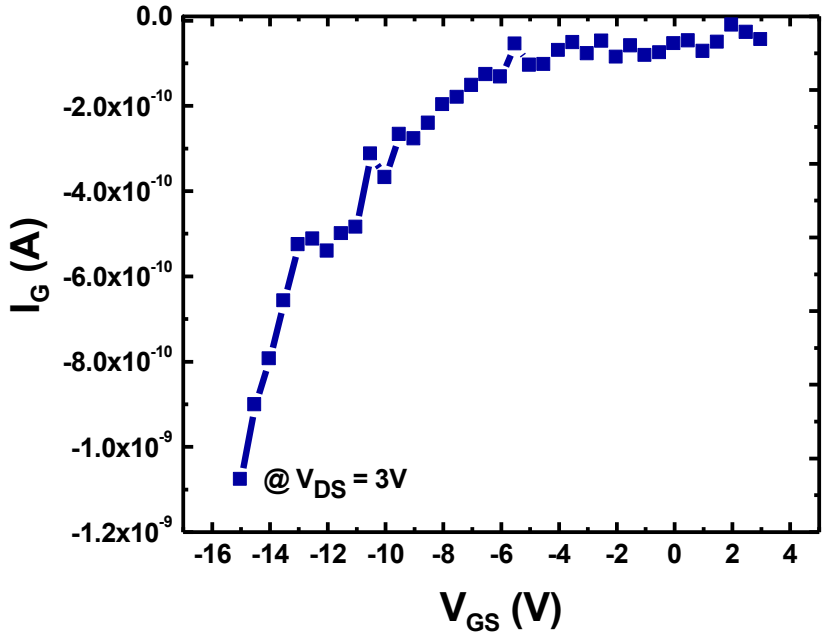


a)

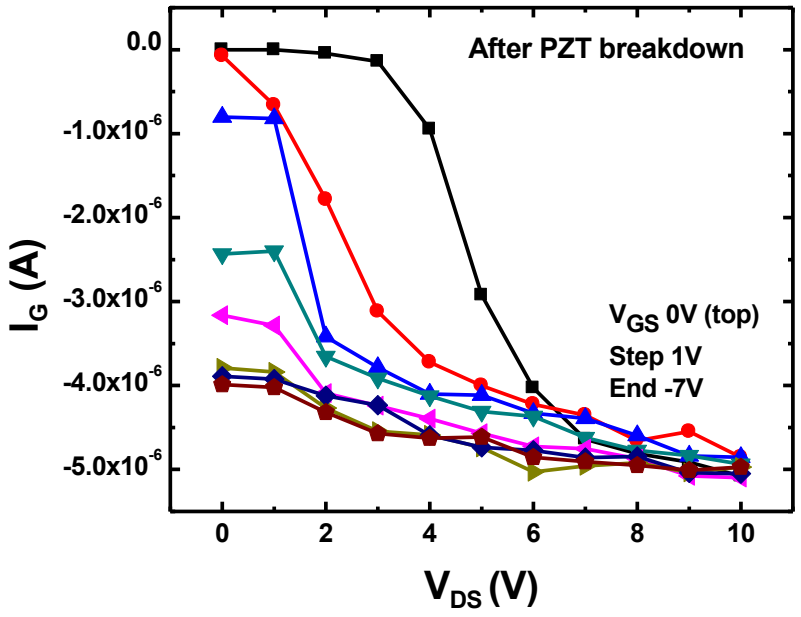


b)

Fig. 5.6 a) $I_G$-$V_{GS}$ curve of the PZT/AlGaN/GaN heterostructure field effect transistor. b) $I_G$-$V_{DS}$ curve for the same device after PZT degradation.

| Samples | Thickness | Roughness rms (nm) | $E_g$ (eV) |
|---|---|---|---|
| $PbZr_{0.8}Ti_{0.2}O_3$ (amorphous) | 109 | 0.68 | 4.34 |
| $PbZr_{0.8}Ti_{0.2}O_3$ (polycrystalline) | 96 | 1.18 | 3.73 |
| $PbZr_{0.7}Ti_{0.3}O_3$ (amorphous) | 110 | 0.61 | 4.24 |
| $PbZr_{0.7}Ti_{0.3}O_3$ (polycrystalline) | 102 | 1.06 | 3.67 |
| $PbZr_{0.5}Ti_{0.5}O_3$ (amorphous) | 89 | 0.57 | 4.20 |
| $PbZr_{0.5}Ti_{0.5}O_3$ (polycrystalline) | 81 | 1.03 | 3.57 |
| $PbZr_{0.4}Ti_{0.6}O_3$ (amorphous) | 102 | 0.53 | 4.12 |
| $PbZr_{0.4}Ti_{0.6}O_3$ (polycrystalline) | 94 | 0.96 | 3.50 |

Table 5.1 Physical property of PZT thin layer.[20]

As given in table 5.1, polycrystalline PZT films will have a higher rms-roughness (~ 1 nm) and larger spherical grain size (~ 20 nm), whereas amorphous PZT films exhibit rms-roughness of (~ 0.6 nm) and microcrystal particles with a size of (~ 1-2 nm). For an amorphous PZT film, the energy band gap was found to decrease from 4.34 eV to 4.12 eV with the increasing Ti content from 0.2 to 0.6, whereas crystalline PZT film showed the energy bandgap of 3.73 eV to 3.50 eV over the Ti content from 0.2 to 0.6.[20] As the band gap of the amorphous PZT layer is comparable or slightly higher than that of the AlGaN layer, conduction band offset will be slightly positive. Observed reduction in the gate leakage current can be attributed to the combined effect of positive band offset and increased barrier width due to the PZT layer. Moreover, dominant leakage current path

for the high $\kappa$ dielectrics lies at the grain boundaries and the amorphous PZT without the grain boundary also has helped in the overall reduction in the gate leakage current.

### 5.3.2 Transfer characteristics

$I_D$-$V_{GS}$ characteristics of the amorphous PZT/AlGaN/GaN HFET have been studied, and the results were shown in the Fig. 5.7. In all measurements, gate voltage was swept from -8V to +2V and back +2V to -8V. For the conventional Schottky gate AlGaN/GaN HFET, $I_D$-$V_{GS}$ curve showed no hysteresis as shown in the Fig. 5.8 (a). However, the clockwise hysteresis observed in the PZT/AlGaN/GaN HFET in Fig. 5.8 (b) might be attributed to the carrier trapping and de-trapping phenomena occurred at an unpotimized PZT/AlGaN interface. Negative transconductance in AlGaN/GaN HFET for positive gate bias might be the effect of carrier injection from the 2DEG channel into the AlGaN barrier layer.

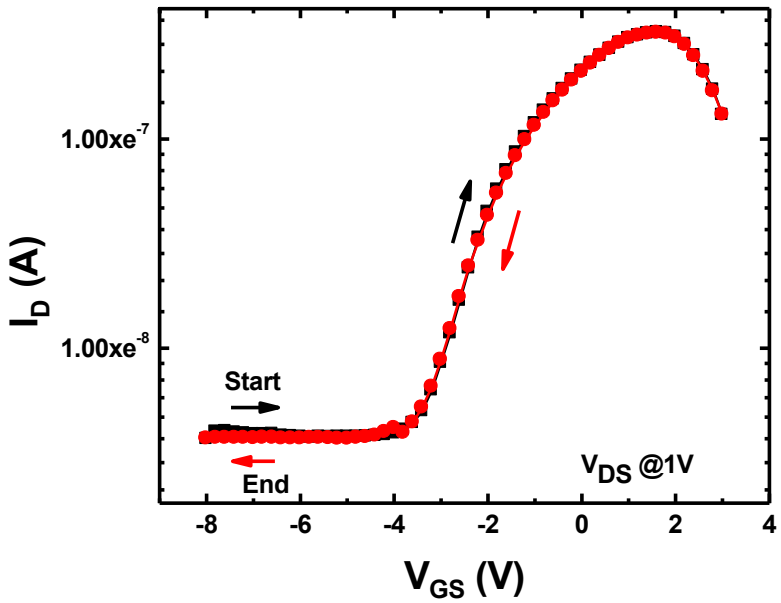


**a)**

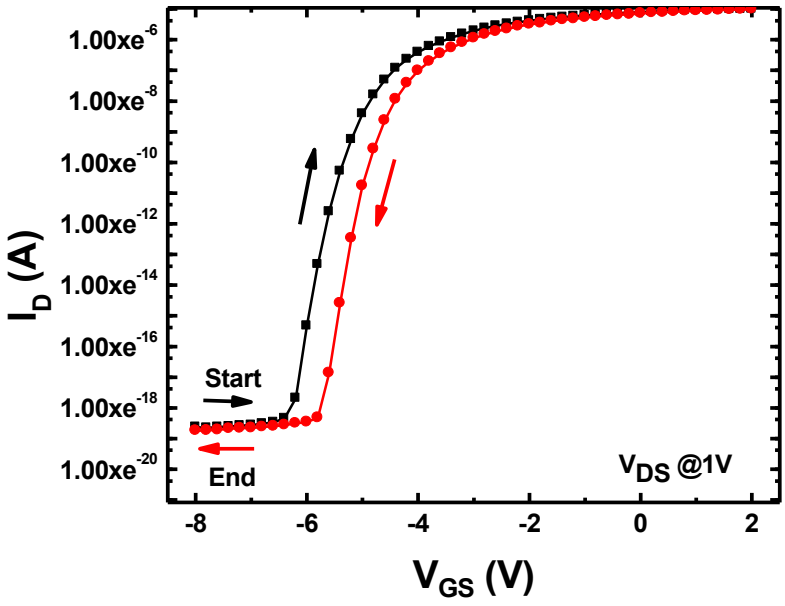


**b)**

Fig. 5.7 Transfer characteristics of a) AlGaN/GaN HFET b) PZT/AlGaN/GaN HFET.

### 5.4 Summary and conclusions

AlGaN/GaN heterojunction field effect transistors with different device structure were fabricated and current voltage characteristics were studied. Proper device isolation was found to be very crucial in order to control the transistor. Moreover, amorphous PZT thin film was incorporated as a gate dielectric into the AlGaN/GaN heterojunction field effect transistor. Significant reduction in the gate leakage current was observed as compared to the Schottky gate AlGaN/GaN HFET.

## 5.5 Future work

Crystalline PZT films are known for ferroelectricity, piezoelectricity and pyroelectricity. By crystalizing PZT film, these effects can be studied in AlGaN/GaN ferroelectric field effect transistors for sensors and actuators applications. In addition, relative study of amorphous, single crystalline and polycrystalline PZT films as a gate dielectric in AlGaN/GaN HFET can provide their effectiveness as a dielectric, ferroelectric, piezoelectric and pyroelectric material.

**References**

[1] N. Izyumskaya, Ya. Alivov & H. Morkoç, "Oxides, oxides, and more oxides: high-κ oxides, ferroelectrics, ferromagnetics, and multiferroics", Crit. Rev. Solid State. **34**, 89 (2009).

[2] J. F. Scott and C. A. Paz de Araujo, "Ferroelectric memories", Science **246**, 1400 (1989).

[3] Y. Xu, "Ferroelectric materials and their applications", North-Holland, Amsterdam, Chap. 4, p. 206 (1991).

[4] O. Ambacher, J. Smart, J. R. Shealy, N. G. Weimann, K. Chu, M. Murphy, W. J. Schaff and L. F. Eastman, "Two-dimensional electron gases induced by spontaneous and piezoelectric polarization charges in N- and Ga-face AlGaN/GaN heterostructures", J. Appl. Phys. **85**, 3222 (1999).

[5] C.J. Zhang, Y.F. Chen, Z.G. Wang, B.L. Tian, C. Chen, X.W. Deng, M. Liu, Y. Zhang, X.Z. Liu, Y.R. Li, "Growth and structure of MBE-grown $PbTiO_3$ epilayers by using RF atomic oxygen source", J. Cryst. Growth **312**, 382 (2010)

[6] P. J. Hansen, L. Shen, Y. Wu, A. Stonas, Y. Terao, S. Heikman, D. Buttari,T. R. Taylor, S. P. DenBaars, U. K. Mishra, R. A. York, and J. S. Speck, "AlGaN/GaN metal-oxide-semiconductor heterostructure field- effect transistors using barium strontium titanate," J. Vac. Sci. Technol. B **22**, 2479 (2004).

[7] A. V. Vertiatchikh and L. F. Eastman, "Effect of the surface and barrier defects on the AlGaN/GaN HEMT low-frequency noise performance," IEEE Electron Device Lett. **24**,

535 (2003).

[8] H. Hasegawa, T. Inagaki, S. Ootomo, and T. Hashizume, "Mechanisms of current collapse and gate leakage currents in AlGaN/GaN heterostructure field effect transistors," J. Vac. Sci. Technol. B, Microelectron. Process. Phenom. **21**, 1844 (2003).

[9] G. Meneghesso, G. Verzellesi, F. Danesin, F. Rampazzo, F. Zanon, A. Tazzoli, M. Meneghini, and E. Zanoni, "Reliability of GaN high- electron-mobility transistors: State of the art and perspectives," IEEE Trans. Device Mater. Rel. **8**, 332 (2008).

[10] J. W. Chung, J. C. Roberts, E. L. Piner, and T. Palacios, "Effect of gate leakage in the subthreshold characteristics of AlGaN/GaN HEMTs," IEEE Electron Device Lett. **29**, 1196 (2008).

[11] R. Chu, L. Shen, N. Fichtenbaum, D. Brown, S. Keller, and U. K. Mishra, "Plasma treatment for leakage reduction in AlGaN/GaN and GaN Schottky contacts," IEEE Electron Device Lett. **29**, 297 (2008).

[12] P. D. Ye, B. Yang, K. K. Ng, J. Bude, G. D. Wilk, S. Halder, and J. C. M. Hwang, "GaN metal–oxide–semiconductor high-electron- transistor with atomic layer deposited $Al_2O_3$ as gate dielectric," Appl. Phys. Lett. **86**, 501 (2005).

[13] C. Liu, E. F. Chor, and L. S. Tan, "Investigations of $HfO_2$/AlGaN/GaN metal–oxide–semiconductor high electron mobility transistors," Appl. Phys. Lett. **88**, 173 (2006).

[14] V. Adivarahan, M. Gaevski, W. H. Sun, H. Fatima, A. Koudymov, S. Saygi, J. Yang, M. A. Khan, A. Tarakji, M. S. Shur, and R. Gaska, "Sub- micron gate $Si_3N_4$/AlGaN/GaN

metal–insulator–semiconductor heterostructure field-effect transistors," IEEE Electron Device Lett. **24**, 54 (2003).

[15] I. Stolichnov, L. Malin, P. Muralt, N. Setter, "Ferroelectric gate for control of transport properties of two-dimensional electron gas at AlGaN/GaN heterostructures." Appl. Phys. Lett. **88**, 043512 (2006).

[16] T. P. Ma and J. P. Han, "Why is nonvolatile ferroelectric memory field-effect transistor still elusive?" IEEE Electron Device Lett. **23**, 386 (2002).

[17] B. Xiao, X. Gu, N. Izyumskaya, V. Avrutin, J. Xie, H. Liu, H. Morkoc, "Structural and electrical properties of $Pb(Zr,Ti)O_3$ grown on (0001) GaN using a double $PbTiO_3$/PbO bridge layer." Appl. Phys. Lett. **91**, 182908 (2007).

[18] W. Cao, S. Bhaskar, J. Li, S. Dey, "Interfacial nanochemistry and electrical properties of $Pb(Zr_{0.3}Ti_{0.7})O_3$ films on GaN/sapphire." Thin Solid Film **484**, 154 (2005).

[19] S. Dey, S. Bhaskar, M Tsai, W. Cao, "$Pb(Zr,Ti)O_3$-GaN heterostructures for RF MEMS applications." Int. Ferro. **62**, 69 (2004).

[20] S. Yang, Y. Zhang, and D. Mo, "A comparison of the optical properties of amorphous and polycrystalline PZT thin films deposited by the sol–gel method" Mater. Sci. Eng. B **127**, 117 (2006).